Analysis of vegetation-atmosphere transfers simulated by the Interaction Soil-Biosphere-Atmosphere (ISBA) model for a beech forest in Lorraine, France

Auteur : Acerbis, Julie
Promoteur(s) : Longdoz, Bernard
Faculté : Gembloux Agro-Bio Tech (GxABT)
Diplôme : Master en bioingénieur : sciences et technologies de l'environnement, à finalité spécialisée
Année académique : 2023-2024
URI/URL : http://hdl.handle.net/2268.2/19713

LIÈGE université
Gembloux
Agro-Bio Tech

Analysis of vegetation-atmosphere transfers simulated by the Interaction Soil-Biosphere-Atmosphere (ISBA) model for a beech forest in Lorraine, France

Julie Acerbis

THESIS SUBMITTED FOR THE DEGREE OF MASTER IN BIOENGINEER
SPECIALISED IN ENVIRONMENTAL SCIENCES AND TECHNOLOGIES

ACADEMIC YEAR 2023-2024

SUPERVISOR: BERNARD LONGDOZ

[1] L'autorité académique est représentée par le promoteur, membre du personnel enseignant de GxABT (Bernard Longdoz)

[2] The academic authority is represented by the thesis supervisor, a member of the GxABT teaching staff (Bernard Longdoz)

LIÈGE université
Gembloux
Agro-Bio Tech

Analysis of vegetation-atmosphere transfers simulated by the Interaction Soil-Biosphere-Atmosphere (ISBA) model for a beech forest in Lorraine, France

Julie Acerbis

THESIS SUBMITTED FOR THE DEGREE OF MASTER IN BIOENGINEER
SPECIALISED IN ENVIRONMENTAL SCIENCES AND TECHNOLOGIES

ACADEMIC YEAR 2023-2024

SUPERVISOR: BERNARD LONGDOZ

This master thesis was carried out with the support of the Biosystems Dynamics and Exchanges (BIODYNE) department of Gembloux Agro-Bio Tech, University of Liege, as well as the help of INRAE and Météo France, respectively represented by Bernard Longdoz, Emilie Joetzjer and Christine Delire.

Abstract

Climate change is anticipated to increase the frequency of drought events, posing a significant threat to the European Beech, *Fagus Sylvatica L.*, known for its high sensitivity to such conditions. This heightened vulnerability may lead to a northward migration of its distribution, impacting carbon sequestration. In light of these concerns, developing land surface models tailored to forest ecosystems becomes crucial for predicting their fate under changing climate conditions. To address this, the Interaction Soil-Biosphere-Atmosphere (ISBA) component of the SURFEX model underwent adjustments to refine predictions under drought events, specifically considering the unique phenology of the Beech. The study focuses on the ICOS network station located in the Beech forest of Hesse, France, providing standardized, high-precision, high-frequency, and long-term observations. Initially, a simulation was conducted, keeping the ISBA model intact to evaluate its baseline performance. Subsequently, two simulations were implemented to impose phenological adjustments, enhancing the representation of carbon transfers between the soil-plant system and the atmosphere. The first simulation incorporated the observed Leaf Area Index (LAI) into the photosynthesis subroutine, while the second, more performant, additionally implemented observed LAI in the carbon allocation scheme. Despite these advancements, the drought-induced reduction in latent heat flux and gross primary production were poorly represented. Further adjustments, such as implementing hydraulic architecture, are necessary to refine the drought response regarding the water vapour fluxes.
The promising results of imposing phenology hold the potential to yield an enhanced representation of soil-plant system exchanges with the atmosphere. This improvement, once achieved, would enable more accurate forecasting of forest responses under climate change conditions.

Keywords: *Fagus Sylvatica L.* - Land surface model - ISBA - ICOS network - Phenology - Soil-plant system exchanges with the atmosphere - Climate change

Résumé

L'augmentation de la fréquence des événements de sécheresse suite aux conséquences du changement climatique menace le Hêtre européen, *Fagus Sylvatica L.*, qui a une grande sensibilité à ces conditions. Cette vulnérabilité accrue pourrait entraîner une migration vers le nord de sa distribution, ce qui impacterait la séquestration du carbone. Face à ces préoccupations, le développement de modèles de surface adaptés aux écosystèmes forestiers devient crucial pour prédire leur destin sous changement climatique. Dans ce but, le modèle Interaction Sol-Biosphère-Atmosphère (ISBA), composant du modèle SURFEX, a fait l'objet d'ajustements afin d'améliorer les prédictions lors d'événements de sécheresse, en tenant compte de la phénologie particulière du Hêtre. L'étude se concentre sur la station du réseau ICOS située dans la hêtraie de Hesse, en France, fournissant des observations normalisées, de haute précision, à haute fréquence et à long terme. Premièrement, une simulation a été réalisée en maintenant le modèle ISBA intact pour évaluer ses performances de base. Ensuite, deux simulations ont été mises en œuvre pour imposer des ajustements phénologiques, améliorant la représentation des transferts de carbone entre le système sol-plante et l'atmosphère. La première simulation a intégré l'indice de surface foliaire (LAI) observé dans la sous-routine de photosynthèse, tandis que la deuxième, plus performante, a également inclut l'indice LAI observé dans le schéma d'allocation du carbone. Malgré l'amélioration des prédictions, la réduction induite par la sécheresse du flux de chaleur latente et de la production primaire brute n'était pas représentée. Dès lors, des ajustements supplémentaires, tels que la mise en œuvre d'une architecture hydraulique, sont nécessaires pour affiner la réponse à la sécheresse, en particulier en ce qui concerne les flux de vapeur d'eau.
Les résultats prometteurs de l'imposition de la phénologie ont le potentiel de mener à une représentation améliorée des échanges entre le système sol-plante et l'atmosphère. Une fois cette amélioration réalisée, elle permettrait une prévision plus précise des réponses des forêts sous les conditions du changement climatique.

Mots-clés : *Fagus Sylvatica L.* - Modèle de surface terrestre - ISBA - Réseau ICOS - Phénologie - Échanges sol-plante avec l'atmosphère - Changement climatique

Contents

1 Introduction

1.1 General context

Global warming is now a burning issue, with climate change key indicators currently breaking records. For example, the multiplication of drought events (Gaudin, 2015) and heat waves, the rising sea levels and ice loss in polar regions and mountain glaciers ((NASA, 2023)). These events already have noticeable devastating effects on ecosystems and jeopardise food and water security (Intergovernmental Panel on Climate Change (2023)), emphasising the urgency of addressing climate change. Meanwhile, global warming will cause a shift in crops and forest settlements.

In response, international agreements such as the Kyoto Protocol and the Paris Agreement were adopted during the Conference of the Parties (COP) in the framework of the United Nations Framework Convention on Climate Change (UNFCCC) to reduce greenhouse gas (GHG) emissions and mitigate climate change. However, despite these efforts, GHG emissions from human activities continue to increase (Intergovernmental Panel on Climate Change (2023)). Burning fossil fuels, deforestation, and industrial processes increase heat-trapping GHG levels in Earth's atmosphere. Regarding total warming potential, the predominant GHGs are carbon dioxide and methane, respectively, representing 86,2% and 7,1% of total GHG emissions for Belgium in 2021 (SPF Santé publique, sécurité de la chaîne alimentaire et environnement (2023)).

Terrestrial and marine habitats play a mitigating role against climate change by sequestrating atmospheric carbon partway, helping reduce its concentration. Forests, in particular, represent the second largest terrestrial reservoir of carbon per unit area (European Environment Agency (2022)). Yet, climate change and interactions with its consequences could shift the future carbon balance of forests from sink to source (Thom (2023); Brienen et al. (2020)). Understanding and modelling these complex interactions will enhance the activities and policies to preserve forests and their ecosystem services. Moreover, species sensitivity to climate change must be considered in projections relating to carbon sinks, forest management and resilience-boosting policies.

1.2 Beech forests and drought

Climate change in France and Belgium will increase summer temperatures and, although the signal is unclear, possibly decrease summer precipitation. Thus, drought event frequency will increase, partly due to increased summer evapotranspiration caused by increased temperatures. European Beech, *Fagus sylvatica* L., with their hygrophilous physiology, are among the most sensitive species to drought (Bréda et al. (2004)). Indeed, the temperature and the photoperiod are the main drivers of budding and senescence (Jean et al. (2023)). Also, water availability, which could become a limiting factor, temperature and rainfall deficit are sufficient to determine the distribution of Beech (Pinto and Gégout (2005); Weng et al. (2017); Landmann et al. (2007); Inventaire Forestier National (2005)). The temperature drives the distribution of deciduous forests by affecting the nitrogen mineralisation rates and thus its availability for tree uptake (Landmann et al. (2007)). Despite their drought sensitivity, European Beech exhibited fast and important R_{eco}very ability and among the lowest mortality rates in forest monitoring networks following the 2003 drought (Landmann et al. (2008)). However, the abovementioned observations must be considered cautiously as they are localised and do not reflect a general feature (Frei et al. (2022); Obladen et al. (2021); Thom (2023)). For instance, beech decline was observed in several regions in Europe following prolonged and repeated periods of drought since 2018 (Langer and Bußkamp (2023)). The beech fate under climate change will also depend on the management type and development stage (Frei et al. (2022); Chen et al. (2023); Obladen et al. (2021); Rukh et al. (2020); Gossner et al. (2019); Brück-Dyckhoff et al. (2019)). The drought impact is far from negligible, and cumulative effects with other consequences of climate change could lead to perturbations in Beech's phenology, growth, and reproduction. Moreover, European Beech might migrate northward and at higher altitudes, and their

potential extinction in southern regions would have a significant impact on the landscape and carbon sequestration (Bolte et al. (2010); Dolar et al. (2023); Gregorčič et al. (2023); Stojanović et al. (2013)).

Drought stress depends on meteorological conditions, precipitation, potential soil water stocks, and root depths (WSL (Institut fédéral de recherches sur la forêt, la neige et le paysage) (2020)). It could directly reduce photosynthesis with a deficit in soil water content or indirectly through beetle attacks, sunburn, fungal infections and complex diseases (Langer and Bußkamp (2023); Lebourgeois et al. (2001)). During edaphic drought (i.e. deficit in soil water content), the tree will try to avoid water loss through transpiration by closing the stomata, which reduces photosynthesis and inhibits growth. Despite this regulation strategy, persistent drought can result in irreversible damage. When the soil can no longer provide water sufficiently, the sap tension in the vessels rises, and cavitation occurs in the phloem conducting system in leaf petioles, small branches and twigs. Even if the water stock improves after cavitation, the conducting system remains impaired, resulting in embolism-induced wilting, especially in the canopy. After the prolonged and intense edaphic droughts in 1982 and 2003, green leaves and leafy twigs fell from the Beech (Bréda et al. (2004); Schutt et al. (1984)). Increased drought vulnerability is often implied to height-associated hydraulic constraints (Socha et al. (2023); Frei et al. (2022)). Yet, conclusive evidence is still lacking (Fernández-de Uña et al. (2023)). The close coupling between the sap flow and the water vapour flux escaping through stomata highlights the vital role of stomatal closure. It protects the sap flow conducting system by limiting water tensions between the soil and leaves, thus preventing catastrophic embolism. Hence, the fertilising effect and growth rate acceleration due to higher atmospheric carbon dioxide concentration, nitrogen deposition, and longer growing seasons could lead to an overshoot in aboveground biomass, resulting in water stress under drought conditions. It is attributable to a temporal mismatch between water demand and availability, consequently increasing the mortality rate (Socha et al. (2023); Chen et al. (2023)). The previous summer water stress also influenced crown state and shoot growth. Besides, the width of the annual ring is determined by the earliness of water deficit during the growing season, which is defined by the interaction between climate, available water reserve depending on soil type and leaf area index (Landmann et al. (2007)).
Secondary effects of drought stress and damage on Beech are a higher infestation of beetles (*Agrilus viridis* L., ambrosia beetles, Scolytinae), microfungi and bleeding cankers (Gossner et al. (2019); Frei et al. (2022); Brück-Dyckhoff et al. (2019)). Major beetle outbreaks initiated in drought conditions can accelerate beech mortality rate (Brück-Dyckhoff et al. (2019)). Indeed, trees with a higher proportion of crown die-back show a higher frequency of infestations (Frei et al. (2022).

Accordingly, the accuracy of predictions of drought-driven mortality based on physiology alone is limited (Trugman et al. (2021)). The fate of beech trees also depends on adaptations or community-level ecological interactions (Socha et al. (2023); Trugman et al. (2021)), current or future genetic variability, adaptation abilities, competition dynamics, and species migration (Landmann et al. (2007)). However, the knowledge on those aspects is limited and ongoing research is being conducted (Prigoliti et al. (2023); Dolar et al. (2023); Gregorčič et al. (2023); Marchelli et al. (2017)). With the current knowledge, predictions concerning the survival of Beech in regions bordering its present distribution area require the consideration of various variables. Based on the observations mentioned above, models ought to encompass the energy, carbon, nitrogen, and water cycles, along with climate and soil information, at diverse resolutions-continental, regional, and local (Simon et al. (2023); Zell et al. (2019); Stojanović et al. (2013)).

1.3 Monitoring of greenhouse gases (GHG) and water fluxes (measurements and modelling)

Understanding greenhouse gas (GHG) and water between ecosystems and the atmosphere is crucial for effective policy- and decision-making in climate change mitigation, in line with the objectives of the UNFCCC's Agreements. Accordingly, the Integrated Carbon Observation System (ICOS) has established a network composed of 170 measurement stations across 16 European countries (ICOS (2023b)). It provides standardised, high-precision and long-term observations in open-source of GHG concentrations in the atmosphere and carbon, water and energy fluxes between atmosphere, land surface and oceans (ICOS

(2023b)). The measurements of carbon and energy fluxes are carried through the Eddy Covariance technique. The ICOS network promotes technological developments and provides necessary information on GHG, which facilitates carbon cycle research. Given the importance of forests in carbon sequestration and heat regulation, as well as their vulnerability to the consequences of global warming, it is crucial to quantify and monitor their exchange with the atmosphere. This knowledge will enhance our understanding of their dynamics and enable the prediction of the impact of global warming consequences in their mitigating role. Consequently, half of the ICOS network's Ecosystem domain is implanted in forest land cover. Within this network, some measurement stations are located in European Beech (*Fagus sylvatica* L.) forest sites, such as Hainich and Hohes Holz in Germany, Soroe in Denmark and Hesse, France.

Various land surface models have been developed to simulate the exchange of energy, water and GHG fluxes between the surface and the atmosphere. These models are used to predict fluxes dynamics under climate change across diverse ecosystems. These models represent the Earth's surface, including vegetation, soils and water bodies and their complexity and simulate a constantly increasing number of processes (Delire et al. (2020)). They use satellite observations, terrestrial measurements, climate datasets, meteorological model outputs, or both as input to simulate the soil-vegetation-atmosphere exchanges. This simulation is achieved by modelling physical, chemical and biological processes through differential equations. Models differ in the incorporated processes and the complexity degree of their representation (Delire et al. (2020)). Because they are intricately interconnected, models must account for all relevant parameters and processes concerning different components. For instance, plant carbon metabolism (photosynthesis, photorespiration and respiration) is impacted by rising atmospheric CO2 concentrations and temperatures, both separately and in combination (Dusenge et al. (2019)). Another example is stomatal conductance, which regulates the net CO2 assimilation, leaf dark respiration, and evapotranspiration and directly impacts the plant water relations according to Farquhar and Sharkey (1982). This conductance partly depends on variables like vapour pressure deficit and air temperature. A rise in air temperature results in a stomatal opening, which can lead to water stress (Urban et al. (2017)).
These models shed light on the processes of carbon fluxes (sequestration and emissions) and heat fluxes for different ecosystems, considering the changes in temperature and precipitation and their interactions. They also contribute to the research of climate change and weather forecasting by helping to understand the complex interactions between the atmosphere, land, and oceans. Factors' dependency can be highlighted at the ecosystem scale. The ICOS dataset enables calibration and evaluation of those models due to its standardised, high-precision, high-frequency and long-term observations.
Among these models, few are developed by French teams such as ORCHIDEE (Chen et al. (2016)) and the Interaction Soil-Biosphere-Atmosphere (ISBA) from the SURFEX model (Delire et al. (2020); Noilhan and Planton (1989); Gibelin et al. (2008)), which simulate the functioning of all the ecosystem types and can be coupled with a meteorological forecasting model or forced with atmospheric data (offline run). They can be used to fill data sets of land carbon sinks across extensive geographical regions without measurement stations, such as to complete the global carbon budget from the Global Carbon Project (Delire et al. (2020)). Other models are specific to an ecosystem and can only be used with atmospheric forcing data, e.g. CASTANEA (Dufrêne et al. (2005)), which is specific to forest ecosystems.

ISBA was used for this thesis for the following reasons. Firstly, the opportunity to have access to the model program and the support of the team managing this model thanks to the collaboration between the Biosystems Dynamics and Exchanges (BIODYNE) department of Gembloux Agro-Bio Tech, University of Liege, the INRAE and Météo France. Secondly, the 2008 ISBA version performs relatively well for simulating deciduous broadleaf forest growth (Gibelin et al. (2008)), demonstrating a good match with observed variability driven by climate conditions. Hence, an evaluation of the latest version's performance is interesting. Also, ISBA has already been used to model drought's effects on the Amazon rainforest (Joetzjer (2014)). Therefore, the model can be used to estimate the reaction of beech forests to forthcoming climate changes.

1.4 Thesis objectives

Forests are essential to mitigate the effects of climate change while simultaneously being susceptible to its consequences. Accordingly, it is crucial to develop surface models adapted to forest ecosystems to predict their functioning as climate change occurs. This master's thesis aims to adjust the surface model ISBA from the French weather forecasting service research centre (CNRM (2023)) to a deciduous broadleaf forest, specifically the Hesse beech forest in France, where a flux tower has been installed since 1997. The site (called FR-Hes) is a part of the ICOS ecosystem network. This site was chosen for its climate, similar to Wallonia's, the previous collaboration with the team in charge of its management, and because of the extensive meteorological and ancillary measurements available.

Before the model's adaptation, a deeper understanding of the carbon allocation scheme and the processes implementation was needed (Section 2.2). Then, a spin-up (Section 4.1) and a prediction with reference parameter values (Section 2.4) were required to determine whether a modification was necessary. Indeed, if the model accurately represents the observations, there is no point in modifying it. The prediction was realised for 2001 and 2002 to allow a comparison with the observation from the FRHes station. This analysis focused on the energy and carbon fluxes. Besides, ISBA's main issue is its representation of the seasonality of the Leaf Area Index, which was also explored in this thesis (Section 4.2) as it could impact the carbon cycle.

The modified model will allow the prediction of the carbon and energy fluxes, providing estimates of the Hesse forest's contribution to carbon dioxide sequestration and heat regulation. Furthermore, it will enable the analysis of environmental constraints such as drought and their impact on the forest ecosystem.

2 Materials and methods

2.1 Study site

2.1.1 Hesse

The ICOS network gathers nine deciduous broadleaf forest stations, including the study site, the beech forest of Hesse (Figure 1b). It was labelled class 1 ICOS in 2022 (ICOS (2023a)) but monitored since 1997. The Hesse forest is located in the northeast of France (Figure 1a) at the feet of the Vosges Mountains (48 ° 0.453 N, 7 ° 03.877 E, 310 m a.s.l.). INRAE selected this site for its youth and fast-growing characteristics, and it is managed by an official organism (Office National des Forêts).

(a) Location of the Hesse site in France.

(b) Location of the ICOS tower in the Hesse forest.

2.1.2 Vegetation

The forest originates from natural regeneration with trees aged 55 (±5) years old. It is composed of approximately 95% of European Beech, *Fagus sylvatica* L. The remainder is mainly *Carpinus betulus* L. (Granier et al. (2008)). Due to the dense canopy cover, understorey vegetation is sparse, and its influence can be disregarded (Granier et al. (2000)).

2.1.3 Soil

Three types of soils are present in the Hesse forest: pelosol, neoluvisol-redoxisol and fluviosol (Figure 2).

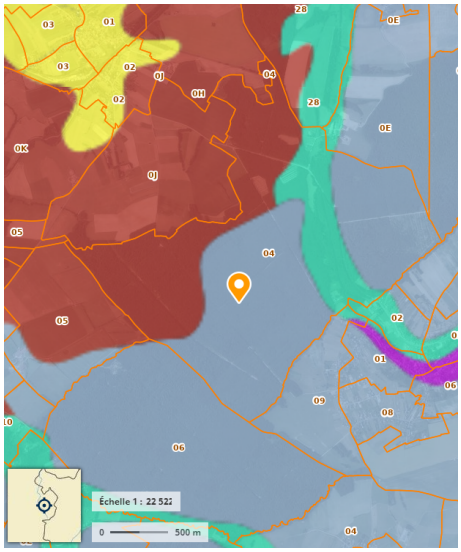

Figure 2: Soil map and cadastral parcels retrieved from ©IGN 2023 - www.geoportail.gouv.fr/mentions-legales. The orange flag indicates the location of the FRHes tower. The blue-grey area represents the pelosol, the red area represents the neoluvisols-redoxisols, and the turquoise area represents the fluviosols.

The main type is pelosol (81% of the footprint according to Montigny (2021-2022)), characterised by the Pelosolic S horizon (Sp) (Baize et al. (2009)). This horizon exceeds 30 cm in thickness and contains

more than 45% clay. It is always alkaline. Under forests, the Sp horizon is topped with horizon Ae/E, displaying a loamy or silty clay texture (less than 30% clay). It does not exceed 30 cm and is unsaturated, often acidic. The transition from Sp to the C horizon, where the aggregates are enlarging, is gradual. Wide and deep shrinkage cracks are marked in summer due to lower water content. They close during winter when water content increases. Those movements are coupled with landslides and compressions, yet there is no widespread pedoturbation. The surface horizons clog up during rainy periods, and water accumulates very shallowly. In the sloped areas, the water runs off and only a small amount infiltrates deeply to reach the C horizon. On the contrary, the dense summer structure and the clays' low useful water retention capacity lead to rapid drying of the surface horizons. Temporary waterlogging occurs at very shallow depths, starting from the base of the Ae/E horizon or sometimes even throughout the entire soil thickness. The resulting red or grey mottles indicative of oxidation-reduction processes are numerous in these horizons and the upper part of the Sp horizon (Spg). These waterlogging events and the high concentration of clay lead to establishment, survival, and growth challenges, affecting tree species. Under these conditions, the surface structure is precarious.

The second soil type is the neoluvisol-redoxisol, characterised by the intense hydromorphy appearing under 50cm from the surface related to a long waterlogging (Baize et al. (2009)). It is generally silty and has a high maximum water reserve and potential when depletion and clay leaching processes remain moderate. It has the principal references horizons E and BT from the luvisols. They are topped by a horizon A composed of organic and mineral matter.

Finally, the fluviosols are characterised by their development in recent deposited fluvial or lacustrine alluvial by transport, then sedimentation in an aqueous environment (Baize et al. (2009)). They are always in the lower position of the landscape, like valleys where they constitute river beds and are marked by the presence of a permanent or temporary alluvial phreatic table with strong oscillations. Therefore, they are waterlogged to varying degrees depending on the depth of the phreatic table. They have typical organic-mineral horizons (A horizons with bio macrostructures) or atypical horizons (Js horizons).

2.1.4 Climate

The climate is semi-continental temperate, characterised by warm summers and winters marked by frosts and snowfalls stretching down the plains, which become less frequent due to global warming. The annual rainfall under this climate is relatively high (Météo France (2023)). The annual averages for temperature and rainfall are 10.4°C and 919.6 mm, respectively, between 2001 and 2019. It usually rains for 120 to 140 days.

Figure 3 displays the main meteorological variables used in this thesis as ISBA inputs to predict the ecosystem-atmosphere exchange. The data are the gap-filled observations of the Hesse station for 2001 and 2002. Four seasons are discernible in the monthly average air temperature and in the monthly average daily cycle of incident direct shortwave radiation graphs, with lower values in winter, higher values in summer and a gradual increase and decrease in, respectively, spring and fall. Moreover, the monthly rainfall is heavier in winter. The annual average rainfall rate for those two years is 1067 mm/year. The amplitude of the monthly average diurnal cycle of carbon dioxide air concentration is wider between May and October due to the presence of leaves, which amplify the ecosystem-atmosphere exchanges through respiration and photosynthesis.

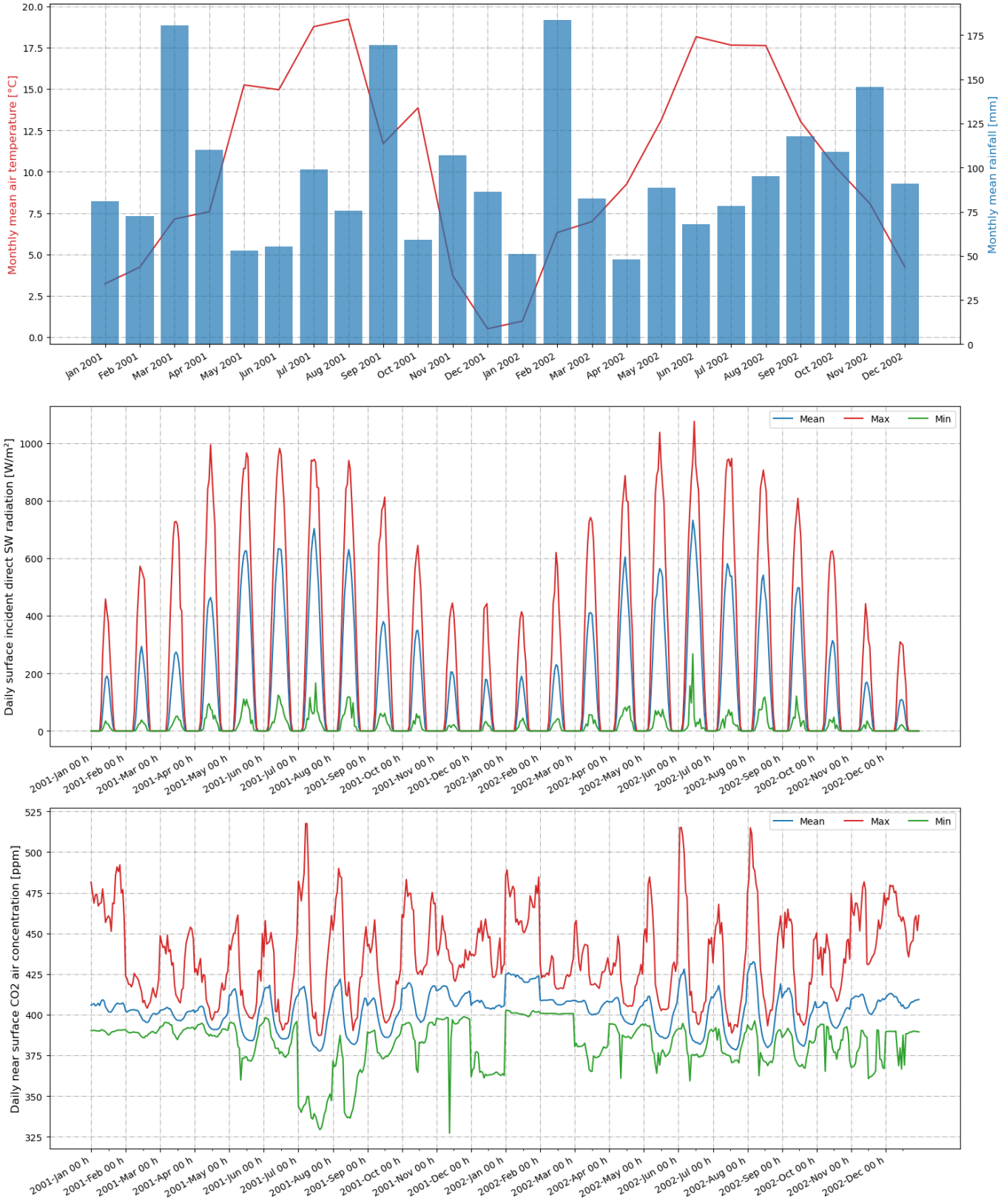

Figure 3: This figure displays the 2001 and 2002 time series of the monthly mean of the surface air temperature and the monthly cumulated rainfall (top), the incident shortwave mean diurnal cycle (middle) and the average diurnal cycle of the surface CO2 air concentration (bottom). The data are the gap-filled observations of the Hesse station for 2001 and 2002. The data used to compute those monthly averages are used as input for the simulations with ISBA.

2.1.5 Measurements and post-processing

Water and carbon dioxide fluxes were obtained using Eddy covariance. The Eddy-covariance technique is a micro-meteorological method with the advantages of a few hypotheses and a vast application spectrum (lia (2020)). It computes turbulent fluxes from the covariance between a gas's air concentrations (CO2, H2O) or temperature and the vertical wind's turbulent fluctuations. This technique necessitates simultaneous air gas concentrations, temperature, wind speed, and direction measurements at one point and with a high frequency (at least 20 Hz). The carbon dioxide and water vapour concentrations are measured with IRGA (LI-6262 LI-COR Inc., Lincoln, Nebraska, USA) and the temperature and wind characteristics are measured with a 3D Sonic anemometer (Solent R2, Gill Instruments Ltd., Lymington, UK) at the height of 23 m (in 2012). Those measurements are realised in the ecosystem and atmosphere boundary layer. It gathers information from the upstream area depending on the wind direction, velocity and turbulence. Simultaneously, the meteorological variables such as the air temperature and relative humidity (HMP155, Vaisala Oyj, Helsinki, Finland), the net radiation (pyrradiometer CNR4, Kipp& Zonen, Delft, The Nederlands) and the rainfall (pluviometer PREC-PrecMec 3029) were measured (Montigny (2021-2022)). The data are processed with Edisol software (University of Edinburgh, UK) following the prescription of Aubinet et al. (2012). It computes the outgoing carbon dioxide flux, the evapotranspiration and the sensible heat flux from the covariance between the vertical component of the wind speed and, respectively, the carbon dioxide concentration, the water vapour concentration and the air temperature. The Net Ecosystem Exchange (NEE) was computed using the fixed point method and then gap-filled by Jonathan Bitton. This method characterised the whole canopy based on a single carbon dioxide air concentration value rather than the concentration profile. While acknowledging it is biased and not recommended as it doesn't account for storage, this approach is deemed suitable for analysis at a monthly step. It was solely employed for flux partitioning, and the ISBA model doesn't calculate the photosynthetic variables with an air carbon concentration profile. The measured net carbon dioxide flux was used to benchmark the ISBA output as it is more accurate. The flux partitioning was computed with REddyProc (Wutzler et al. (2018)) by Jonathan Bitton with the nighttime method to obtain Gross Primary Production (GPP) and Ecosystem Respiration (R_{eco}). The nighttime method hypothesises the nighttime values of NEE correspond to R_{eco}; from that information, it computes the GPP. Due to the progress in ultrasonic wind meters and to the high performance and precision of CO2 analysers continuously monitoring the CO2 and water vapour fluxes, eddy covariance (EC) is the most efficient technique to measure the ecosystem-atmosphere exchange (Aubinet et al. (2012)).

A manual measurement of the leaf area index (LAI) is also realised by two different methodologies depending on the year. One of these methods is based on collecting falling leaves through litter traps. They are dried and weighed. A part of this sample dried is scanned through a planimeter and weighted to establish the specific leaf area. This mass-surface relationship and the total weight allowed computation of the total LAI of the season. The other method uses the LAI 2000 (LI-COR Inc., Lincoln, Nebraska, USA). It has a radiation sensor connected to the one at the top of the tower. The technician scans the area and takes a punctual measurement of the above and below canopy radiation. This measurement is based on the hypothesis of an exponential relationship between the quantity of photosynthetically active radiation lost and the LAI. It is realised by measuring the attenuation of the radiation at five zenith angles simultaneously, also giving information on the foliage orientation (Li-Cor Inc (1992)). The LAI used in this thesis is computed from the PPFD measurements using four dates: the budding, two weeks after budding (maximum LAI), the start of the senescence, and the complete fall of leaves ($LAI = 0$). This method produces a square LAI dynamic and does not consider thinning.
Additionally, the circumference (in mm) at chest height has been measured at different dates during the growing season since 1996. Within the 0.6 ha fenced experimental plot containing the flux tower at its centre, 60 plots were defined, and 12 were used for circumference measurements. The temporal frequency of these measurements varied from year to year. From 2014, circumferences were measured at least twice a year. These measurements, combined with allometric equations (established from data collected during thinning), were used to estimate biomass (Montigny (2021-2022)). As the study site is managed by the ONF (Office Nationale des Forêts), regular thinning is realised. To compare these data with the results of the ISBA, we have to assume that the trees cut during the thinning remain in place and keep their biomass constant (Appendix A).

Finally, the soil temperature (homemade thermocouples), the soil humidity (Thetaprobe ML2-UM-1, Delta-T Devices Ltd, Cambridge, England until 2017 and after EC-5 Campbell Scientific, Logan, UT), and the soil heat flux (HFP01SC, HukseFlux) were measured (Montigny (2021-2022); Lafont et al. (2014)). The soil organic carbon was measured between March and December 2004 during the research of Schrumpf et al. (2011). One hundred soil samples were taken on a regular grid at 30m distances in the tower's footprint. A corer with an inner diameter of 8.3 and 8.7cm (Eijkelkamp Agrisearch Equipment BV, Giesbeek, The Netherlands) was used for mineral soil sampling. It was driven with a motor hammer (Cobra Combi, Atlas Copco AB, Nacka, Sweden). The borehole's depth and the extracted core's length were measured and compared for the soil compaction estimation during coring. Soil cores were visually characterised, photographed and then sectioned into segments (0–5, 5–10, 10–20, 20–30, 30–40, 40–50, and 50–60cm).

2.2 Interaction Soil-Biosphere-Atmosphere (ISBA) model description

ISBA is the land surface model[1] of the National Meteorological Research Centre (CNRM, Météo-France) (Noilhan and Planton (1989); CNRM (2023); Delire et al. (2020)). Initially developed for weather forecasting purposes, ISBA undergoes continuous improvement, resulting in several coexisting versions (Joetzjer (2014)). It is part of the Surfex[2] platform, developed by CNRM, serving as a universal interface for various surface schemes (ocean, lakes, town, ...). The surface scheme representing the natural terrestrial surfaces is ISBA.

ISBA calculates the interactions between the surface and the atmosphere (Figure 4. At each model time step, each surface grid box receives essential meteorological parameters and ISBA computes the soil and vegetation temperature, soil moisture, and the upward energy, carbon and water fluxes. All this information serves as lower boundary conditions for atmospheric radiation and turbulent schemes. Each Surfex grid box comprises surfaces for nature, urban areas, sea/ocean, and lakes, determined using the global ECOCLIMAP database (Masson et al. (2003)). The Surfex fluxes represent weighted averages computed over different surface types.

ISBA can be paired with weather forecasting models or used with meteorological forcing, requiring variables such as radiative fluxes, precipitation, wind, vapour pressure deficit, and temperature. Programmed in Fortran, ISBA's input parameters and data are controlled by the OPTIONS.NAM file. ISBA-CC simulates various aspects of the terrestrial carbon cycle, including gross photosynthesis rate, dark leaf respiration, changes in leaf biomass, autotrophic and heterotrophic respiration, net primary production (NPP), and total plant biomass. A specific carbon allocation scheme is implemented to represent various biomass components, such as roots and wood, with turnover and respiration terms computed.

For this study, gap-filled observations from January 1^{st}, 1997, to December 31^{th}, 2011, from the Hesse flux tower served as meteorological forcing. Additional inputs included ecosystem classification and land surface parameters from Masson et al. (2003), soil texture (sand and clay content), and soil organic carbon measured in Hesse (Schrumpf et al. (2011)). The simulations provided localised model outputs as instantaneous values every half-hour, contrasting with observed data, representing average values of the previous half-hour.

The following description focuses on key equations governing exchange processes and provides a partial overview of the model's parameterisation based on Joetzjer (2014) and Le Moigne (2018).

[1] A land surface model describes the exchange between the ecosystem and the atmosphere and relevant parameters of the soil and vegetation.

[2] Surfex stands for 'surface externalisée,' as it externalizes physical parametrizations, preparation of specific surface parameters, and initialization of state variables for different models.

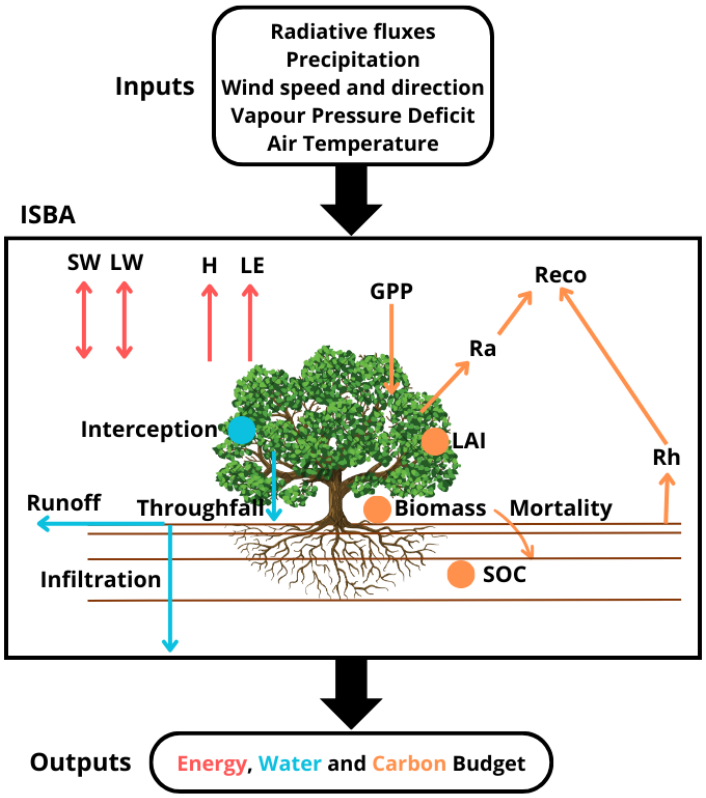

Figure 4: Conceptual diagram of the ISBA-CC surface model (Joetzjer (2014)).

2.2.1 Energy

The continental surface is the site of radiative and energetic exchanges with the atmosphere through turbulent phenomena and with the ground via heat conduction. Turbulent flows involve vertical movements of air heated by the surface (sensible heat, H in W/m^2) and water vapour evaporated or transpired by vegetation (latent heat, LE in W/m^2). Adhering to the principle of energy conservation, the energy balance is succinctly expressed as:

$$R_n = H + LE + G \tag{1}$$

where R_n denotes net radiation (W/m^2) and G represents soil heat conduction (W/m^2), the latter being contributed, to a lesser extent, by vegetation and snow cover.

2.2.1.1 Radiative balance

Solar radiation acts as the primary driver for surface-atmosphere exchanges. The atmosphere reflects and absorbs portions of solar radiation, allowing the remaining global incident radiation R_G (W/m^2) to reach the surface. Upon reaching the surface, a portion is reflected based on surface albedo (α), while the remainder is absorbed. Infrared radiation emitted by the atmosphere, R_A, is also partially absorbed by the surface. The residual infrared radiation follows the Stefan-Boltzmann law:

$$R_T = \epsilon \, \sigma_{SB} \, T_s^4 \tag{2}$$

Consequently, the radiative balance at the surface is given by

$$\begin{aligned} R_n &= SW + LW \\ SW &= R_G(1-\alpha) \\ LW &= \epsilon\,(R_A - \sigma_{SB} T_s^4) \end{aligned} \tag{3}$$

with:

SW : the shortwave radiation ($\mathrm{W/m^2}$)
LW : the longwave radiation ($\mathrm{W/m^2}$)
σ_{SB} : the Stefan-Boltzman constant ($5.67037442 \times 10^{-8}\ kg\,s^{-3}K^{-4}$)
α : the average albedo of a model grid-area
ϵ : the average emissivity
T_s : the surface temperature (K)

Snow exerts a substantial influence on surface characteristics, affecting both albedo and emissivity and on heat conduction fluxes due to its heightened insulating properties. Its presence reduces surface roughness and, with a large surface albedo impact on the net radiation budget, contributes to a notable decrease in turbulent transfer processes. However, this study exclusively concentrates on the growing season. Consequently, the total snow cover fraction and the frozen fraction of the surface layer are considered set to zero for a focused examination of energy dynamics during snow-free periods.

2.2.1.2 Turbulent fluxes

Latent Heat The water vapour flux E is computed using the liquid water evaporation from the soil surface E_g, the direct evaporation E_r from the fraction δ of the foliage covered by intercepted water (rainfall and dew) and the transpiration E_{tr} of the remaining part $(1-\delta)$ of the leaves.

$$\begin{aligned} LE &= L\,(E_g + E_{tr} + E_r) \\ E_g &= (1 - veg)\,\rho_a C_H V_a\,(h_u q_{sat}(T_s) - q_a) \\ E_{tr} &= veg\,\frac{1-\delta}{R_a + R_s}\,(q_{sat}(T_s) - q_a)) \\ E_r &= veg\,\frac{\delta}{R_a}\,(q_{sat}(T_s) - q_a) \end{aligned} \tag{4}$$

with:

L : the specific heat of evaporation (kJ/kg)
veg : the vegetation cover fraction, set to 0.95 for temperate forests
$q_{sat}(T_s)$: the saturated specific humidity at the surface temperature T_s (g/kg)
q_a : is the atmospheric specific humidity at the lowest atmospheric level
h_u : the relative humidity at the ground surface (set to 1 for dew flux; otherwise, it is calculated as a function of superficial soil moisture and the field capacity of liquid water, which is defined using the adjusted soil porosity)
C_H : the drag coefficient depending upon the thermal stability of the atmosphere (computed based on the formulation of Louis (1979) (Mascart et al. (1995)))
$R_a = (C_H V_a)^{-1}$: the aerodynamic resistance where V_a is the wind speed (m/s)
$R_s = (LAI\,g_{sc})^{-1}$: the surface resistance where g_s is the stomatal conductance

The fraction δ of the foliage covered by intercepted water is determined by a function incorporating the interception reservoir's water content and its maximum capacity, along with the Leaf Area Index (LAI, m^2/m^2) and a weighting function that accounts for vegetation height dependence. The reservoir's water content variation is further defined based on the precipitation rate at the top of the vegetation, the vegetation's evapotranspiration, and the runoff from the interception reservoir (refer to pages 138-139 of Le Moigne (2018)).

Sensible Heat

$$H = \rho_a c_p C_H V_a (T_s - T_a) \tag{5}$$

with:

c_p : the specific heat ($JK^{-1}kg^{-1}$)

ρ_a, V_a and T_a : the air density (kg/m^3), the wind speed (m/s), and the temperature (K) at the lowest atmospheric level, respectively

T_s : the surface temperature (K)

2.2.1.3 Soil heat conduction

The soil heat conduction G is linked to the surface temperature variation (Eq. 4.78b from Le Moigne (2018)).

2.2.2 Carbon

The version of ISBA (ISBA_bgc6) used incorporates an enhanced representation of gross primary production and autotrophic respiration for 16 plant functional types (PFTs) (Delire et al. (2020)). Annual changes in land cover drive fluctuations in PFTs, influencing carbon flux outcomes. The model also features a simplified representation of dissolved organic carbon leaching and transport to the ocean. However, the model applies the same phenology to all broadleaved trees, which leads to inaccurate predictions of carbon flows when the species does not follow this phenology.

$$NEE = R_{eco} - GPP \tag{6}$$

with $GPP = A_n + R_{d,leaf}$ When the Net Ecosystem Exchange (NEE) is negative, it signifies that the ecosystem functions as a carbon sink, storing more carbon than it releases into the atmosphere. Gross Primary Production quantifies the assimilation of carbon through photosynthesis. Ecosystem Respiration (R_{eco}) is the combined result of autotrophic and heterotrophic respiration. Autotrophic organisms produce the essential molecules to sustain heterotrophs (predominantly bacteria and fungi). Indeed, after assimilation by autotrophs, a portion of the organic matter is subsequently transferred to the soil and litter in the form of dead organic material (leaf fall, mortality). This organic matter becomes the substrate for heterotrophic respiration, leading to the release of CO_2 into the atmosphere. The gas exchange between vegetation and the atmosphere is regulated by stomata. The degree of stomatal opening is described by stomatal conductance (g_s), which is influenced by environmental factors. Factors positively correlated with stomatal conductance include soil water content, light energy availability, and air temperature. However, high air temperatures can exert a negative impact on stomatal conductance. Additionally, the vapour pressure deficit and atmospheric CO_2 concentration are associated with decreased stomatal conductance.

2.2.2.1 Photosynthesis model

The computation of canopy resistance occurs within the COTWORESTRESS routine, which can distinguish between drought-avoiding and drought-tolerant biomes. The photosynthesis model is called through this routine.

Normal water conditions The net carbon dioxide assimilation (A_n) within the canopy is based on various environmental factors, following the methodology proposed by Goudriaan et al. (1985). The CO_2 assimilation is limited by radiation (Eq. 7) and the air carbon dioxide concentration through the saturation equation 8.

$$A_n = (A_m + R_{d,leaf}) \left\{ 1 - \exp \left[- \left(\frac{\epsilon I_a}{A_m + R_{d,leaf}} \right) \right] \right\} - R_{d,leaf} \tag{7}$$

with:

I_a : the photosynthetically active radiation (PAR), assumed to be 48% of the incoming shortwave radiation at the top of the canopy

$R_{d,leaf}$: the leaf dark respiration (Eq. 15 in Section 2.2.2.2)

$\epsilon = \epsilon_0 \left(\frac{C_i - \Gamma}{C_i + 2\Gamma} \right)$: the initial quantum use efficiency

with ϵ_0, the maximum quantum use efficiency, fixed at 0.017

The photosynthesis dependence on temperature is represented through the Γ, g_m and $A_{m,max}$ whose values depend on the type of photosynthesis.

$$A_m = A_{m,max} \left[1 - \exp(\frac{-g_m^* (C_i - \Gamma)}{A_{m,max}} \right] \tag{8}$$

with:

$A_{m,max}$: the maximum net carbon dioxide assimilation defined as a function of the surface temperature and Q_{10} set at 2.0

g_m^* : the mesophyll conductance (with no soil water stress), fixed at 3 for deciduous broadleaf trees, which can be considered as a proxy for the Rubisco activity

C_i : the carbon dioxide concentration in the leaf

Γ : the carbon dioxide concentration at which assimilation compensates respiration, called CO_2 compensation concentration defined as a function of the surface temperature and Q_{10} set at 1.5

The carbon dioxide concentration in the leaf, C_i, is obtained through the air carbon dioxide concentration, C_a, controlled by the air humidity following the equations 9, 10.

$$C_i = f C_a + (1 - f)\Gamma \tag{9}$$

The ratio f varies according to the air humidity deficit D_s (g/kg).

$$f = f_0^* \left(1 - \frac{D_s}{D_{max}^*} \right) + f_{min} \left(\frac{D_s}{D_{max}^*} \right) \tag{10}$$

with:

D^*_{max} : the maximum specific humidity deficit of the air tolerated by the vegetation (with no soil water stress), fixed at 109 for deciduous broadleaf trees

D_s : the actual deficit

f^*_0 : the value of f if there is no saturation deficit (with no soil water stress, $D_s = 0$), fixed at 0.51 for deciduous broadleaf trees

$f_{min} = \frac{g_c}{g_c + g^*_m}$ with g_c, the cuticular conductance, fixed at 0.15 for deciduous broadleaf trees

When $D_s > D^*_{max}$, the plant closes its stomata to avoid water losses (Section 1.2). Both D^*_{max} and f^*_0 are vegetation and photosynthesis type dependent.

The estimation of stomatal conductance to CO_2, g_{sc}, employs a flux-gradient relationship adjusted to incorporate the impact of a specific humidity deficit on the stomatal aperture. The initial approximation, g_{sc}, is provided by:

$$g_{sc} = \frac{A_n - A_{min}\left[\frac{D_s}{D_{max^*}}\left(\frac{A_n+R_{d,leaf}}{A_m+R_{d,leaf}}\right)\right] + R_{d,leaf}\left[1 - \left(\frac{A_n+R_{d,leaf}}{A_m+R_{d,leaf}}\right)\right]}{C_a - C_i} \tag{11}$$

The residual photosynthesis rate at full light intensity, A_{min}, associated with cuticular transfers when stomata are closed due to high specific humidity deficit, is defined as a function of the mesophyll conductance, the value of C_i at maximum specific humidity deficit ($D_s = D^*_{max}$) and the CO_2 compensation concentration (Γ).

To account for the interaction between transpiration and assimilation, the leaf transpiration is regulated by g_{sc}. Initially, the estimation of stomatal conductance to water vapour is derived from the ratio of water vapour and CO_2 diffusivity, followed by a refined adjustment considering the interaction between CO_2 and water vapour diffusion. The process involves iterative enhancements for improved accuracy.

Response to drought For deciduous broadleaf trees, the strategy in response to soil moisture stress in the model is drought-tolerant. This strategy aims to resist stress through a more efficient root water uptake or a more rapid growing cycle. Within this strategy, two regimes are distinguished. One regime involves moderate stress, characterized by the normalised soil moisture f_2 exceeding the critical value f_{2c}. The other indicates severe stress, where the normalised soil moisture f_2 is under the critical value f_{2c}. The critical value is set at 0.3 for global modelling. However, this value can be adjusted for local modelling based on available data.

Calvet et al. (2004) discusses the soil moisture stress response by high vegetation. For the drought-tolerant strategy, as stress occurs, f_0 remains at its unstressed value and the g_m decreases until the critical soil moisture level is attained (Eq. 12). It leads to a decline of the water use efficiency.

$$g_m = g^*_m - (g^*_m - g^N_m)\frac{1 - f_2}{1 - f_{2c}} \tag{12}$$

with:

g^N_m : the value of g_m given by: $\ln(g^*_m) = 2.8 - 7f^*_0$

$f_2 = \frac{\overline{w} - w_{wilt}}{w_{fc} - w_{wilt}}$: the effect of soil moisture stress on mesophyll conductance g^*_m

with :

w : the soil moisture

w_{wilt} : the wilting point

w_{fc} : the field capacity

If the stress drops below the critical threshold (indicating severe stress), there is an increase in f_0 and a simultaneous decrease in g_m according to the equation 13.

$$g_m = g_m^N \frac{f_2}{f_{2c}} \tag{13}$$

The following relationship between D^*_{max} and g^*_m was established based on findings from Calvet et al. (2004).

$$D^*_{max} = -37.97 \ln(g^*_m) + 150.4 \tag{14}$$

Extrapolation from leaf to canopy As the photosynthesis model computes net CO_2 assimilation at the leaf level, integration is required to extrapolate the canopy. For this purpose, the following assumptions are made: the variables D_s, T_s, and C_a remain constant within the canopy, along with the model parameters. The model considers that the fraction δ of the foliage covered by intercepted water does not assimilate CO_2, and it accounts for the vertical attenuation of incoming shortwave radiation within the canopy according to Carrer et al. 2013 (cited by Joetzjer (2014)). Additionally, the leaf respiration exhibits a vertical profile influenced by an exponential leaf nitrogen distribution proposed by Joetzjer (2014). In this context, as the Leaf Area Index (LAI) increases, the effect of the exponential leaf nitrogen distribution causes a decrease in leaf respiration. To extend this leaf respiration profile to the entire canopy, it is multiplied by the reciprocal of LAI (1/LAI). This multiplication serves as a scaling factor, allowing the representation of the overall leaf respiration across the canopy, accounting for the variation induced by the changing LAI values.

The tile-specific skin temperature T_s is determined by solving each tile's surface energy balance. In COTWORESTRESS, canopy-level D_s (surface vapour pressure deficit) is computed using a flux-gradient relationship from D_s at the reference atmospheric level, utilising the aerodynamic resistance (r_a) and the water vapour flux from the previous time step. Nonetheless, the model sets the surface CO_2 concentration (C_s) at the atmospheric concentration (C_a).

2.2.2.2 Ecosystem respiration model

Autotrophic respiration scheme Autotrophic respiration consists of plant parts' respiration uptaking carbon dioxide to create glucose. Growth respiration enables the production of new plant tissues and maintenance respiration to support existing biomass. The sum of both respirations corresponds to autotrophic respiration (dark respiration + photorespiration).

The ISBA model employed for autotrophic respiration in this thesis follows the PS+R approach proposed by Joetzjer (2014), which characterizes respiration for the following biomass reservoir (Section 2.2.2.3).

The leaf dark respiration is expressed by the equation:

$$R_{d,leaf} = \frac{A_m}{9} \exp(-k_n \, LAI) \frac{1}{LAI} \tag{15}$$

where k_n represents the photosynthetic capacity profile within the canopy, set to 0.2 (Bonan et al., 2012, cited by Joetzjer, 2014).

The respiration of the active structural biomass is modelled as:

$$R_2 = B_2 \beta f(T) \tag{16}$$

with β set to 1.25, and $f(T)$ computed using the Arrhenius temperature function based on the temperature of the biomass pool, a temperature sensitivity factor, and a reference temperature (25°C).

For below-ground structural biomass respiration (R_4), it is given by:

$$R_4 = B_4 \beta f(T) \tag{17}$$

where β is set to 0.0125.

Similarly, the above-ground biomass respiration (R_5) is represented as:

$$R_5 = B_5 \lambda_{sap} \beta_{wood} f(T) \tag{18}$$

with β_{wood} set to 0.0125, and λ_{sap} denoting the fraction of sapwood estimated using assumed sap velocity, maximum transpiration rate, and tree height (Kucharik et al., 2000, cited by Joetzjer (2014)). No respiration is associated with the heartwood biomass (B6).

Heterotrophic respiration scheme The soil respiration approach employed in ISBA-CC is based on a modification of an early version of the CENTURY model proposed by Parton et al. (1987, 1988) (cited by Le Moigne (2018)). CENTURY models the dynamics of carbon flux and storage, capturing their interplay with the soil-plant system's water and nutrient cycles. Originally designed to simulate crops and grasslands in the US Great Plains, CENTURY features a plant growth module and a representation of soil organic matter. CENTURY has undergone enhancements and validations for various vegetation types and biomes, evolving into a widely acknowledged model within the international scientific community.

The ISBA-CC model simulates numerous soil carbon pools with distinct organic matter categories, residence times and locations (Figure 5). Additionally, it accounts for the carbon fluxes moving between these various pools.

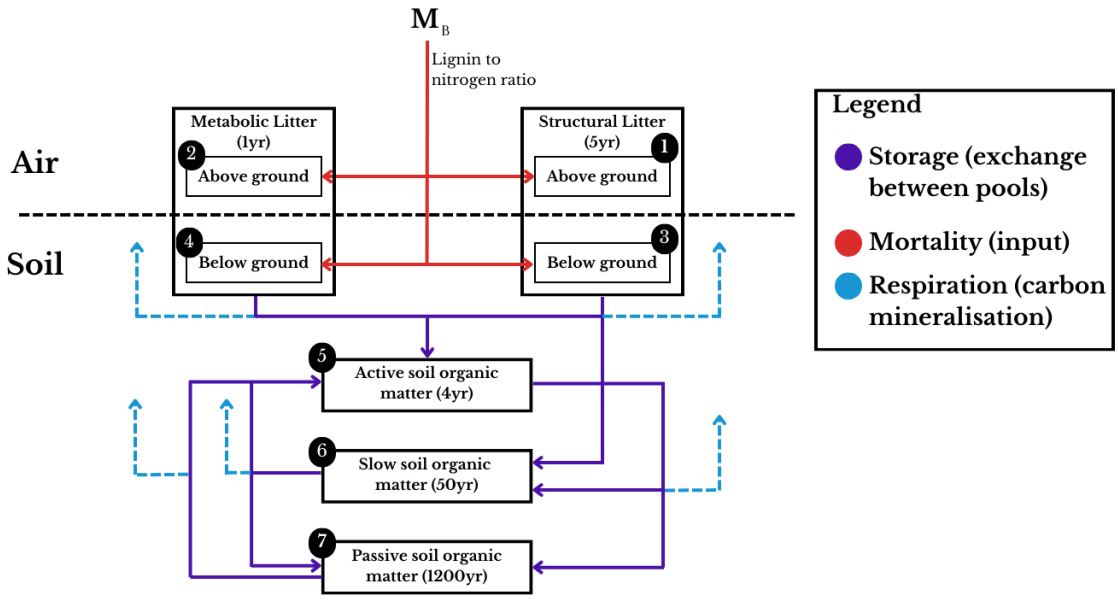

Figure 5: Scheme of the heterotrophic respiration of ISBA-CC based on the CENTURY model. The soil carbon pools are depicted alongside input mortality terms, carbon exchange fluxes between the pools, and mineralised carbon fluxes. The sum of all the elements in the latter is the heterotrophic respiration. The number associated with each pool is the indices i used to shorten the label.

Four litter categories are modelled (Figure 5), distinguished by their residence times. Two surface litter compartments are fueled by mortality fluxes from above-ground biomass, and two soil litter compartments are supplied by the below-ground biomass mortality fluxes. This distinction is supplemented

by the separation of structural and metabolic litter. Structural litter consists of lignin and cellulose from dead vegetation residues, with a residence time of 2 to 5 years. Metabolic litter comprises more labile organic components with a residence time of 0,1 to 1 year Parton et al. (1988) (cited by Le Moigne (2018)). The allocation of vegetation residues to these categories depends on the lignin-to-nitrogen ratio (L/N), with high ratios favouring more structural litter. Conversely to the CENTURY model, ISBA-CC uses constant L/N values fixed at 8,8 for the leaf biomass compartment and 14 for the remaining biomass reservoirs.

Soil organic carbon is represented by three pools calculated by the Century model: active, slow, and passive, characterised by different residence times, fuelled by the organic matter (OM) produced by the litter compartments (Figure 5) and representing different chemical states of soil OM. The active pool depicts the soil microorganisms and the decomposition products of short residence time (2 to 4 years). The slow pool within the model represents soil organic molecules or components characterized by a residence time ranging from 20 to 50 years, while the passive pool represents those with a residence time ranging from 800 to 1200 years (Parton et al. (1988) cited by Le Moigne (2018)). ISBA decomposition rate is determined by climatic conditions (such as soil moisture and temperature), soil physical properties (e.g., texture, depth), and the chemical composition of the substrate (i.e., the carbon, nitrogen, and lignin content of residues). However, the soil OM model does not depict the soil profile's carbon content. Consequently, ISBA-CC employs surface and root-zone soil moisture and corresponding temperatures for different components.

A fraction of the decomposed organic matter releases carbon dioxide into the atmosphere due to mineralisation through respiration. The remaining fraction is transferred to the various soil carbon pools depending on their respective levels of resistance to decomposition. The decomposition process of the structural litter contributes to the respiration flux and facilitates the stabilisation of carbon within a soil organic carbon pool—either active or slow depending on the content of lignin and the type of litter. The decomposition of the metabolic litter reservoirs contributes to the respiration flux and carbon stabilisation within the active soil organic carbon pool. The active soil organic carbon decomposition supplies the respiration flux, and the slow and passive soil organic carbon pools, depending on the soil texture. The decomposition of the slow organic carbon pool provides the respiration flux, and the active and the passive soil organic carbon pools, depending on the soil texture. Finally, the decomposition of the passive soil organic carbon delivers the respiration flux (55%) and the active soil organic carbon pool (45%).

2.2.2.3 Allocation scheme

ISBA-CC allocation scheme simulates six biomass pools (kg/m^2), comprising four above-ground and two below-ground pools (Le Moigne (2018); Gibelin et al. (2008); Joetzjer (2014)):

1. B_L: Leaf biomass,
2. $B_{S,act}$: Active structural biomass, assimilated to new twigs and linked to B_L through nitrogen dilution,
3. $B_{S,pas}$: Passive structural biomass, a numeric reservoir corresponding to a small and negligible amount of carbon, present for numerical stability purposes
4. $B_{S,bg}$: Below-ground structural biomass depicting the roots sapwood and fine roots (non-woody).
5. $B_{W,ag}$: Above-ground biomass characterising the trunk, bough and branches
6. $B_{W,bg}$: Below-ground biomass depicting the heartwood roots

The $B_{S,pas}$ reservoir is used to store the biomass released by $B_{S,act}$ during the senescence phase. Figure 6 represents the plant carbon reservoirs and the different fluxes. The changes in all biomass

reservoirs are computed once a day, following the equation 19. The biomass reservoir evolution (B) is driven by an incoming allocation term A_B, a respiration carbon loss term R_B and a turnover term D_B (kg/m^2).

$$\Delta B = A_B - D_B - R_B \tag{19}$$

Allocation to other reservoirs than B_L is furnished by the storage term (as shown in Figure 6). It is derived from the decline term depending on the reservoir, the plant type and the growth phase. When the decline isn't transferred to another compartment, it is entirely converted to mortality. During the growing phase, all the decline terms are converted to storage (except the woody terms). In contrast, during the senescence phase, a fraction is reallocated, and the other is considered as mortality restocking the litter. Decline occurs when the biomass decline exceeds daily net CO_2 assimilation. The biomass decline depends on the leaf biomass time of residence and the minimum Leaf Area Index. Senescence is mimicked by a decline over a sufficient number of consecutive days, where the decline in biomass exceeds the daily net assimilation of CO_2, to reach the leaf biomass content according to LAI_{min}.

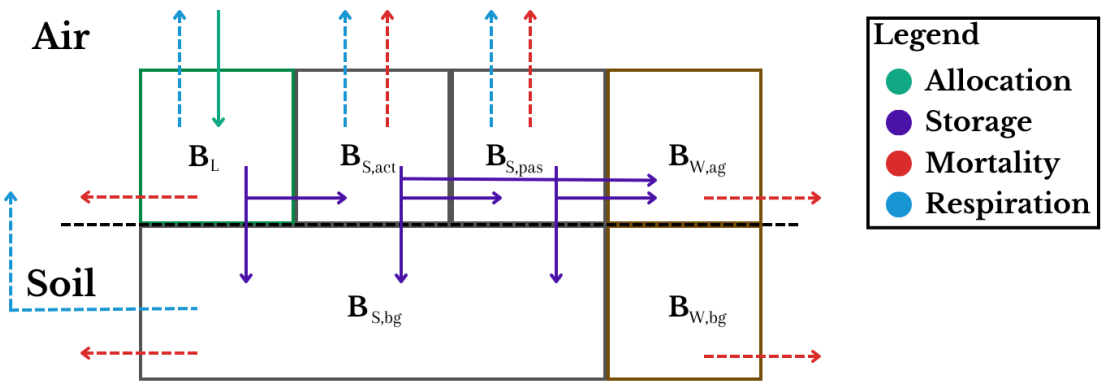

Figure 6: Plant carbon reservoirs and fluxes schematic representation for a woody vegetation. Input fluxes are indicated by solid arrows, and output fluxes are indicated by dashed arrows. The autotrophic respiration is the sum of all the biomass respiration terms.

Leaf Area Index (LAI) The Leaf Area Index (LAI) dynamic representation is achieved through a simple growth model, as outlined by Calvet et al. (1998) (cited by Le Moigne (2018)). It computes the leaf biomass and the LAI interactively, allowing the consideration of interannual variability, particularly during droughts. The interactive LAI calculation relies on the evolution of biomass resulting from photosynthetic activity. The photosynthesis model is invoked from COTWORES (or COTWORESTRESS) for all present vegetation tiles (in this case, deciduous broadleaf forest), and LAI is determined using the equation 20. To initiate carbon dioxide assimilation for vegetation after an unfavourable conditions period, a minimum LAI, LAI_{min}, is required, with a specific value of 0.3 for deciduous broadleaf trees.

The nitrogen dilution concept from Lemaire and Gastal (1997) (cited by Le Moigne (2018)) is applied to account for plant morphology. It provides the law correlating plant nitrogen N_L in non-limiting N-supply conditions with the accumulated aboveground dry matter.

$$SLA = \frac{LAI}{B_L} = eN_L + f \tag{20}$$

with:

LAI : the leaf area index

B_L : the leaf biomass reservoir

SLA : the specific leaf area ratio, which depends on the leaf nitrogen concentration

e & f : the plasticity parameters, 4.83 and 2.53 respectively for deciduous broadleaf trees

N_L : the nitrogen content in leaves

The nitrogen content in leaves N_L and, consequently, the SLA, may decrease with an increase in CO_2 air concentration. The nitrogen dilution constrains the CO_2 fertilisation effect, which increases vegetation biomass. In the study of Calvet et al. (2008), nitrogen dilution is considered by parameterising the alteration in leaf nitrogen mass-based concentration (N_L) in response to a rise in CO_2 concentration. The sensitivity of leaf nitrogen concentration to variations in CO_2 concentration was assessed using a meta-analysis based on the assumption that, on average, a CO_2-doubling leads to an 18% reduction in N_L (Le Moigne (2018)). Yet, the N_L response is influenced by various factors. A change in CO_2 concentration from C_1 to C_2 induces a corresponding change in N_L from N_{L1} to N_{L2} as follows:

$$\ln\left(\frac{N_{L2}}{N_{L1}}\right) = -a\exp\left[b - \frac{N_{L1}}{N_{Lmax}}\right]\ln\left(\frac{C_1}{C_2}\right) \tag{21}$$

with:

$a = 0.048$, $N_{Lmax} = 6.3\%$ and $b = 0.75DF + 1.1PPFD + \dfrac{T_a}{23}$

where DF = 1 for deciduous forests,

PPFD is the average photosynthetically active solar radiation reaching the leaf within the vegetation canopy

Additionally, the SLA and the nitrogen content in leaves vary depending on the height and development stage of the tree. However, this effect is neglected by the ISBA model, which represents an average tree.

Respiration representation The computation of respiration terms occurs at the model's time step, dt, and is aggregated at the daily time step, $\Delta t = 1day$. For each biomass reservoir, the respiration is computed through the equations described in Section 2.2.2.2.

Decline term The decline term represents the biomass decrease due to mortality and carbon reallocation to other plant elements (storage) through the equation 22.

$$D_B = B(1 - e^{-\frac{\Delta t}{\tau}}) = M_B + S_B \tag{22}$$

where τ is the residence time (in days).

Mortality results from higher decline values than the storage term, if any. It supplies the above- and below-ground litter compartments of the soil organic matter scheme.

The residence time differs from one compartment to another. The structure biomass is determined with τ_M and refers to the maximum effective life expectancy, which depends on the vegetation type. It is set at 230 days for deciduous broadleaf trees. For the leaf biomass, the daily leaf span time τ_{B_L} is computed based on the photosynthesis efficiency (ratio of the maximum leaf net assimilation (A_n) reached on the previous day and the optimum leaf net assimilation (A_n) multiplied by the maximum effective life expectancy). A constraint on leaf span time is imposed to avoid extreme biomass loss when A_n is low: $\tau \geq \frac{\tau_M}{10}$. The B_S, act and B_S, bg residence time is τ_M and for B_S, pas it's $\tau_M/4$. For the woody biomass reservoir ($B_{W,ag}$ and $B_{W,bg}$), the life expectancy τ_w equals 40 years for broadleaf deciduous forests.

Allocation of leaf biomass Allocation to leaf biomass, A_{B_L}, is determined by gross assimilation (photosynthesis), including net carbon assimilation (A_n) and dark respiration ($R_{d,leaf}$ for maintenance and growth). A_{B_L} can be negative at nighttime.

$$A_{B_L} = \sum_{dt} 10^{-6}\frac{M_C}{P_c M_{CO_2}}(A_n + R_{d,leaf})dt \tag{23}$$

where:

P_c : the fraction of carbon of the dry biomass, assumed to be 40%

$M_C \& M_{CO_2}$: the molecular weights of carbon and CO2 (12 and 44 g mol^{-1}, respectively)

All the assimilated carbon is initially allocated to the leaves and subsequently cascades to other biomass reservoirs.

$$B_T = \left(\frac{B_L}{c}\right)^{\frac{1}{1-a}} \tag{24}$$

with a and c set at 0.38 and 0.314 respectively.

During the growing phase (assimilation > turnover), B_L evolution is computed through the equation 19. Then, it is used to compute the total biomass B_T with the equation 24. As this law was established for herbaceous plants and cereals, B_T represents B_L + $B_{S,act}$. Obtaining $B_{S,act}$ from B_T and B_L is therefore straightforward. As the nitrogen dilution law 24 does not conserve mass, the variation in B_T does not correspond to the net carbon balance of the leaves. A correction is therefore applied to limit the variation in B_T to the carbon actually available.

During the senescence (assimilation < turnover), the nitrogen dilution law isn't verified anymore. The computation of B_L is still done using the equation 19 but $B_{S,act}$ only loses mass.

Even if the B_L increases, the model can simulate a $B_{S,act}$ decrease (after a temporary senescence phase or a cut). In that case, the lost biomass supplies $B_{S,pas}$, a buffer reservoir to avoid the irreversible loss of $B_{S,act}$ through mortality.

The B_L, $B_{S,act}$, and $B_{S,pas}$ supply the $B_{S,bg}$ reservoir during the growing phase, while it is supplied solely by S_{B_L} during senescence phase. The woody reservoirs, $B_{W,ag}$ and $B_{W,bg}$ are supplied by $S_{B_{S,act}}$ and $S_{B_{S,act}}$, $S_{B_{S,bg}}$, respectively.

2.3 Spin-up

Before conducting any simulations, a spin-up process is essential to equilibrate carbon stocks and fluxes with the imposed climate. The spin-up consists of a series of prediction iterations based on the existing atmospheric forcing from 1997 to 2011. During this process, spin-up parameters are activated, and the number of output files is constrained for system optimisation while monitoring the carbon reservoirs (biomass and SOC). The spin-up process uses the SURFOUT file as the initial input (PREP), necessitating a modification of the starting date to correspond to the existing atmospheric forcing. Indeed, since the SURFOUT file's date corresponds to the last day of the atmospheric forcing, it requires adjustment to iterate the simulation of carbon fluxes on the 15 years of atmospheric forcing. The model is run 17 times using the 15 years of atmospheric forcing each time, totalling 255 years. While this duration is sufficient for stabilising biomass pools, it falls short for soil carbon pools which does not pose a substantial issue (Appendix C). Given that the values already exceed observations, allowing soil carbon to stabilise could lead to overestimating heterotrophic respiration.

After the spin-up, the file PGD.txt, which remains the same for all simulations, and the file PREP.txt of the 17$^{\text{th}}$ iteration are used to run the simulations.

2.4 Description of the different simulations

The model was executed from 1997 to 2011, coinciding with the availability of measured data. However, for detailed presentation and discussion, the years 2001, 2002, and 2003 have been specifically chosen.

Meteorological R_{eco}rds, despite notable precipitation in the fall and winter of 2002, classified 2001 and 2002 as climatically average (Chaste et al. (2023); échelon central) et al. (2004)). Notably, during these years, there were no observed instances of heat, drought, or hydrous stress damage to the trees. The inclusion of the year 2003 in the analysis serves the purpose of examining the model's response to drought conditions. Although the drought in 2003 was not severe, it occurred unusually early, at the beginning of July. It is pertinent to highlight that the effective replenishment of water tables by rainfall in 2002 ensured sufficient soil water reserves at the onset of the 2003 growing season. Nevertheless, 2003 proved exceptionally dry, ranking among the two driest years in the past 60 years (Granier et al. (2008)).

2.4.1 Simulation with parameters at reference values (SimREF)

A first simulation was conducted with the input parameters at the reference values (Table 1). Those must be given in the OPTIONS.NAM file to configure the ongoing simulation. Other parameters, such as coordinates and Plant Functional Type (PFT), are also encoded. The model remained unaltered during this simulation, serving the purpose of getting a control simulation. This unmodified state allowed for a comprehensive evaluation of its performance in the unique context of a European Beech forest. Given that the model encapsulates the phenological characteristics common to all deciduous forests, its application to a beech forest becomes particularly insightful, considering the distinct budding processes that differentiate beech from other deciduous trees. This approach facilitated the identification of potential issues necessitating rectification or adjustments.

Table 1: The input parameters reference values. The topsoil refers to the soil's 30^{th} cm, and the subsoil refers to the first meter of the soil (including the topsoil layer).

		Reference values
Roots depth (m)		2
Soil depth (m)		3
Soil texture	**Clay content (%)**	34.4
	Sand content (%)	8
SOC topsoil (%)		1.28
SOC subsoil (%)		0.94

2.4.2 Carbon allocation scheme

After running the simulation with parameters at the reference values, significant issues were exposed (Section 4.2.1). The first avenue was adjusting the carbon allocation scheme's module (Section 2.2.2.3) to address those issues. For this purpose, it was replicated in Python to allow fine-tuning outside the main program. The replication was limited to the pathways used for this study site. As mentioned in section 2.2.2.2, the forests (NCB) are represented by six biomass reservoirs, unlike the grasslands (NIT), which are characterised by four reservoirs. Concerning the soil organic carbon, the CENTURY bulk method (CNT) which determines the litter quantity and represents a single soil reservoir, was used instead of the vertical discretisation method. The flow chart of the allocation scheme module is located within the appendix B. Several options to modify the carbon allocation scheme's module were considered, such as imposing an observed LAI, adjusting leaf life expectancy using a phenological model, or adapting the model to trigger budburst based on photoperiod and temperature or degree days. However, these adjustments were not implemented due to the challenges highlighted in Section 4.2.2.

2.4.3 Simulation with reference parameters values and LAI forcing (SimLAI)

An alternative approach to enhance the modelling of the European Beech forest is to integrate the measured Leaf Area Index (LAI) directly as inputs, as opposed to relying on the Interactions between Soil, Biosphere, and Atmosphere (ISBA) model to simulate it. Specifically, the subroutine responsible for simulating LAI and photosynthesis underwent adjustments to incorporate the measured LAI as input in the OFFLINE executable. Consequently, photosynthesis was computed using the provided LAI input. The daily net assimilation, derived from this imposed LAI, is used in the allocation subroutine, which governs the evolution of leaf biomass and the biomass of the other five reservoirs (see section 2.2.2.3). However, it's important to note that the leaf biomass resulting from this subroutine is not directly forced by the LAI inputs. While influenced by the LAI inputs through net assimilation, the leaf biomass reservoir is not directly correlated with the LAI input. In this scenario, LAI and leaf biomass do not follow Equation 20.

2.4.4 Simulation with reference parameters values, LAI forcing and modified leaf biomass allocation scheme (SimLAIB1)

As a subsequent step, the measured LAI was imposed, as described earlier, while Equation 20 was applied to ensure coherence between leaf biomass and LAI at the onset of the allocation scheme. This adjustment involved selectively modifying the subroutine responsible for carbon allocation, requiring it to utilise the LAI input for improved accuracy. However, it's crucial to acknowledge that this adjustment disrupts the inherent logic of the allocation scheme, leading to an incomplete carbon conservation. This is also observed in the SimLAI scenario.

2.5 Convergence and quality indexes

An index of convergence (the relative root mean square error (rRMSE, Eq. 25)) and a quality index (the Nash-Sutcliffe model Efficiency (NSE, Eq. 26)) were used to assess the accuracy, the fitness and the exactitude of the energy and carbon fluxes' prediction. The NSE is recommended while analysing a model with day and night modelling and temporal variation. These indices were calculated based on the monthly average diurnal cycle, including nighttime values, for the analysis of 2001 and 2002. For the drought of 2003, they were computed on the daily mean. The program used to compute them was developed on Python 3.9.7 64-bit.

$$rRMSE = \frac{\sqrt{\sum_N^i \frac{(o_i - d_i)^2}{N}}}{\sqrt{\sum_N^i \frac{d_i^2}{N}}} \tag{25}$$

$$NSE = 1 - \frac{\sum_N^i (o_i - d_i)^2}{\sum_N^i (d_i - \overline{d})^2} \tag{26}$$

with:

o_i : the model output
d_i : the measured data
N : the number of observations

An NSE equal to one reveals a perfect fit of the model. When it's under 0.5, the model doesn't represent correctly the observed data. The rRMSE indicates an ideal fit when it's close to 0, suggesting that the model's predictions closely match the magnitude of the observed values. If the rRMSE is above 0.5, it indicates a poor fit, suggesting that the model differs substantially from the measured values.

3 Results

3.1 Spin-up

As mentioned in Section 2.2.2.2, the ISBA model incorporates six carbon reservoirs and four soil organic carbon stocks. Detailed output from the spin-up, including biomass reservoirs and total soil organic carbon reservoir data, is provided in Appendix C.

Table 2 presents the spin-up final values for the above- and below-ground biomass, contrasting them with the measured biomass from the 2th of January 1996. Strikingly, ISBA's biomass values are five times higher than the measured counterparts. Leaf biomass is excluded due to the absence of available measurements.

Table 2: Measured biomass of the 2th of January 1996 compared to the last biomass values of the spin-up

Biomass reservoirs	**Last biomass values of the spin-up (gC/m²)**	**Measured biomass (gC/m²)**
Above-ground (BIOM2 + BIOM5)	22834	3900
Below-ground (BIOM4 + BIOM6)	3472	823
Total biomass	26306	5584

Table 3 gives the spin-up last values of the soil organic carbon reservoirs. The total soil organic carbon (SOC) represents the global trend of the three different SOC components (Appendix C). Owing to the extended residence time of soil organic molecules within the passive pool (refer to Section 2.2.2.2), the total SOC does not reach a plateau even after the 17th iteration. Although the SOC has not yet stabilised, values are already higher than the measured values reported by Schrumpf et al. (2011).

To allow a meaningful comparison between measured values and ISBA outputs, a ratio was applied to the measured values. This ratio, determined by the total SOC and three other reservoirs, allows allocation of the total SOC measured in 2004 according to ISBA dynamics. Table 3 presents the values for different SOC reservoirs, revealing that ISBA's SOC values are three times higher than the measured values.

Table 3: This table encompasses soil organic carbon values obtained from the last values of the spin-up, average measured total SOC values in 2004 (n=100, Schrumpf et al. (2011)), and values obtained for distinct reservoirs through the application of SOC ratios to measured values.

Sources	**Depth (cm)**	**SOCT (g/m²)**	**SOC1 (g/m²)**	**SOC2 (g/m²)**	**SOC3 (g/m²)**
Schrumpf	0-5	1161	80	840	240
	5-10	943	65	683	195
	10-30	2769	192	2004	573
	30-60	1814	126	1313	376
	0-60	6687	463	4840	1384
Last values of the spin-up, ISBA	0-100	21951	1519	15888	4545

3.2 Model evaluation

In the following, all the time series of energy fluxes or carbon fluxes are presented as time series of monthly averaged diurnal cycles.

Table 4: Relative root mean square error convergence index and Nash-Sutcliff efficiency quality index were computed for each simulation to assess model performance for the years 2001 and 2002. These indices were calculated based on the monthly average diurnal cycle, including nighttime values.

Index	**Simulation**	R_{net}	H	LE	NEE	GPP	R_{eco}
rRMSE	**SimREF**	1,69 $\times 10^{-6}$	2,86 $\times 10^{-5}$	1,23 $\times 10^{-5}$	1,24 $\times 10^{-4}$	6,14 $\times 10^{-5}$	7,51 $\times 10^{-5}$
	SimLAI	1,69 $\times 10^{-6}$	2,83 $\times 10^{-5}$	1,29 $\times 10^{-5}$	1,10 $\times 10^{-4}$	5,57 $\times 10^{-5}$	8,44 $\times 10^{-5}$
	SimLAIB1	1,69 $\times 10^{-6}$	2,83 $\times 10^{-5}$	1,29 $\times 10^{-5}$	9,44 $\times 10^{-5}$	5,57 $\times 10^{-5}$	9,32 $\times 10^{-5}$
NSE	**SimREF**	0,966	0,319	0,827	0,742	0,811	0,786
	SimLAI	0,966	0,331	0,810	0,799	0,844	0,729
	SimLAIB1	0,966	0,331	0,810	0,851	0,844	0,670

3.2.1 Net radiation and Leaf area index (LAI)

Before delving into the analysis of the flux output from simulations, it is important to evaluate two essential variables: net radiation and leaf area index (LAI). Ensuring the accurate representation of these variables is crucial, given their roles in influencing various physical and biological processes within the ecosystem. Net radiation serves as the energy input for both physical (Eq. 1) and photosynthetic processes (Eq. 7), while leaf area index significantly impacts photosynthesis and evapotranspiration by scaling up to the ecosystem level. Any inaccuracies in the representations of these variables may lead to biases in the simulated fluxes.

The accuracy of net radiation predictions by the simulations is visually confirmed in Figure 7a. This observation is further substantiated by examining the quality and convergence indexes (Table 4). The NSE reveals a perfect fit of the simulations and the rRMSE indicates the predicted and observed values are remarkably close to identical, with only a minor underestimation of the prediction observed during the summer months. It is important to note only the SimLAI and SimLAIB1 have identical values of net radiation and, thus, of albedo.

Figure 7b displays the simulated and measured leaf area index. Noticeably, the simulation with reference parameters (SimREF) diverges from the others. Indeed, SimREF simulates LAI based on specific leaf area and leaf biomass (Eq. 20), resulting in a distinct pattern. It retains leaves until the winter, causing a slower increase in LAI compared to the other simulations. Accordingly to their parametrisation, the simulations with imposed LAI values (SimLAI and SimLAIB1) exhibit a noticeable overlap with the observed LAI (Section 2.4). This overlapping was expected as the observed LAI was forced into the photosynthesis subroutine which computes the LAI output. Indeed, even though SimLAI still simulates the LAI for the input in the carbon allocation scheme, it is not provided in the model outputs. Due to the computation of the observed LAI, the LAI of SimLAI and SimLAIB1 trend is straightforward (Section 2.1.5). Despite these differences, the overall range of LAI values remains consistent. Consequently, the disparity between simulated and observed LAI primarily resides in the temporal scale rather than the magnitude of the values.

3.2.2 Turbulent fluxes

In Figures 8a and 9a, the monthly average diurnal cycle of observed and predicted sensible heat flux (W/m^2) and latent heat flux, respectively, is presented for the period between January 2001 and December 2002. Notably, the predictions of SimLAI and SimLAIB1 are found to be equal, as evidenced

by both the quality and convergence indexes presented in Table 4. Henceforth, these simulations will be collectively referred to as SimLAI-LAIB1.

3.2.2.1 Latent heat

Despite an overall good fit indicated by the quality index and consistent magnitudes suggested by the convergence index (Table 4), a nuanced pattern emerges. Figure 8a reveals that SimREF consistently overestimates latent flux throughout the year, while SimLAI-LAIB1 exhibits this overestimation mainly during the summer months except in September 2001 when there was an overestimate of more than 100 W/m^2 and in April 2002 an underestimate of around 20 W/m^2. Although the dynamic of observations is better represented by SimLAI-LAIB1, SimREF surprisingly outperformed SimLAI-LAIB1 according to the indexes (Table 4). This unexpected outcome is further corroborated by the comparison in Figure 8b, where SimREF aligns more closely with the 1:1 line in high latent heat flux values, whereas SimLAI-LAIB1 shows greater aggregation around the 1:1 line in lower values.

The latent heat computation involves three water vapour fluxes (Equation 4). The evaporation from the soil surface equals 0 for the whole period (2001-2002). The direct evaporation from the fraction δ of the foliage covered by intercepted water ranges from -2.24 W/m^2 to 48.96 W/m^2 for the SimREF and from -2.71 W/m^2 to 47.46 W/m^2 for the SimLAI-LAIB1. The transpiration of the 1-δ part of the leaves ranges from 0.03 W/m^2 to 227.45 W/m^2 for the SimREF and from 0.04 W/m^2 to 237.11 W/m^2 for the SimLAI-LAIB1.

3.2.2.2 Sensible heat

Turning to sensible heat flux (Figure 9a), all simulations exhibit an overestimation of peaks and baseline, with variations in the degree of overestimation. The overestimation from June to September is more pronounced for SimREF, while in November and December, SimLAI-LAIB1 exhibits greater overestimation. Despite the precision indicated by the convergence index, NSE values below 0.5 suggest inaccuracies in the predictions (Table 4). This inaccuracy is further evident in Figure 9b, where most points lie above the 1:1 line. However, all simulations effectively capture the increase and decrease of sensible heat. Besides, SimLAI and SimLAIB1 better capture the general trend observed and have a better prediction of observations than SimREF, as indicated by the indexes in Table 4.

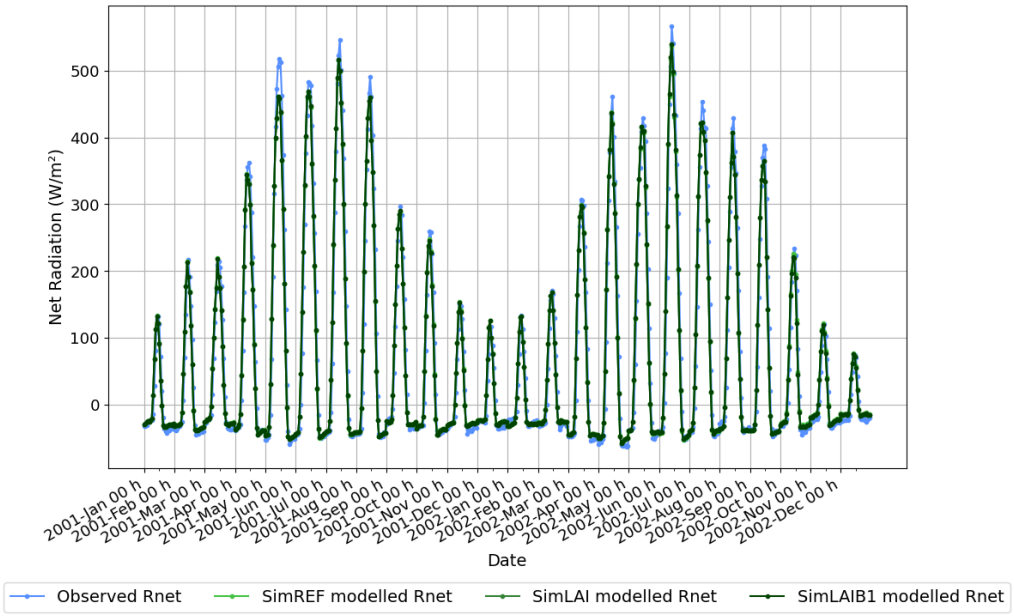

(a) Net radiation (W/m^2) for the different simulations.

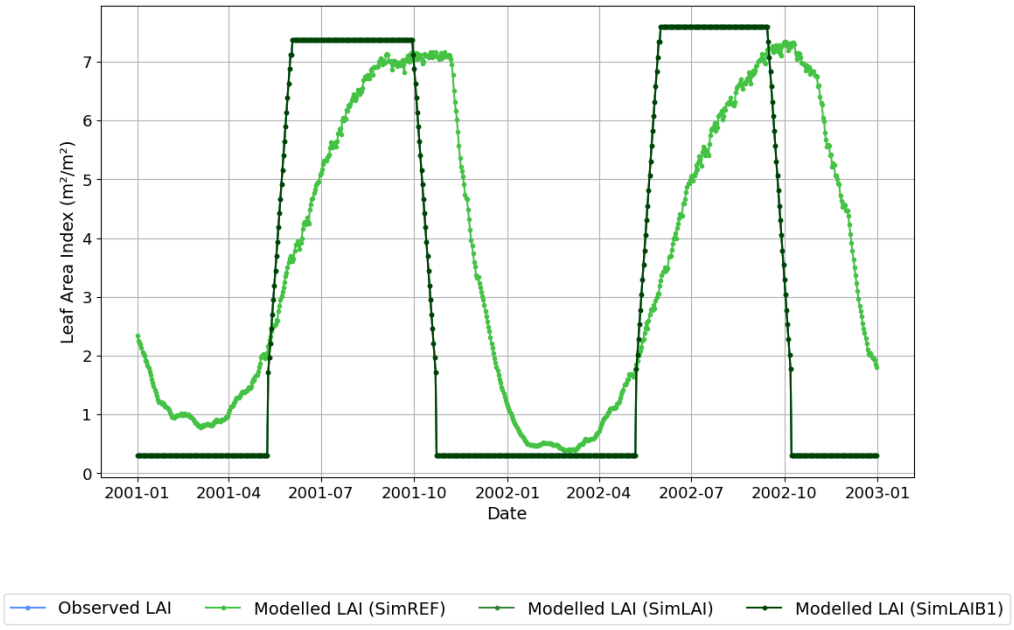

(b) Leaf area index (m^2/m^2) for the different simulations.

Figure 7: Graphs of modelled and measured average day per month Net radiation (W/m^2) and the daily Leaf area index (m^2/m^2) for the different simulations.

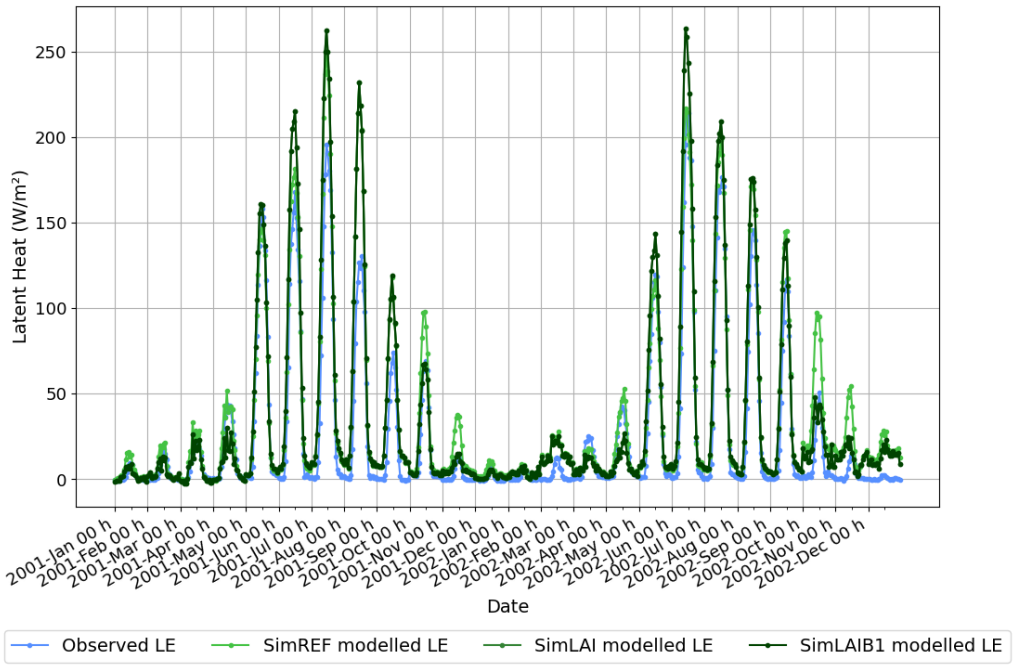

(a) Graphs of the monthly average diurnal cycle of observed and simulated Latent Heat Flux (W/m^2) for 2001 and 2002.

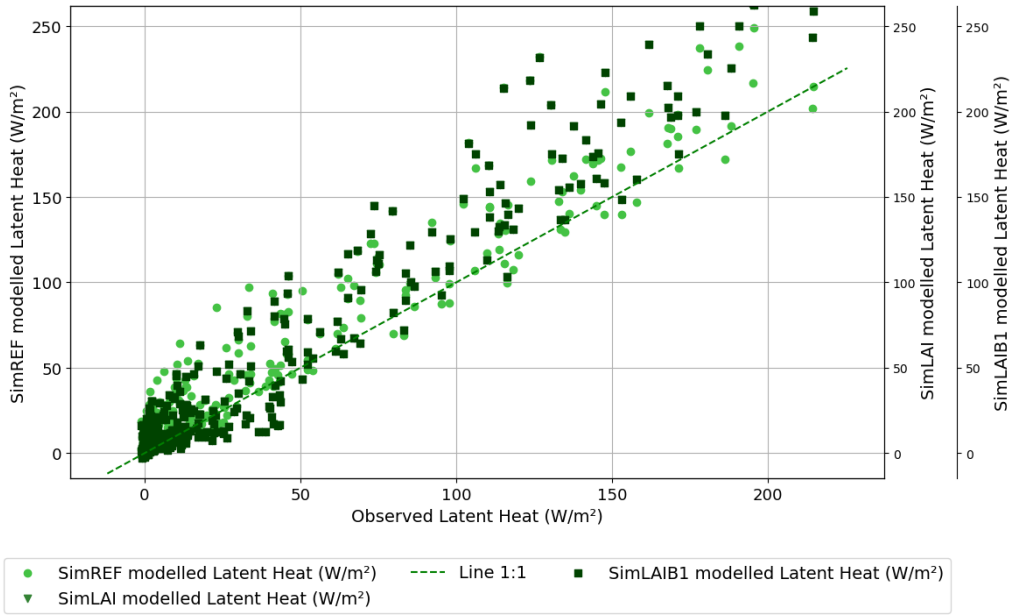

(b) Comparison of observed and simulated Latent Heat Flux (W/m^2) for 2001 and 2002.

Figure 8: Graphs of simulated and observed monthly average diurnal cycle Latent Heat Flux (W/m^2) for the different simulations.

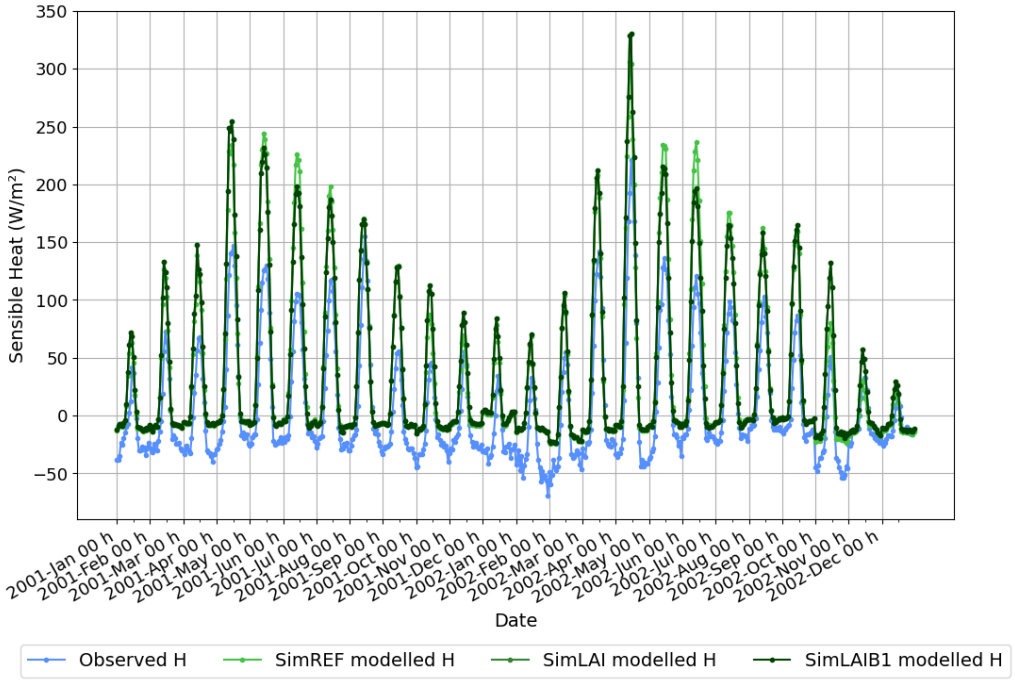

(a) Graphs of the monthly average diurnal cycle of observed and simulated Sensible Heat Flux (W/m^2) for 2001 and 2002.

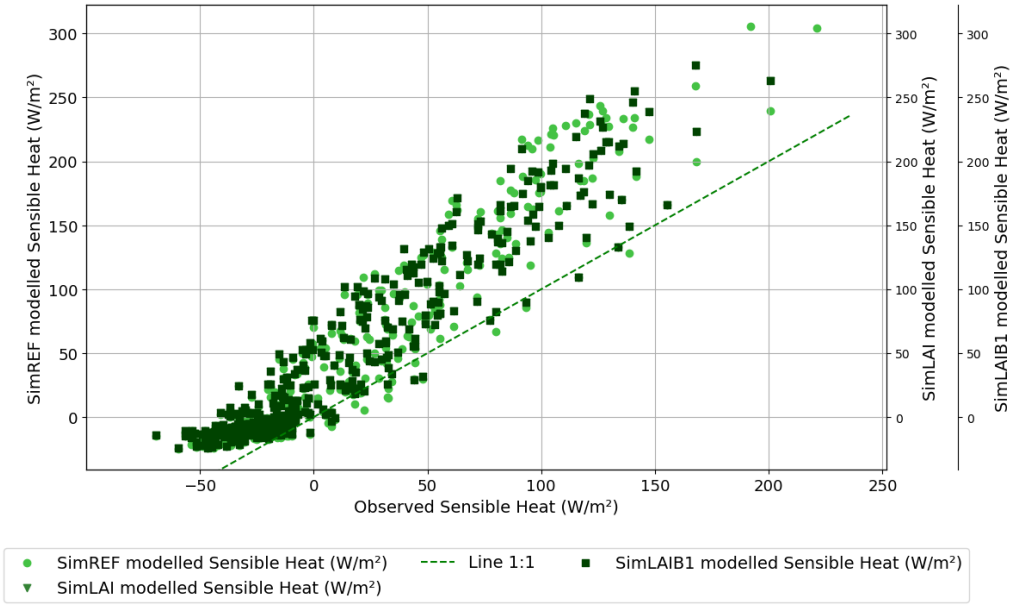

(b) Comparison of observed and simulated Sensible Heat Flux (W/m^2) for 2001 and 2002.

Figure 9: Graphs of simulated and observed monthly average diurnal cycle Sensible Heat Flux (W/m^2) for the different simulations.

3.2.3 Carbon

Carbon fluxes are calculated within the photosynthesis subroutine, as detailed in Section 2.2.2. The outputs are used in the allocation scheme subroutine to assess the biomass reservoir evolution (Section 2.2.2.3).

3.2.3.1 Ecosystem Respiration (R_{eco})

The evaluation of ecosystem respiration performance reveals a gradient from higher to lower accuracy among the simulations, with SimREF exhibiting the highest performance, followed by SimLAI, and SimLAIB1. Visual confirmation of these trends is presented in Figure 10b, where, at lower values, SimLAIB1 surrounds the 1:1 line, while the others slightly overestimate it. Beyond a flux of 3 µmol/m²s, SimLAIB1 generally underestimates R_{eco}, whereas the others demonstrate superior performance. However, after reaching 6.5 µmol/m²s, all three simulations consistently underestimate ecosystem respiration. This observed trend is complemented by quantitative measures, as depicted in Table 4, where both the convergence index (rRMSE) and quality index (NSE) exhibit a decline in the same order, indicating a diminishing accuracy in representing ecosystem respiration across the simulations. It is noteworthy that despite these diminishing trends, the NSE remains above the threshold, and the rRMSE tends towards 0, signifying a good fit of the predictions.

Considering the temporal aspect of ecosystem respiration flux predictions, all simulations exhibit peaks of greater amplitude than the observations and tend to underestimate summer respiration (Figure 10a). Throughout the other seasons, ecosystem respiration is generally overestimated, with SimLAIB1 values being relatively closer to the observations. Interestingly, SimLAIB1 even underestimates ecosystem respiration during specific periods, such as from October 2001 to January 2002 and September 2002 to November 2002. Moreover, the ecosystem respiration values for the SimLAIB1 simulation exhibit two significant drops in May 2001 and 2002, coinciding with the transition from LAI_{min} to elevated values, marking the period of budburst.

3.2.3.2 Gross Primary Production (GPP)

Transitioning to the predictions of Gross Primary Production (GPP), contrary to ecosystem respiration, incorporating observed LAI significantly improves the model's fit to observed GPP values. The NSE values surpass the threshold, and the rRMSE tends towards 0, indicating a robust fit of GPP predictions across all simulations (Table 4). However, the adjustment made in SimLAIB1 did not impact the performance of GPP predictions. Consequently, akin to the turbulent fluxes, SimLAI and SimLAIB1 exhibit identical outputs.

Examining Figure 11b, SimLAI-LAIB1 mainly underestimates the GPP values. This pattern is also evident in the temporal perspective depicted in Figure 11a. In contrast, SimREF tends to exhibit a slight overestimation of GPP at lower values. Around 7 µmol/m²s, it maintains proximity to the 1:1 line but eventually underestimates GPP for values beyond 13 µmol/m²s (Figure 11b). This behaviour is further illustrated in the temporal graph (Figure 11a), where SimREF effectively captures small peaks but experiences overestimation in April and November 2001, as well as in the peaks from October to December 2002.

3.2.3.3 Net Ecosystem Exchange (NEE)

Moving on to Net Ecosystem Exchange (NEE), the inclusion of observed LAI in the photosynthesis subroutine enhances not only GPP predictions but also improves NEE representation. The NSE values surpass the threshold, and the rRMSE tends towards 0, indicating a robust fit of NEE predictions across all simulations (Table 4). There is a gradient in performance among the simulations, with SimLAIB1 exhibiting the highest accuracy and fitness, followed by SimLAI and SimREF.

In positive NEE values, all three simulations exhibit a slight overestimation, with SimLAIB1 displaying a comparatively smaller deviation than the others (Figure 12b). However, the points are more concentrated near the 1:1 line than at negative values, where the points are scattered. Despite this, SimLAIB1 is closer to the 1:1 line for negative values. These trends are also evident in Figure 12a,

where negative peaks are underestimated, but the baseline (in positive values) is overestimated. Once again, SimLAIB1 shows closer alignment with observed values. Predictions from SimLAI and SimREF are comparable for values constituting the baseline. However, SimREF deviates from this trend in April 2001-2002, and from October to December 2001-2002, where it overestimates the negative drop.

Similar to the patterns observed in ecosystem respiration predictions, SimLAIB1 experiences notable NEE drops in May 2001 and 2002, aligning with the transition from LAI_{min} to increased values during budburst.

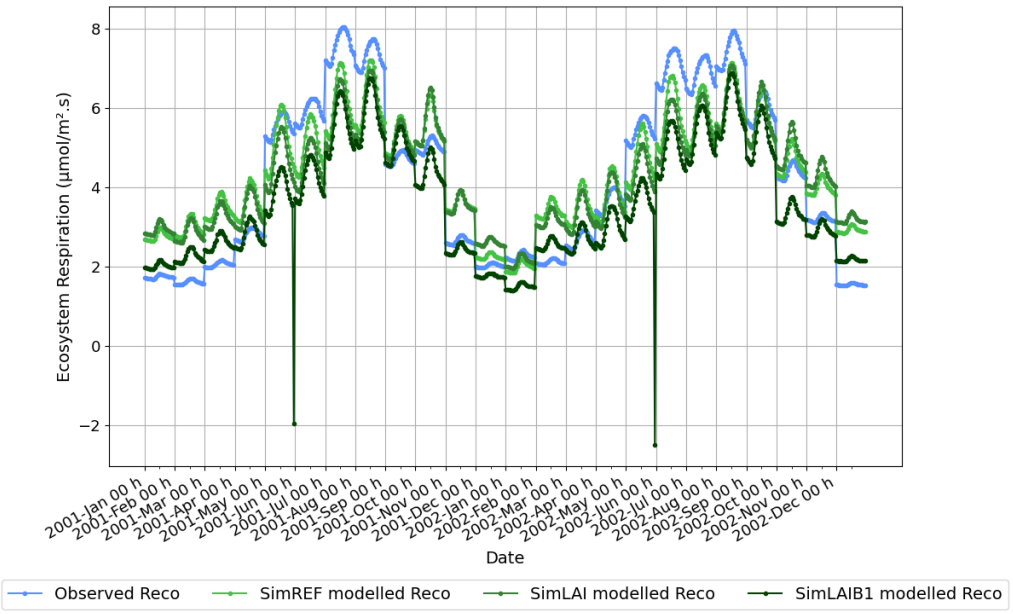

(a) Graphs of the monthly average diurnal cycle of observed and simulated Ecosystem respiration (µmol/m^{2}s) for 2001 and 2002.

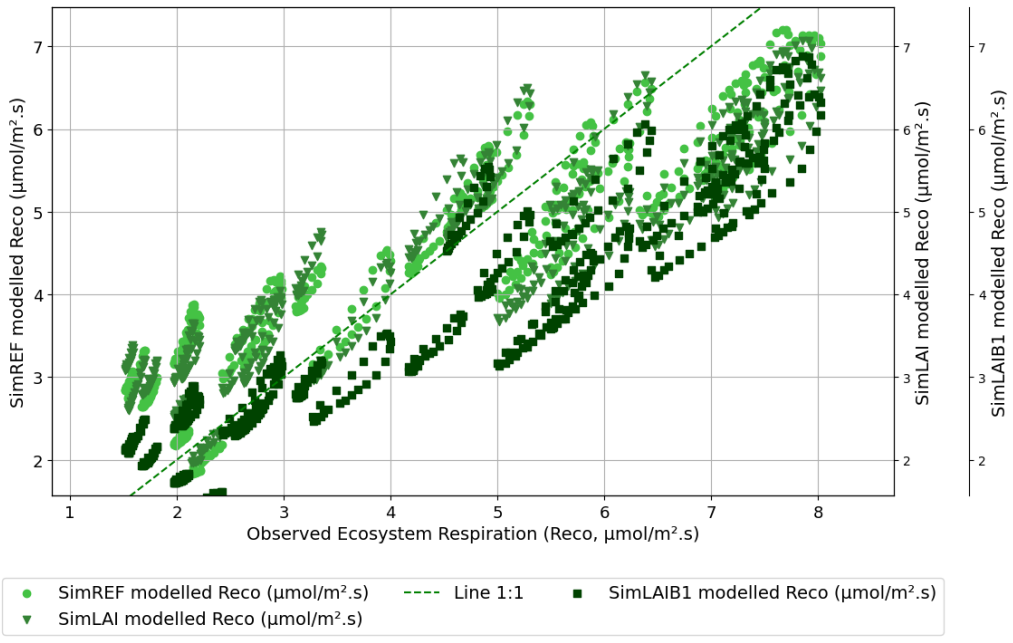

(b) Comparison of observed and simulated Ecosystem respiration (µmol/m^{2}s) for 2001 and 2002.

Figure 10: Graphs of simulated and observed monthly average diurnal cycle Ecosystem respiration (µmol/m^{2}s) for the different simulations.

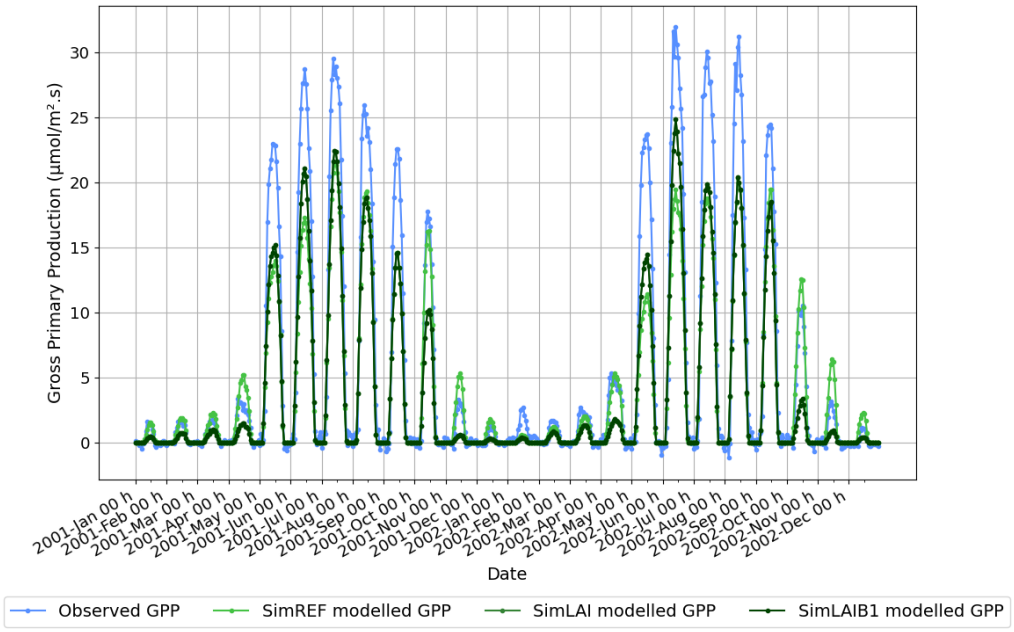

(a) Graphs of the monthly average diurnal cycle of observed and simulated Gross Primary Production (µmol/m^{2}s) for 2001 and 2002.

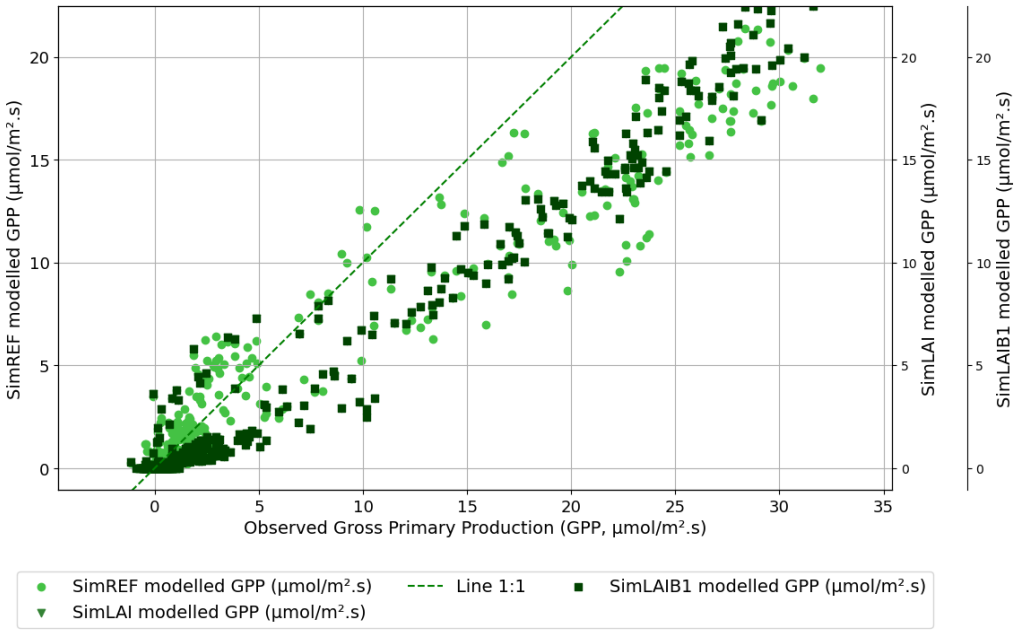

(b) Comparison of observed and simulated Gross Primary Production (µmol/m^{2}s) for 2001 and 2002.

Figure 11: Graphs of simulated and observed monthly average diurnal cycle Gross Primary Production (µmol/m^{2}s) for the different simulations.

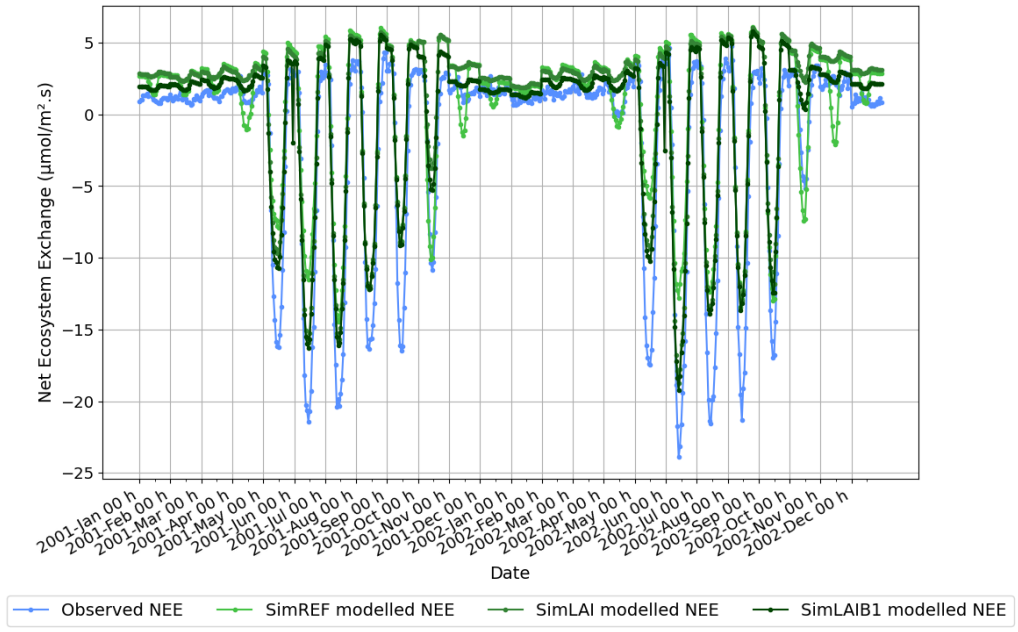

(a) Graphs of the monthly average diurnal cycle of observed and simulated Net ecosystem exchange (µmol/m^{2}s) for 2001 and 2002.

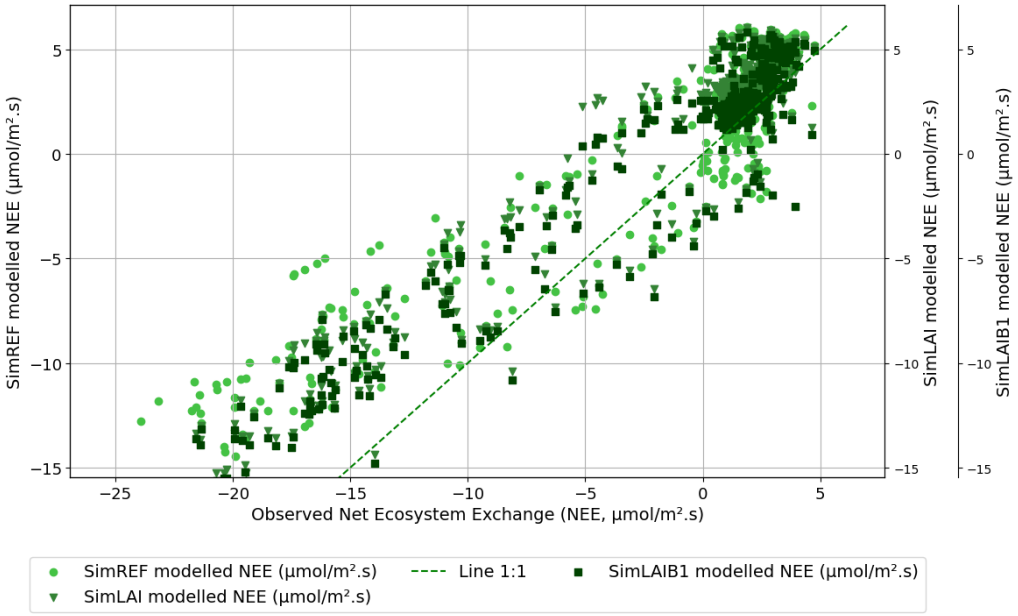

(b) Comparison of observed and simulated Net ecosystem exchange (µmol/m^{2}s) for 2001 and 2002.

Figure 12: Graphs of simulated and observed monthly average diurnal cycle Net ecosystem exchange (µmol/m^{2}s) for the different simulations.

3.2.4 Biomass reservoirs

As shown in Section 3.1, the initial biomass values for the prediction period (1997 until 2011) are significantly different from the observations as discussed in Section 4.1. Consequently, the focus of the biomass reservoir predictions analysis will be on the dynamics rather than the absolute biomass values, allowing for a comparison of accretion patterns.

Between September 2001 and March 2002, no measurements were taken. Furthermore, outside this period, measurements were not conducted daily. Hence, the predictions from the simulations were filtered to align with this gap.

Figure 13 displays the daily accretion of the observed and predicted total biomass (gC/m^2), excluding leaf biomass. During the growth period, the total biomass exhibits an increase which is steeper for SimLAIB1. Its accretion magnitude surpasses that of the other two simulations. Although all simulations' accretion starts at the same time as the observations, SimLAIB1 matches the amplitude of the observed accretion despite its sharper increase. During winter, observed total biomass decreases by approximately 30 gC/m^2, while the simulations total biomass becomes negative, with SimLAI and SimREF showing a greater loss.

Figure 14a and 14b depicts the daily accretion of the observed and predicted above-ground (excluding leaf biomass) and below-ground biomass (gC/m^2), respectively. The predicted above-ground biomass experiences a more pronounced decrease in winter than the below-ground biomass. Throughout the growth period, the predicted above-ground biomass increases, while the below-ground biomass decreases. In fact, the predicted below-ground biomass mainly decreases except for April and September where it increases slightly. SimLAIB1 is the only simulation predicting an increase in below-ground biomass during winter.

Finally, Figure 15 shows the predicted Leaf Biomass reservoir (gC/m^2) of the three simulations during 2001 and 2002. SimREF and SimLAI exhibit closely aligned dynamics, although SimREF values are higher. Both simulations preserve leaf biomass until winter. On the other hand, SimLAIB1 closely follows the dynamics of the imposed LAI and gradually accumulates carbon, like the other two simulations. Nevertheless, SimLAIB1 shows three abrupt peaks—one in June 2001 and two in May and July 2002.

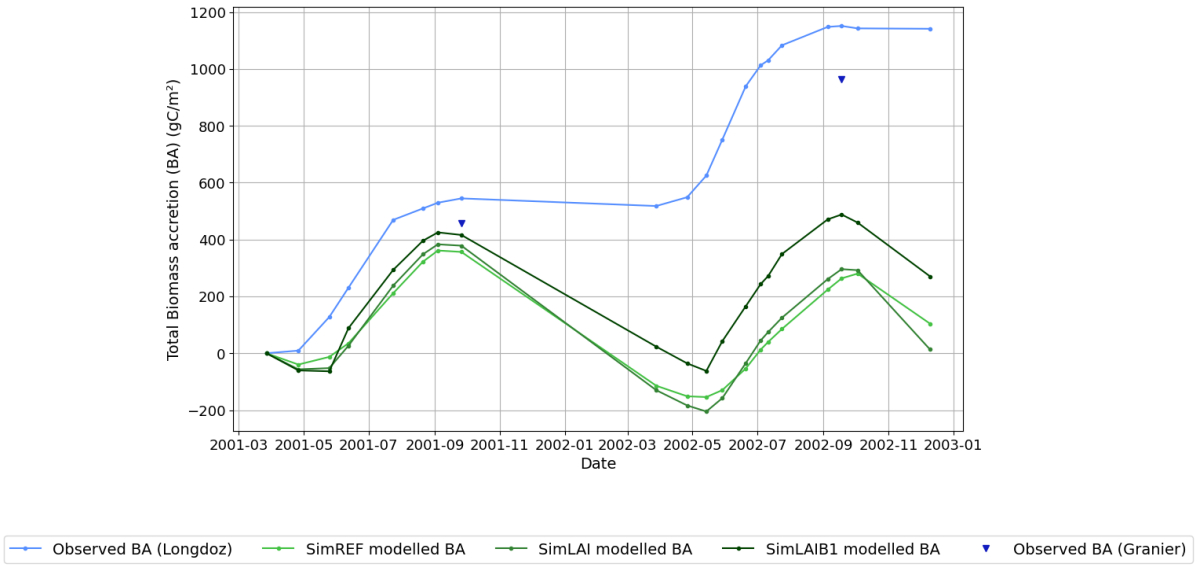

Figure 13: Graphs of the daily accretion of total biomass (gC/m^2) of the observation (provided by Bernard Longdoz) and the three simulations for 2001 and 2002. The observations from Granier et al. (2008) are also displayed (blue upside-down triangle).

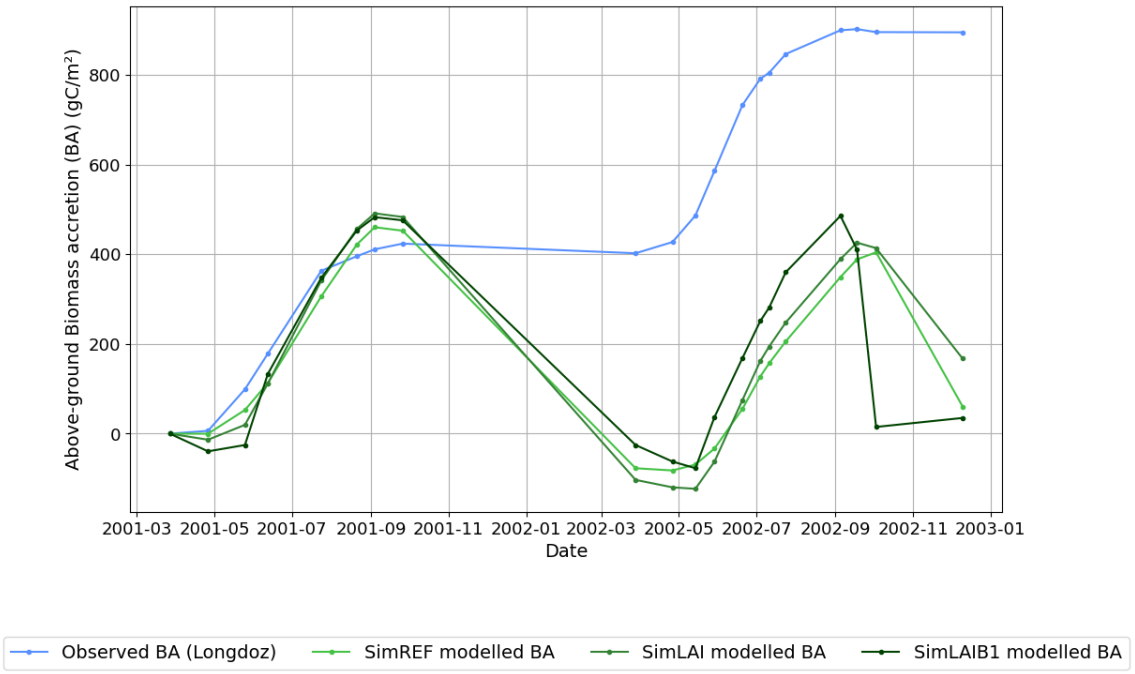

(a) Graphs of the daily accretion of observed and predicted above-ground biomass (gC/m^2) for 2001 and 2002.

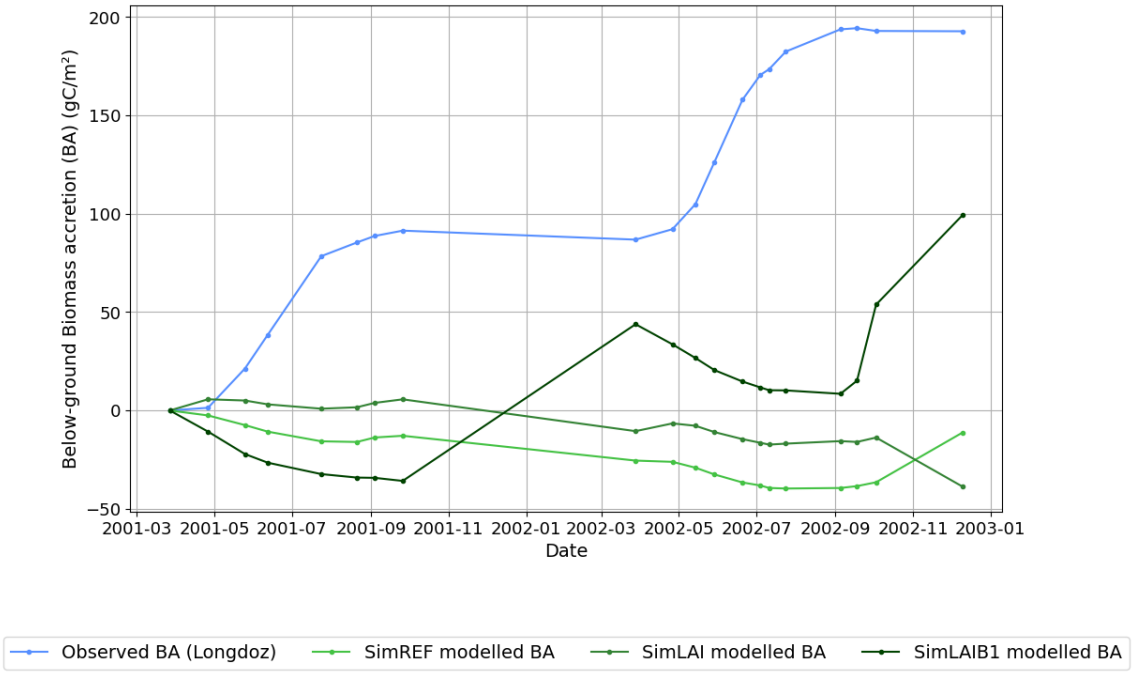

(b) Graphs of the daily accretion of observed and predicted below-ground biomass (gC/m^2) for 2001 and 2002.

Figure 14: Daily accretion of the above-ground and below-ground biomass (gC/m^2) of the observation (provided by Bernard Longdoz) and the three simulations.

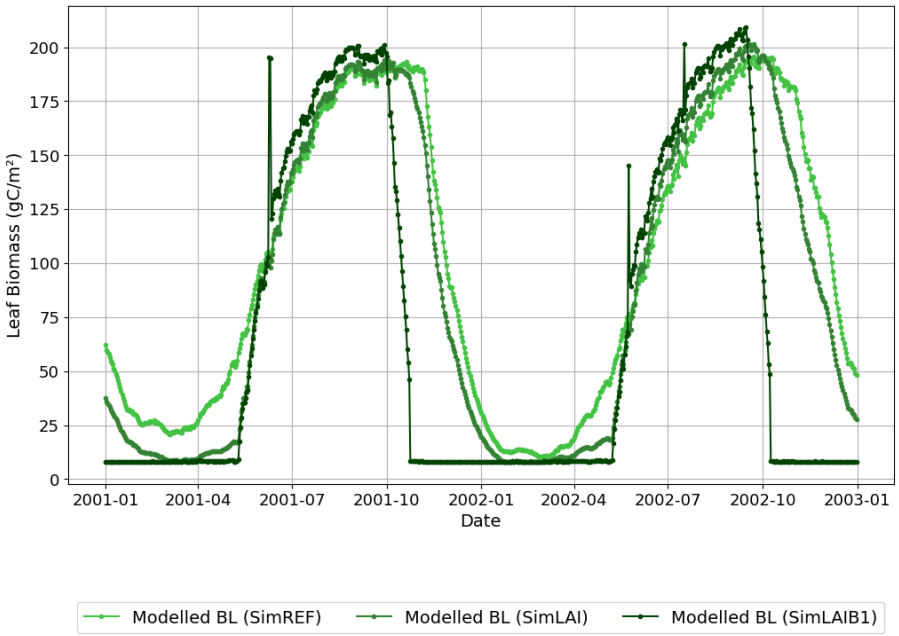

Figure 15: Predicted Leaf Biomass reservoir (gC/m^2) of the three simulations for 2001 and 2002.

3.3 Analysis of the predictions of the 2003 drought

Initiating the analysis of the 2003 drought predictions, a review of the trends exhibited by the monthly average diurnal cycle predictions for the year 2003 from the three distinct simulations, comparing them with the patterns observed in the years 2001 and 2002 (Appendix E). The behaviour of carbon flux and latent heat predictions for 2003 mirrors that of 2001 and 2002 (Tables 5 and 4). Latent heat is consistently overestimated in summer and underestimated in winter. Ecosystem respiration tends to be underestimated in summer and overestimated in winter, with the characteristic drop attributed to budburst and instabilities in the carbon allocation scheme in SimLAIB1. Gross primary production continues to be underestimated throughout the year, with the exception of SimREF's overestimation in November. However, the observations of net ecosystem exchange exhibit different dynamics compared to 2001 and 2002, influenced by drought conditions and potentially noisy flux data. Nevertheless, the overall trend of the simulations aligns with that observed in 2001 and 2002.

Given the similarity in the behaviour of the 2003 monthly average diurnal cycle predictions to those of 2001 and 2002, the subsequent analysis will focus on a comparison of interannual monthly means. This aims to evaluate the model's ability to accurately represent drought conditions across the simulations. Additionally, drought-induced impacts on soil-plant-atmosphere exchanges predominantly manifest as a reduction in latent heat (primarily transpiration) and gross primary production due to stomatal closure to mitigate water loss (Bastos et al. (2020)). Consequently, only the results of these fluxes are presented in Figure 16.

Observations indicate the summer peak in GPP for 2003 is approximately 1 $\mu mol/m^2s$ lower than in previous years, with a shortened timespan. While the magnitude of the simulations does not decrease in line with observations, the timespan reduction follows the observed dynamic decrease. SimLAI-LAIB1 exhibits a closer match to the observed magnitude and trend, supported by rRMSE and NSE metrics suggesting superior model fit compared to SimREF (Table 5). In fact, SimLAIB1 demonstrates the best performance in simulating carbon fluxes and sensible heat, whereas SimREF excels in simulating latent heat. This aligns with the results from the 2001-2002 predictions, except for the added improvement in representing ecosystem respiration by SimLAIB1.

Concerning the Latent Heat flux, the observed peak in 2003 is lower than in 2002 but exceeds that of 2001. Nevertheless, all simulations overestimate summer peaks, and the 2003 predicted summer peak is unexpectedly greater than in the previous years. Analysis of Figure 16c and 16d indicates that this anomaly is attributed to transpiration rather than evaporation, akin to observations in the preceding two years (Section 4.2.3). Transpiration is approximately 20 W/m^2 higher for the three simulations compared to the two previous years.

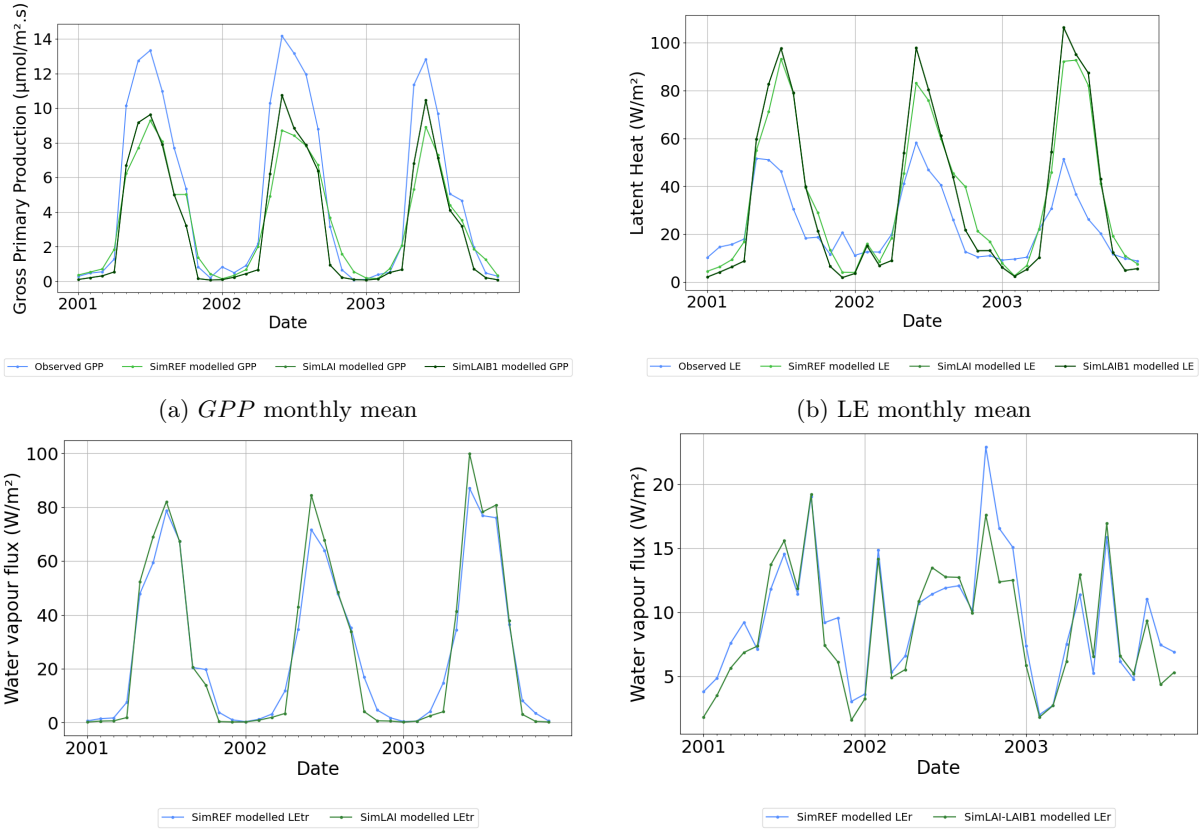

(a) GPP monthly mean

(b) LE monthly mean

(c) Transpiration monthly mean

(d) Evaporation monthly mean

Figure 16: Those graphs display monthly mean, excluding nighttime values. For the Gross Primary Production (µmol/m^{2}s) and the Latent Heat (W/m^2), the simulations and observations are displayed following the same colour scheme as the previous figures. For the transpiration and evaporation flux, only the SimREF (blue line) and SimLAI (green line) predictions are displayed as no observations were available and the output of SimLAI and SimLAIB1 are identical.

Table 5: Relative root mean square error convergence index and Nash-Sutcliff efficiency quality index were computed for each simulation to assess model performance for the year 2003 (drought simulation). These indices were calculated based on the daily mean, excluding nighttime values.

Index	**Simulation**	R_{net}	H	LE	NEE	GPP	R_{eco}
rRMSE	**SimREF**	3,76 $\times 10^{-6}$	1,43 $\times 10^{-5}$	3,28 $\times 10^{-5}$	2,33 $\times 10^{-4}$	9,05 $\times 10^{-5}$	2,38 $\times 10^{-4}$
	SimLAI	3,79 $\times 10^{-6}$	1,42 $\times 10^{-5}$	3,57 $\times 10^{-5}$	2,39 $\times 10^{-4}$	7,97 $\times 10^{-5}$	2,34 $\times 10^{-4}$
	SimLAIB1	3,79 $\times 10^{-6}$	1,42 $\times 10^{-5}$	3,57 $\times 10^{-5}$	2,35 $\times 10^{-4}$	7,97 $\times 10^{-5}$	2,07 $\times 10^{-4}$
NSE	**SimREF**	0,262	0,007	-0,688	0,064	0,644	0,591
	SimLAI	0,258	0,014	-0,995	0,018	0,724	0,601
	SimLAIB1	0,258	0,014	-0,995	0,051	0,724	0,689

4 Discussions

4.1 Spin-up

The computed values for biomass and soil organic carbon (SOC) during the spin-up process are overestimated, compromising the accuracy of subsequent simulations. For instance, these SOC values may lead to an overestimated respiration flux.

Several causes could explain this overestimation. First, in 1996, the trees of the Hesse forest were 30 years old, according to Granier et al. (2008). However, the spin-up simulates biomass accumulation over 255 years, resulting in values representing a 255-year-old forest at equilibrium. This disparity led to values being misaligned with the forest state in 1996. Additionally, using recent atmospheric forcing data, including air carbon concentration, may contribute to inaccuracies owing to elevated atmospheric carbon levels. Using older atmospheric forcing data such as the database Safran would help avoid these inaccuracies leading to overestimating the biomass and SOC. Furthermore, as forest management, including thinning, is not incorporated, the model fails to account for the regular losses of above-ground biomass. Ultimately, the reliance on core samples as input values introduces uncertainty due to inherent biases such as soil heterogeneity and sampling instrument bias.

An enhanced approach addressing these concerns is required to achieve an accurate representation of 1996 conditions. Generally, spin-ups for biomass reservoirs and SOC stocks are conducted separately to align with measured values. When this separation is not feasible, incorporating measured values while respecting SOC ratios from the spin-up output into the PREP file for subsequent simulations would rectify this overestimation. Besides, considering older measurements for atmospheric carbon may provide a more precise representation. Furthermore, adjusting the spin-up time span to 30 years to correspond to the forest age would result in carbon stocks that are more closely representative of the 1996 ecosystem state. Nevertheless, ISBA is a global land surface model, resulting in a lack of modelled processes when trying to simulate a local site ecosystem, such as thinning out.

These suggested improvements were not implemented in this thesis. Consequently, the outcomes of the subsequent simulations must be approached with caution, acknowledging the influence of these overestimated values.

4.2 Outputs of the different simulations

4.2.1 Leaf Area Index

The distinctive simulation behaviour of SimREF, rooted in its reliance on specific leaf area and leaf biomass (Eq. 20), reflects the application of a uniform phenological model across all deciduous broadleaf forests. However, this approach inherently limits its ability to accurately capture the unique dynamics inherent to Beech trees.

Beech trees, characterized by a distinctive phenological pattern, deviate from the general deciduous broadleaf forest dynamics. Unlike their counterparts, Beech trees exhibit a rapid budding process, unfolding within two weeks. Remarkably, the leaves are already well-developed within the bud, achieving photosynthetic activity at an early stage. This specific dynamic poses a challenge for SimREF, which is designed around a uniform phenological framework.

The consequences of this discrepancy extend to the simulation outcomes, particularly influencing carbon fluxes, latent heat (encompassing the evaporation of intercepted rain and transpiration from leaves, as discussed in Section 2.2.1.2), and the sensible heat flux. These turbulent fluxes are intricately

linked to the surface resistance which varies according to LAI (Eqs. 4, 1). The LAI regulates the dark respiration of the leaf which determines the net assimilation of CO_2 (Eq. 7). Given SimREF's inability to accurately represent the Beech-specific dynamics, these critical fluxes are prone to inaccuracies in their simulation.

This limitation underscores the importance of using refined simulation models to capture the dynamics of Beech trees. In the context of this thesis, the SimLAI and SimLAIB1 simulations represent an attempt to address this challenge.

4.2.2 Issues with the carbon allocation scheme

During the replication in Python and understanding the programming of the allocation scheme module, several issues were pointed out which prevented the realisation of the fine-tuning outside the main program of ISBA.

The purpose of extracting the allocation scheme module in Python was to introduce the observed Leaf Area Index (LAI) as an input. This adjustment sought to enhance the representation of Beech phenology, a refinement necessitated by the inability of the simulated LAI to capture the Beech phenology (Section 4.2.1). The simulated LAI tends to conserve leaves during autumn and winter, resulting in an unwilling conservation of leaf biomass. It affected predictions related to latent heat and carbon exchange. The adjustment aimed to rectify this issue by forcing a decline in leaf biomass and facilitating its transfer to other reservoirs.

Unfortunately, the inputs required (Table 6) are sourced from other modules, thereby omitting consideration of the observed LAI as an input. The main problematical input was the daily net CO_2 assimilation, computed within the photosynthesis module. The daily net CO_2 assimilation is used to compute the allocation and respiration term (Eqs. 23 and 15) of the biomass reservoir evolution equation 19. The leaf-level net CO_2 assimilation is computed using the leaf dark respiration which varies along with the simulated LAI (Eq. 7). Moreover, it is extrapolated to the canopy using the simulated LAI (Section 2.2.2.1). This methodological dependence on simulated LAI presents a roadblock, potentially resulting in a stabilisation of the allocation scheme without due consideration of the measured LAI.

Therefore, two simulations (SimLAI and SimLAIB1) were conducted to address those issues. SimLAI focused on obtaining daily net assimilation aligned with the observed LAI. SimLAIB1 is the SimLAI with the addition of the assimilation of observed LAI within the allocation scheme. This enabled the leaf biomass to be linked to the observed LAI values specified, strengthening the model's representation of beech phenology.

Table 6: List of the inputs in the allocation scheme module which are outputs of other modules.

Inputs from other modules	
LAI	Maximum leaf assimilation
Biomass of the previous day	Minimum LAI
Daily cumulated respiration of each biomass reservoir	Daily net CO_2 assimilation
Mesophyll conductance	Turnover from biomass to litter
e-folding time for senescence	New radiative transfer

4.2.3 Turbulent fluxes

In Section 3.2.2, it was pointed out that the predictions of SimLAI and SimLAIB1 are identical, exposing the leaf biomass isn't used for their computation (Section 2.2.1).

Considering the overall overestimation of turbulent fluxes, the accurate representation of net radiation (Section 3.2.1), and the necessity for maintaining energy balance (Eq. 1), collectively imply potential errors in predicting turbulent fluxes or an underestimation of observed fluxes due to the lack of energy closure in FLUXNET records and relative uncertainty around 25% (Santaren et al. (2014)). The limitations in tower measurements hinder a comprehensive assessment of soil conduction, leading to significant losses.

According to Napoly et al. (2017), the sensible heat flux is constantly overestimated in summer for deciduous broadleaf forests. However, in the results of this thesis, the three simulations exhibit overestimation in both summer and winter. Sensible heat emerges as the most inaccurately represented flux, with an NSE below 0.5. Interestingly, introducing observed LAI as input enhances the quality of sensible heat flux representation while exacerbating the quality of latent heat representation. This inverse correlation underscores the impact of maintaining energy balance on turbulent fluxes. With net radiation being consistent across all three simulations (see Section 3.2.1), the total sum of the balance components is identical. Since the ground flux (G) is generally low, an increase in LAI leads to an increase in latent heat flux due to rising evapotranspiration (Eq. 4) and a subsequent decrease in sensible heat flux, thereby reducing overestimation and improving representation.

Despite the decrease in the quality of latent heat flux representation when observed LAI is incorporated, the overall temporal pattern appears more coherent without the excessive values observed in SimREF during winter. The overestimation of SimREF's winter latent heat flux is attributed to erroneous LAI values. The latent heat computation involves three water vapour fluxes (Equation 4), with differences between SimREF and SimLAI-LAIB1 lying in direct evaporation and transpiration from the foliage, as these fluxes are computed based on the LAI. The predominant factor contributing to the difference between SimREF and SimLAI-LAIB1 is the magnitude of transpiration, following the dynamics of LAI and air temperature (Figure 3, 7b and Appendix D Figure 23). During winter, spring, and autumn, except February 2002, SimREF latent heat values exceed those of SimLAI-LAIB1 as it conserves an LAI superior to the observed one. This results in premature SimREF evapotranspiration from the foliage, contributing to the overall overestimation of latent heat. However, in summer, the situation is reversed, with SimLAI-LAIB1 exhibiting a greater LAI.

While the analysis of evapotranspiration elucidates the differences between SimREF and SimLAI-LAIB1, the overall overestimation from the three simulations of latent heat likely stems from an inaccurate assessment of evapotranspiration intensity or, as previously mentioned, the underestimation of latent heat in the observed data due to the lack of energy closure in FLUXNET records and their relative uncertainty (Santaren et al. (2014)). The behaviour of direct evaporation does not align with the dynamics of the leaf area index (LAI), despite the intercepted reservoir exhibiting a corresponding pattern. An intriguing observation arises in February 2002 when evaporation from the intercepted reservoir peaks alongside wind speed and total soil water content, despite the absence of water in this reservoir (Appendix D). This evaporation attributed to the foliage should have originated from soil evaporation. Typically, in winter, when LAI is null, the latent heat flux should be dominated by ground evaporation (Napoly et al. (2017)), yet it is null for the entire period (2001-2002). The latent heat flux is governed by the evaporation from the intercepted reservoir of the foliage, which should be reduced to the minimum required by the model ($LAI_{\min} = 0.3$). Additionally, the evaporation from the intercepted foliage maintains the same magnitude across the entire period (except for January and February 2002). This anomaly indicates a potential issue in the computation of the direct evaporation and soil evaporation, potentially leading to a general overestimation of the latent heat flux.
The rate of water evaporation from any surface is inherently linked to the specific humidity difference between the surface and the surrounding air. A temporal analysis reveals that surface-specific humidity increased early in 2001, decreased during the winter of 2001-2002, and then increased again in the summer, with values ranging from 3.6 g/kg to 10.9 g/kg. While this indicates elevated humidity levels during the summer, it fails to solely account for the observed overestimation.
A further consideration is given to the role of vapour pressure deficit, a parameter conditioning transpiration from plants through the stomatal conductance equation (Medlyn et al., 2011). The vapour pressure deficit is higher in summer, and the latent heat closely follows its dynamic. This suggests that, even though water vapour fluxes are overestimated, their representation in the model remains close to

reality under varying vapour pressure deficit conditions.

An avenue for improving energy flux computation is exploring the ISBA-MEB model, which addresses biases in ISBA (Napoly et al. (2017) and Le Moigne (2018)). Although currently untested with ISBA-CC, investigating the simultaneous use of ISBA-MEB and ISBA-CC could potentially enhance the representation of turbulent fluxes.

4.2.4 Carbon

While the adjustment made in SimLAIB1 does not enhance the prognoses of turbulent fluxes, it could improve the predictions of carbon fluxes due to a more realistic representation of phenology (Section 4.2.3). Indeed, ecosystem respiration is composed of heterotrophic and autotrophic respiration. Autotrophic respiration, especially leaf dark respiration, depends on biomass reservoirs and Leaf Area Index (LAI) (Eqs. 15 - 18 in Section 2.2.2.2). Conversely, heterotrophic respiration is influenced by soil organic carbon (Section 2.2.2.2). The Gross Primary Production (GPP) corresponds to the raw carbon dioxide assimilation (Equation 6). Thus, the adjustment made in SimLAIB1 doesn't affect its performance as it is computed without considering the biomass reservoir. The differences between SimREF and SimLAI-LAIB1 are attributed to the influence of LAI through the $R_{d,leaf}$ term (see Section 4.2.1). Finally, the Gross Primary Production and ecosystem respiration predictions are used to compute the net ecosystem exchange (NEE) following the Equation 6. Therefore, it was expected that NEE trends would closely align with these individual fluxes.

As discussed in Section 4.1, the overestimation of stocks in 1996 leads to an overestimation of heterotrophic respiration, particularly noticeable in winter. During this season, heterotrophic respiration is coupled with autotrophic respiration from active structural biomass, below-ground structural biomass, and above-ground biomass. These autotrophic respirations are computed based on the biomass reservoir content, which is influenced by the LAI input of the allocation scheme subroutine (Section 2.2.2.3). This dependence explains the winter discrepancy between SimLAIB1 and the other two simulations, as SimLAIB1 employs observed LAI as input for the allocation scheme subroutine. In contrast, the other two simulations compute the evolution of their biomass reservoirs based on simulated LAI, resulting in higher values of ecosystem respiration in winter. This discrepancy arises because the allocation scheme conserves biomass for an extended period due to conserving a high LAI late in the season (see Figure 7b). Regarding GPP, the effect of adding the observed LAI as input for the photosynthesis subroutine improved its predictions, while the SimLAIB1 didn't change the performance. Indeed, its computation solely relies on terms depending on the LAI and not on the biomass evolution. Hence, the SimREF simulation overestimates the peaks of April and November 2001, as well as the peaks from October to December 2002, as a consequence of the tardive conservation of LAI in the simulation (4.2.1). From May until the end of the leaf stage, the GPP predictions of SimLAI-LAIB1 exceeded the one of SimREF as the observed LAI is greater than the simulated. Consequently, these winter, fall and spring R_{eco} overestimations by SimREF, SimLAI and SimLAIB1 led to overestimating the positive values of NEE predictions for those periods. This impact was smoothened in April 2001, October and November 2001-2002 and December 2002 as the GPP was overestimated by SimREF.

Furthermore, the influence of observed LAI on SimLAIB1's biomass evolution and dark leaf respiration explains the heavy drops observed in May in the ecosystem respiration and NEE representation, as it coincides with LAI transitioning from LAI_{min} to higher values. The inverse relationship between leaf-dark respiration and LAI contributes to these drops, as leaf-dark respiration decreases with increasing LAI. The leaf dark respiration, in turn, affects net assimilation, and together, they play a crucial role in determining the carbon allocation to the leaf biomass reservoir. It subsequently influences allocations to other reservoirs as it is computed by cascade from the leaf reservoir. As the outliers occurred at nighttime, the GPP was null and they were directly implemented in the NEE predictions. It reflects instabilities in the imperfect use of the carbon allocation scheme which are also observable in the biomass reservoir evolution (Section 4.2.5).

Despite the representation improvement, the SimLAI-LAIB1 GPP predictions underestimate the observed values across the whole period and all three simulations underestimated the GPP and R_{eco} in summer. This may be due to the observed R_{eco} and GPP data not being totally representative of reality. The flux data are deduced from measurements and CO_2 fluxes are noisy with a relative uncertainty of around 25 % on a temperate site. Additionally, the flux partitioning can add up to 10% uncertainty (Desai et al. 2008, cited by Joetzjer (2014)) and the method used wasn't the most performing. Consequently, the summer underestimation of both fluxes results in underestimating the negative values of NEE predictions.

Finally, the original model represents the same phenology for all deciduous broadleaf trees which is not accurate for Beech. The leaf of the Beech is already well-developed in the bud before the bud bursts. As soon as it buds, it photosynthesises directly (photosynthetically active) and matures in 2 weeks. As a result, SimREF has difficulty representing fluxes that are highly dependent on LAI, such as GPP and, thus, the NEE, starting prematurely and progressively (4.2.1). Consequently, to get closer to the true phenology of the Beech, the observed LAI was introduced in SimLAI-LAIB1, which explains their predicted GPP steep increase in May. These adjustments resulted in higher performance for the GPP and NEE representations.

In conclusion, the impact of the lower accuracy and precision of SimLAIB1 in representing ecosystem respiration (R_{eco}) is mitigated by its strong performance in GPP representation, which avoids overestimation and provides a faithful representation of GPP trends despite consistently underestimating all peaks. The outcome is an accurate representation of the NEE dynamic and effectively captures the ecosystem's behaviour despite imprecision.

4.2.5 Biomass reservoirs

The examination of biomass accretion predictions from the simulations sheds light on the intricacies of the carbon allocation scheme and the influence of the Leaf Area Index (LAI) on biomass evolution. In SimLAIB1, the incorporation of observed LAI into the carbon allocation scheme results in a total biomass accretion magnitude aligning with the observations of Granier et al. (2008), despite an initial steeper increase during the growth period (see Figure 13). Moreover, SimLAIB1 demonstrates a leaf biomass dynamic matching the observed LAI from Granier et al. (1999) (see Figure 15). Conversely, SimREF and SimLAI, which utilize simulated LAI in the carbon allocation scheme, exhibit similar dynamics in leaf biomass evolution (see Figure 15). Both simulations retain leaf biomass until winter, with slight differences arising from an adjustment made in SimLAI. Adding observed LAI to the photosynthesis subroutine in SimLAI influences carbon allocation through Equations 7 and 23. Indeed, the leaf biomass allocation is computed based on the output of this subroutine such as the net assimilation and the leaf dark respiration. As the leaf biomass reservoir content subsequently cascades to the other reservoirs in the carbon allocation scheme (Section 2.2.2.3), the absolute values of the above-ground, below-ground and total biomass accretion differ between SimLAI and SimREF, despite having a similar dynamic.

The trends in total biomass accretion can be elucidated by examining the dynamics of above-ground and below-ground biomass. Throughout the growth period, above-ground biomass, particularly the active structural biomass representing new twigs, predominantly contributes to the increase in total biomass. Conversely, the biomass reservoir representing the trunk, bough, and branches decreases during this period and increases in winter in SimLAIB1 predictions, albeit at a smaller range than the new twigs biomass reservoir (ranging from 0 to -200gC/m^2 for the former and 0 to 630gC/m^2 for the latter). The winter increase in SimLAIB1 predictions for the trunk, bough, and branches reservoir, parallel with the decrease in the new twigs reservoir, reflects the maturation of new twigs into branches, transferring carbon into the trunk, bough, and branches reservoir. However, the new twigs reservoir resets to 0 in the winter of 2001, with only approximately 17% transferring to the trunk, bough, and branches reservoir, corresponding to half of the new twigs reservoir storage term in the carbon allocation scheme (see Appendix B). Some modifications could enhance this allocation logic for winter carbon conservation. The influx into the new twigs biomass reservoir solely originates from the decline in leaf biomass.

Consequently, in winter, when all leaves are shed, the new twigs reservoir lacks an influx, leading to a decline.

The slight conservation of total biomass and, thus, carbon content, in winter by SimLAIB1, can be attributed to below-ground biomass. Both below-ground biomass reservoirs increase in winter. It reveals encapsulates the senescence dynamic, where plants utilize final resources in leaves to grow other biomass reservoirs. The model partly transfers the decline of leaves and new twigs to the roots sapwood and fine roots (non-woody) and then to the heartwood roots reservoir. Hence, the decline in new twigs partly transfers to the trunk, bough, and branches biomass reservoir, and the two below-ground biomass reservoirs. The remaining decrease in the new twig and leaf biomass is associated with mortality, transferring to litter and Soil Organic Carbon (SOC) carbon stocks. Mortality surpasses storage, with over 50% transforming into litter and SOC.

Most of these problems could be mitigated by adjusting the residence time in the carbon allocation scheme to align with the phenology of the species, specifically Beech (Eq. 22).

Regarding the abrupt peaks observed in SimLAIB1, these occurrences can be attributed to instabilities arising from the imperfect implementation of the allocation routine. The adjustments made so far require further refinement to ensure efficiency and autonomy in simulating specific phenologies, especially those unique to Beech. Despite these instabilities, the dynamic pattern of biomass accretion in SimLAIB1 demonstrates a close approximation to the observed data. This underscores the imperative need for additional enhancements in the allocation routine.

4.3 Analysis of the predictions of the 2003 drought

SimLAI and SimLAIB1 consistently produce identical outputs for both Gross Primary Production (GPP) and Latent Heat (LE) across all three years. This uniformity is attributed to the fact that the computation of GPP and LE does not rely on the biomass evolution in these simulations (Section 4.2.3 and 4.2.4).

As detailed in Section 1.2, beech trees employ a strategy of avoiding water loss through stomatal closure when facing soil water deficit. Closure of the stomata stops exchanges with the atmosphere and therefore stops photorespiration and transpiration. However, ISBA's sensitivity to solar radiation can lead it to predict high transpiration rates in case of sufficient soil water content. The drought response modelled in ISBA is marked by a reduction in mesophyll conductance which is used to compute the net assimilation and the latent heat (Eqs. 12 and 13). Despite a peak in vapour deficit pressure and a decline in soil water content during the summer (Appendix E), the response to drought in ISBA is considered drought-tolerant for all the deciduous broadleaf trees (Section 2.2.2.1). This explains why the mesophyll conductance decline didn't accurately represent the Beech dynamic of the stomatal conductance in response to drought, resulting in overestimating the GPP and LE flux.

Potential avenue for improvement could be refining the conditioning of drought responses based on species sensitivity to allow better representation of the dynamic of the stomatal conductance in response to drought. Another was implemented in ORCHIDEE by Yao et al. (2022), which consists of incorporating a hydraulic architecture within the vascular system of trees. Such enhancements could establish a more accurate connection between water transfer processes at the soil-plant-atmosphere interface. It also allows the simulation of hydraulic failure, therefore improving water and carbon fluxes' response to severe droughts. Finally, the imposition of phenology through SimLAIB1 mainly improved the representation of transfers between soil-plant-vegetation.

Generally, land surface models often encounter difficulties in accurately representing the dynamics of soil-plant-atmosphere exchanges under drought conditions. The simulated responses of GPP and latent heat frequently deviate in terms of geographical distribution, intensity, and the trends (increasing instead of decreasing) of the response. Addressing these challenges justifies a re-examination of the modelling of

the response to drought in the ISBA, to improve its completeness, versatility and accuracy.

4.4 Model improvement

Several strategies have been proposed to refine the comprehensive representation of soil-plant system transfers with the atmosphere.

Firstly, addressing inaccuracies in the forest state representation after the 1996 spin-up is crucial. A potential solution involves separate spin-ups for soil organic carbon and biomass, spanning a forest-age-representative period or until observed values are reached, accounting for factors like thinning. Incorporating routines to simulate thinning based on forest management plans can enhance both above-ground and below-ground biomass representations. Transferring dead roots to soil organic carbon and litter stocks, governed by species-specific decomposition rates conditioning the residence time, can contribute to a more accurate carbon allocation scheme.

Overall, the SimLAIB1 modifications, which imposed the Beech phenology using the observed LAI, have shown promising results in flux representation. However, further adjustments are needed to rectify instabilities arising from imperfect carbon allocation scheme utilisation. Replacing the imposed Beech phenology with an accurately modelled phenology is crucial for forecasting soil-plant system transfers with the atmosphere. Possible implementations include incorporating knowledge on the date and duration of budburst and senescence to implement an evolution of the leaf life expectancy to represent the conservation of initial carbon and the loss rate depending on the species or PFT. Another solution is to integrate degree days for temperature-dependent budburst or to integrate more representative phenology adjusted depending on the PFT. A physiologically multi-layer process-based model, CASTANEA, was tested and parameterised on the Hesse forest (Dufrêne et al. (2005) and Davi et al. (2005)). Consequently, its Beech phenology representation is enhanced compared to ISBA and can offer insights into improving phenology representation in ISBA (Section 2.5 of Dufrêne et al. (2005)). Also, asymmetric foliage distribution in the crown, highlighted in Le Moigne (2018), needs reconsideration, as foliage significantly influences water vapour fluxes (Equation 4). Additionally, enhancing the phenology description could also improve the drought response according to species by completing the PFT characteristics.

Further improvement could be adjusting resistance and/or conductance parametrisation, impacting flux representations under stress-free and drought conditions. Models like ISBA-MEB, addressing biases in ISBA, could enhance turbulent flux representations (Napoly et al. (2017)). However, its utilisation requires testing with ISBA-CC. For instance, re-parametrising mesophyll conductance based on phenology, climate, and soil conditions could enhance ISBA predictions of drought response. Yao et al. (2022) incorporated a hydraulic architecture within the vascular system of trees to enhance the representation of the connection between water transfer processes at the soil-plant-atmosphere interface.

Addressing the issue of winter carbon conservation in biomass reservoirs could be done in two possible ways. It could be realised by adjusting the time of residence in the carbon allocation scheme to align with species phenology. Another is implementing biomass increment using stand-scale total aboveground biomass, as explored by Thum et al. (2017) with ORCHIDEE-AR5. However, it leads to inconsistencies and thus requires further investigation.

Finally, to either refine SimLAIB1 or explore proposed modifications, data from the FR-Hes site spanning 1997 to the present provides an invaluable resource for evaluating ISBA model predictions for Beech forests.

5 Conclusions

To address this master's thesis aim to adjust ISBA to a deciduous broadleaf forest with peculiar phenology, three simulations were developed. The simulation with reference parametrisation (SimREF) demonstrated limitations in capturing the phenological dynamics of Beech trees. The introduction of SimLAI and SimLAIB1, imposing observed LAI at Hesse, partially addressed this issue. This highlighted the importance of refining the ISBA phenological model to adapt it to different types of phenology, including specific drought response dynamics. SimLAIB1, which incorporated observed LAI into the photosynthesis subroutine and the carbon allocation scheme, showed improvements resulting from an enhanced phenology representation.

However, the phenology will only partly enhance the turbulent fluxes forecasts due to how these are calculated within the ISBA. An additional improvement is required to fully improve their simulations. It could be by exploring the potential linkage between ISBA-MEB and ISBA-CC or adjusting the resistance and/or conductance computations. On the other hand, despite SimLAIB1 enhancing the accuracy of predicted values during average years such as 2001 and 2002 and the representation of 2003 drought for GPP, R_{eco}, and H, it weakened the predictions' performance of the other of the fluxes used for benchmarking. Further improvement is required to address this weakness such as the implementation of hydraulic architecture (Yao et al. (2022)). Another issue was pointed out during the conduction of this thesis: the model doesn't conserve biomass during winter despite the numerical reservoir being present for stability purposes. Consequently, an additional phenological adjustment of the carbon allocation scheme parametrisation such as time of residence in the biomass reservoir could be beneficial.

Moreover, these predictions do not consider the evolutionary potential of trees to adapt to future environmental changes. While it may play a crucial role in trees' adaptation to environmental shifts, it remains poorly understood, as well as the factors that drive it (Bontemps (2012)).

Nevertheless, the outcome of the comparative analysis of the conducted adjustments in this thesis revealed promising results of refining the phenology representation to enhance the predictions of the soil-plant system transfers with the atmosphere. Although it still requires several adaptations, contributing to the ongoing testing and exploration of various improvement areas within the CRNM, these results could enable improved forecasting under climate change.

6 Description of personal contribution

During my master's thesis, I had the opportunity to delve into ecosystem modelling, a field that has fascinated me since my bachelor's in Biological Sciences. This experience provided me with the chance to bridge theoretical concepts with real-world applications, offering insights into the intricacies of representing the dynamic aspects of an ecosystem based on our current understanding.

Working with the ISBA model, alongside a trustworthy and supportive team, further enriched my exploration. Bernard Longdoz, Emilie Joetjzer and Jonathan Bitton shared observed data, information, and guidance, facilitating significant progress in the analysis and adjustment of ISBA. Christine Delire's expert guidance helped me navigate the complexities of ISBA and conducted the adjustment of SimLAI and SimLAIB1, where her extensive knowledge of the model was crucial. Additionally, she provided valuable leads to help me progress in the analysis and adjustment process.

I acknowledge that the outcomes of this thesis would not have reached the level of importance they hold without the collaborative efforts of this remarkable team. Their mentorship not only expanded my knowledge but also challenged me to surpass my perceived limits. My contributions involved data processing and analysis, the replication of the carbon allocation scheme in Python and the creation of its corresponding flow chart. The scope of data processing and analysis encompassed coding in Python all the scripts used to analyse and display the model outputs and observations, as well as the indexes, followed by the interpretation and discussion of results to provide insights and valuable directions for prospective research endeavours.

This experience also underscored the intricate nature of adjusting a complex land surface model such as ISBA, revealing that the process is far from straightforward and demands dedicated time and effort. The collective efforts of the team and the lessons learned have been instrumental in shaping my understanding and skills in ecosystem modelling, laying a foundation for future attempts in this field.

References

Chapter 15 - Estimate of vegetation production of terrestrial ecosystem. In S. Liang and J. Wang, editors, *Advanced Remote Sensing (Second Edition)*, pages 581–620. Academic Press, second edition edition, 2020. ISBN 978-0-12-815826-5. doi: https://doi.org/10.1016/B978-0-12-815826-5.00015-5. URL https://www.sciencedirect.com/science/article/pii/B9780128158265000155.

M. Aubinet, T. Vesala, and D. Papale, editors. *Eddy Covariance: A Practical Guide to Measurement and Data Analysis*. Springer Netherlands, Dordrecht, 2012. ISBN 978-94-007-2350-4 978-94-007-2351-1. doi: 10.1007/978-94-007-2351-1. URL https://link.springer.com/10.1007/978-94-007-2351-1.

D. Baize, M. Girard, A. G. Beaudou, and R. Poss. *Référentiel pédologique 2008*. Savoir Faire. Quae, Versailles, 2009. ISBN 978-2-7592-0185-3. URL https://www.documentation.ird.fr/hor/fdi:010063397.

A. Bastos, Z. Fu, P. Ciais, P. Friedlingstein, S. Sitch, J. Pongratz, U. Weber, M. Reichstein, P. Anthoni, A. Arneth, V. Haverd, A. Jain, E. Joetzjer, J. Knauer, S. Lienert, T. Loughran, P. C. McGuire, W. Obermeier, R. S. Padrón, H. Shi, H. Tian, N. Viovy, and S. Zaehle. Impacts of extreme summers on european ecosystems: a comparative analysis of 2003, 2010 and 2018. *Philosophical Transactions of the Royal Society B*, 375(1810):20190507, 2020. doi: 10.1098/rstb.2019.0507. URL https://doi.org/10.1098/rstb.2019.0507. Published on 7 September 2020.

A. Bolte, L. Hilbrig, B. Grundmann, F. Kampf, J. Brunet, and A. Roloff. Climate change impacts on stand structure and competitive interactions in a southern swedish spruce-beech forest. *European Journal of Forest Research*, 129(3):261–276, 2010. doi: 10.1007/s10342-009-0323-1. URL https://www.scopus.com/inward/record.uri?eid=2-s2.0-77952319467&doi=10.1007%2fs10342-009-0323-1&partnerID=40&md5=abe781d97b196bacc1a8f4835f2184ef.

A. Bontemps. *Potentiel évolutif d'une population de hêtre commun sur le Mont Ventoux*. PhD thesis, 09 2012.

N. Bréda, A. Granier, and G. Aussenac. La Sécheresse de 2003 dans le contexte climatique des 54 dernières années : analyse écophysiologique et influence sur les arbres forestiers. *Revue forestière française*, 56(2):109–131, 2004. doi: 10.4267/2042/5081. URL https://hal.science/hal-03449335.

R. J. W. Brienen, L. Caldwell, L. Duchesne, and et al. Forest carbon sink neutralized by pervasive growth-lifespan trade-offs. *Nature Communications*, 11:4241, 2020. doi: 10.1038/s41467-020-17966-z. URL https://doi.org/10.1038/s41467-020-17966-z.

C. Brück-Dyckhoff, R. Petercord, and R. Schopf. Vitality loss of european beech (*fagus sylvatica* l.) and infestation by the european beech splendour beetle (*agrilus viridis* l., buprestidae, coleoptera). *Forest Ecology and Management*, 432:150–156, 2019. doi: 10.1016/j.foreco.2018.09.001. URL https://www.scopus.com/inward/record.uri?eid=2-s2.0-85053440853&doi=10.1016%2fj.foreco.2018.09.001&partnerID=40&md5=9dc6e0040e6e067a4eb5127769cc9b01.

J.-C. Calvet and J.-F. Soussana. Modelling co2-enrichment effects using an interactive vegetation svat scheme. *Agricultural and Forest Meteorology*, 108(2):129–152, June 2001.

J. C. Calvet, V. Rivalland, C. Picon-Cochard, and J. M. Guehl. Modelling forest transpiration and co2 fluxes - response to soil moisture stress. *Agricultural and Forest Meteorology*, 124(3-4):143–156, August 2004.

J. C. Calvet, A. L. Gibelin, J. L. Roujean, E. Martin, P. Le Moigne, H. Douville, and J. Noilhan. Past and future scenarios of the effect of carbon dioxide on plant growth and transpiration for three vegetation types of southwestern france. *Atmospheric Chemistry and Physics*, 8(2):397–406, 2008.

D. Carrer, J.-L. Roujean, S. Lafont, J.-C. Calvet, A. Boone, B. Decharme, C. Delire, and J.-P. Gastellu-Etchegorry. A canopy radiative transfer scheme with explicit fapar for the interactive vegetation model isba-a-gs: Impact on carbon fluxes. *Journal of Geophysical Research*, 188:888–903, 2013.

E. Chaste, N. Bréda, V. Badeau, J. Levillain, A. Benard, and I. Nathalie Leroy (UMR Silva: Université de Lorraine, AgroParisTech. Indicateurs de gestion durable. https://foret.ign.fr/IGD/fr/, 2023. Accessed on 01/12/2023.

X. Chen, M. Luo, and M. Larjavaara. Effects of climate and plant functional types on forest above-ground biomass accumulation. *Carbon Balance and Management*, 18(1), 2023. doi: 10.1186/s13021-023-00225-1. URL https://www.scopus.com/inward/record.uri?eid=2-s2.0-85150866798&doi=10.1186%2fs13021-023-00225-1&partnerID=40&md5=47e1022aae04c0f0417d96ba542e868c. Cited by: 1; All Open Access, Gold Open Access, Green Open Access.

Y. Chen, J. Ryder, V. Bastrikov, M. J. McGrath, K. Naudts, J. Otto, C. Ottlé, P. Peylin, J. Polcher, A. Valade, A. Black, J. A. Elbers, E. Moors, T. Foken, E. Van Gorsel, V. Haverd, B. Heinesch, F. Tiedemann, A. Knohl, S. Launiainen, D. Loustau, J. Ogeé, T. Vessala, and S. Luyssaert. Evaluating the performance of land surface model orchidee-can v1.0 on water and energy flux estimation with a single-and multi-layer energy budget scheme. 2016.

CNRM. Centre national de recherches météorologiques. https://www.umr-cnrm.fr, 2023.

H. Davi, E. Dufrêne, A. Granier, V. Le Dantec, C. Barbaroux, C. François, and N. Bréda. Modelling carbon and water cycles in a beech forest. part ii.: Validation of the main processes from organ to stand scale. *Ecological Modelling*, 185(2-4):387 – 405, 2005. doi: 10.1016/j.ecolmodel.2005.01.003. URL https://www.scopus.com/inward/record.uri?eid=2-s2.0-17644380981&doi=10.1016%2fj.ecolmodel.2005.01.003&partnerID=40&md5=35ea9d608d94e3da15c6f0ab2f588384.

C. Delire, R. Séférian, B. Decharme, R. Alkama, J.-C. Calvet, D. Carrer, A.-L. Gibelin, E. Joetzjer, X. Morel, M. Rocher, and D. Tzanos. The Global Land Carbon Cycle Simulated With ISBA-CTRIP: Improvements Over the Last Decade. *Journal of Advances in Modeling Earth Systems*, 12(9):e2019MS001886, Sept. 2020. ISSN 1942-2466. doi: 10.1029/2019MS001886. URL https://doi.org/10.1029/2019MS001886. Publisher: John Wiley & Sons, Ltd.

N. Dolar, E. M. d. Castillo, R. Serrano-Notivoli, M. d. L. Arrillaga, K. Novak, M. Merela, and K. Čufar. Spatial and temporal variation of *fagus sylvatica* growth in marginal areas under progressive climate change. *Dendrochronologia*, 81:126135, 2023. doi: 10.1016/j.dendro.2023.126135. URL https://www.scopus.com/inward/record.uri?eid=2-s2.0-85172934206&doi=10.1016%2fj.dendro.2023.126135&partnerID=40&md5=dd214dc006783c06f44c1c0ae3e41391.

E. Dufrêne, H. Davi, C. François, G. Le Maire, V. Le Dantec, and A. Granier. Modelling carbon and water cycles in a beech forest. part i: Model description and uncertainty analysis on modelled nee. *Ecological Modelling*, 185(2-4):407 – 436, 2005. doi: 10.1016/j.ecolmodel.2005.01.004. URL https://www.scopus.com/inward/record.uri?eid=2-s2.0-17644374804&doi=10.1016%2fj.ecolmodel.2005.01.004&partnerID=40&md5=c84e31eb7fc2acb463962d9e149e87df.

M. E. Dusenge, A. G. Duarte, and D. A. Way. Plant carbon metabolism and climate change: elevated co2 and temperature impacts on photosynthesis, photorespiration and respiration. *New Phytologist*, 221 (1):32–49, 2019. doi: https://doi.org/10.1111/nph.15283. URL https://nph.onlinelibrary.wiley.com/doi/abs/10.1111/nph.15283.

European Environment Agency. Carbon stocks and sequestration in terrestrial and marine ecosystems: a lever for nature restoration? Briefing 05, European Environment Agency, 2022. URL https://doi.org/10.2800/742383.

G. D. Farquhar and T. D. Sharkey. Stomatal conductance and photosynthesis. *Annual Review of Plant Physiology*, 33(1):317–345, 1982. doi: 10.1146/annurev.pp.33.060182.001533. URL https://doi.org/10.1146/annurev.pp.33.060182.001533.

L. Fernández-de Uña, J. Martínez-Vilalta, R. Poyatos, M. Mencuccini, and N. G. McDowell. The role of height-driven constraints and compensations on tree vulnerability to drought. *New Phytologist*, 2023. doi: 10.1111/nph.19130. First published on 23 July 2023.

E. Frei, M. Gossner, Y. Vitasse, V. Queloz, V. Dubach, A. Gessler, C. Ginzler, F. Hagedorn, K. Meusburger, M. Moor, E. Samblás Vives, A. Rigling, I. Uitentuis, G. von Arx, and T. Wohlgemuth. European beech dieback after premature leaf senescence during the 2018 drought in northern switzerland. *Plant Biology*, 24(7):1132–1145, 2022. doi: 10.1111/plb.13467. URL https://www.scopus.com/inward/record.uri?eid=2-s2.0-85136124331&doi=10.1111%2fplb.13467&partnerID=40&md5=ac071f1d76b9399cc8daa33d92a0ef86.

T. Gaudin. Réchauffement climatique, sécheresses et migrations. *Annales des Mines - Responsabilité et environnement*, 80(4):29–36, 2015. doi: 10.3917/re1.080.0029. URL https://www.cairn.info/revue-responsabilite-et-environnement-2015-4-page-29.htm.

A.-L. Gibelin, J.-C. Calvet, and N. Viovy. Modelling energy and co2 fluxes with an interactive vegetation land surface model-evaluation at high and middle latitudes. *Agricultural and forest meteorology*, 148 (10):1611–1628, 2008. ISSN 0168-1923.

M. M. Gossner, K. Falck, and W. W. Weisser. Effects of management on ambrosia beetles and their antagonists in european beech forests. *Forest Ecology and Management*, 437:126–133, 2019. doi: 10.1016/j.foreco.2019.01.034. URL https://www.scopus.com/inward/record.uri?eid=2-s2.0-85060703676&doi=10.1016%2fj.foreco.2019.01.034&partnerID=40&md5=42a2381a3b1f6b1e24035a1b950632a2.

J. Goudriaan, H. van Laar, H. van Keulen, and W. Louwerse. Photosynthesis, co2 and plant production. In *Series A*, pages 107–122. Plenum Press, New York, 1985.

A. Granier, N. Bréda, P. Biron, and S. Villette. A lumped water balance model to evaluate duration and intensity of drought constraints in forest stands. *Ecological Modelling*, 116(2–3):269–283, 1999. ISSN 0304-3800. doi: 10.1016/S0304-3800(98)00205-1. URL https://doi.org/10.1016/S0304-3800(98)00205-1.

A. Granier, P. Biron, and D. Lemoine. Water balance, transpiration and canopy conductance in two beech stands. *Agricultural and Forest Meteorology*, 100(4):291–308, 2000. ISSN 0168-1923. doi: 10.1016/S0168-1923(99)00151-3. URL https://doi.org/10.1016/S0168-1923(99)00151-3.

A. Granier, N. Bréda, B. Longdoz, P. Gross, and J. Ngao. Ten years of fluxes and stand growth in a young beech forest at Hesse, North-eastern France. *Ann. For. Sci.*, 65(7):704–704, Jan. 2008. ISSN 1286-4560, 1297-966X. doi: 10.1051/forest:2008052. URL https://annforsci.biomedcentral.com/articles/10.1051/forest:2008052.

T. Gregorčič, A. Rozman, and B. Repe. Predicting the potential ecological niche distribution of slovenian forests under climate change using maxent modelling [ocena možnih vplivov podnebnih sprememb na prostorsko razporeditev ekoloških niš slovenskih gozdov z uporabo metode maksimalne entropije]. *Acta Geographica Slovenica*, 63(1):89–109, 2023. doi: 10.3986/AGS.11561. URL https://www.scopus.com/inward/record.uri?eid=2-s2.0-85175255000&doi=10.3986%2fAGS.11561&partnerID=40&md5=824e11440968263ccf30170955b3cfc7.

S. Huet, F. Forgeard, and C. Nys. Above- and belowground distribution of dry matter and carbon biomass of atlantic beech (fagus sylvatica l.) in a time sequence. *http://dx.doi.org/10.1051/forest:2004063*, 61, 10 2004. doi: 10.1051/forest:2004063.

ICOS. Integrated carbon observation system : Hesse station. https://meta.icos-cp.eu/resources/stations/ES_FR-Hes, 2023a.

ICOS. Integrated carbon observation system in a nutshell. https://www.icos-cp.eu/about/icos-in-nutshell, 2023b.

Intergovernmental Panel on Climate Change. Climate Change 2023: Synthesis Report. A Report of the Intergovernmental Panel on Climate Change. Contribution of Working Groups I, II and III to the Sixth Assessment Report of the Intergovernmental Panel on Climate Change. IPCC, Geneva, Switzerland (in press), 2023.

Inventaire Forestier National. L'inventaire forestier : No. 07 - carbone. Available at: https://inventaire-forestier.ign.fr/IMG/pdf/L_IF_no07_carbone.pdf, 2005. Accessed on: 07/06/2023.

F. Jean, H. Davi, S. Oddou-Muratorio, B. Fady, I. Scotti, C. Scotti-Saintagne, J. Ruffault, V. Journe, P. Clastre, O. Marloie, W. Brunetto, M. Correard, O. Gilg, M. Pringarbe, F. Rei, J. Thevenet, N. Turion, and C. Pichot. A 14-year series of leaf phenological data collected for european beech (fagus sylvatica l.) and silver fir (abies alba mill.) from their geographic range margins in south-eastern france. *Annals of Forest Science*, 80(1), 2023. doi: 10.1186/s13595-023-01193-9. URL https://www.scopus.com/inward/record.uri?eid=2-s2.0-85171352206&doi=10.1186%2fs13595-023-01193-9&partnerID=40&md5=6def84be7ee27cb2846ca18685c54a4a. Cited by: 0; All Open Access, Gold Open Access.

E. Joetzjer. *Causes, impacts et projections des sécheresses en Amazonie : une étude numérique des processus et des incertitudes*. PhD thesis, Université de Toulouse, Institut National Polytechnique de Toulouse (INP Toulouse), Toulouse, France, December 2014. Thèse en vue de l'obtention du doctorat.

G. Krinner, N. Viovy, N. de Noblet-Ducoudré, J. Ogée, J. Polcher, P. Friedlingstein, P. Ciais, S. Sitch, and I. C. Prentice. A dynamic global vegetation model for studies of the coupled atmosphere-biosphere system. *Global Biogeochemical Cycles*, 19(1):1015–, February 2005.

S. Lafont, D. Loustau, T. Tallec, D. Bonal, E. Ceschia, A. Chabbi, S. Conil, E. Dufrêne, S. Garrigues, R. Huc, R. Joffre, K. Klumpp, L. Bernard, B. Loubet, and B. Mary. The french icos ecosystem monitoring sites: an overview. 09 2014.

G. Landmann, J.-L. Dupouey, V. Badeau, Y. Lefevre, N. Bréda, L.-M. Nageleisen, I. Chuine, and F. Lebourgeois. Le hêtre face aux changements climatiques. *Rendez-vous Techniques de l'ONF*, pages 29–38, 2007.

G. Landmann, J.-L. Dupouey, B. L, Y. Lefevre, B. Nathalie, L.-M. Nageleisen, I. Chuine, and F. Lebourgeois. Le hêtre face aux changements climatiques. ii. connaître les points faibles du hêtre pour les surmonter ? *Forêt-Entreprise*, 182:30–34, 01 2008.

G. J. Langer and J. Bußkamp. Vitality loss of beech: A serious threat to *Fagus sylvatica* in germany in the context of global warming. *Journal of Plant Diseases and Protection*, 130(5): 1101–1115, 2023. doi: 10.1007/s41348-023-00743-7. URL https://www.scopus.com/inward/record.uri?eid=2-s2.0-85152775529&doi=10.1007%2fs41348-023-00743-7&partnerID=40&md5=24c46e347ebbff07024587d236c4980b.

P. Le Moigne. *SURFEX SCIENTIFIC DOCUMENTATION*. 2018. URL https://www.umr-cnrm.fr/surfex/IMG/pdf/surfex_scidoc_v8.1.pdf.

F. Lebourgeois, A. Granier, and N. Bréda. An analysis of regional climate change in france between 1956 and 1997; [une analyse des changements climatiques régionaux en france entre 1956 et 1997. réflexions en terme de conséquences pour les écosystèmes forestiers]. *Annals of Forest Science*, 58(7):733 – 754, 2001. doi: 10.1051/forest:2001160. URL https://www.scopus.com/inward/record.uri?eid=2-s2.0-4244021251&doi=10.1051%2fforest%3a2001160&partnerID=40&md5=41b63897702f9bf61ea4b84a36f80d3a. Cited by: 21; All Open Access, Bronze Open Access, Green Open Access.

G. Lemaire and F. Gastal. *N uptake and distribution in plant canopies*. Springer, Berlin, 1997.

Li-Cor Inc. 2000_manual.pdf | Powered by Box, 1992. URL https://licor.app.boxenterprise.net/s/q6hrj6s79psn7o8z2b2s.

P. Marchelli, E. Thomas, M. Azpilicueta, M. van Zonneveld, and L. Gallo. Integrating genetics and suitability modelling to bolster climate change adaptation planning in patagonian nothofagus forests. *Tree Genetics and Genomes*, 13(6):119, 2017. doi: 10.1007/s11295-017-1201-5. URL https://www.scopus.com/inward/record.uri?eid=2-s2.0-85032334276&doi=10.1007%2fs11295-017-1201-5&partnerID=40&md5=9f6f7675b6422a032eb6f6128f0cb8be.

P. Mascart, J. Noilhan, and H. Giordani. A modified parameterization of flux-profile relationships in the surface layer using different roughness length values for heat and momentum. *Boundary-Layer Meteorology*, 72:331–344, 1995.

V. Masson, J.-L. Champeaux, F. Chauvin, C. Meriguet, and R. Lacaze. A global database of land surface parameters at 1-km resolution in meteorological and climate models. *J. Clim.*, 16(9):1261–1282, 2003.

B. Montigny. Travail de fin d'étude : Etude pluriannuelle de l'allocation du carbon assimilé par deux écosystèmes forestiers et de l'influence de la variabilité climatique sur les sites icos de hesse (france) et de vielsam (belgique), 2021-2022.

Météo France. Le climate en france métropolitaine. `https://meteofrance.com/comprendre-climat/france/le-climat-en-france-metropolitaine`, 2023.

A. Napoly, A. Boone, P. Samuelsson, S. Gollvik, E. Martin, R. Seferian, D. Carrer, B. Decharme, and L. Jarlan. The interactions between soil-biosphere-atmosphere (isba) land surface model multi-energy balance (meb) option in surfexv8 - part 2: Introduction of a litter formulation and model evaluation for local-scale forest sites. *Geoscientific Model Development*, 10(4):1621–1644, 2017. doi: 10.5194/gmd-10-1621-2017.

NASA. Global warming vs climate change. Available at: `https://climate.nasa.gov/global-warming-vs-climate-change/`, 2023. Accessed on: 07/06/2023.

J. Noilhan and S. Planton. A simple parameterization of land surface processes for meteorological models. *Monthly Weather Review*, 117(3):536 – 549, 1989. doi: https://doi.org/10.1175/1520-0493(1989)117<0536:ASPOLS>2.0.CO;2. URL `https://journals.ametsoc.org/view/journals/mwre/117/3/1520-0493_1989_117_0536_aspols_2_0_co_2.xml`.

N. Obladen, P. Dechering, G. Skiadaresis, W. Tegel, J. Keßler, S. Höllerl, S. Kaps, M. Hertel, C. Dulamsuren, T. Seifert, M. Hirsch, and A. Seim. Tree mortality of european beech and norway spruce induced by 2018-2019 hot droughts in central germany. *Agricultural and Forest Meteorology*, 307:art. no. 108482, 2021. doi: 10.1016/j.agrformet.2021.108482. URL `https://www.scopus.com/inward/record.uri?eid=2-s2.0-85107152102&doi=10.1016%2fj.agrformet.2021.108482&partnerID=40&md5=d2253e0870a72dc0337d1a9e6825e752`.

W. J. Parton, D. S. Schimel, C. V. Cole, and D. S. Ojima. Analysis of factors controlling soil organic matter levels in great plains grasslands. *Soil Sci. Soc. Am. J.*, 51:1173–1179, 1987.

W. J. Parton, J. W. B. Stewart, and C. V. Cole. Dynamics of c, n, p, and s in grassland soils: a model. *Biogeochemistry*, 5:109–131, 1988.

P. E. Pinto and J.-C. Gégout. Assessing the nutritional and climatic response of temperate tree species in the vosges mountains. *Annals of Forest Science*, 62(7):761 – 770, 2005. doi: 10.1051/forest:2005068. URL `https://www.scopus.com/inward/record.uri?eid=2-s2.0-28444452999&doi=10.1051%2fforest%3a2005068&partnerID=40&md5=758ad13f5fe6ec466497e5ff75e80d97`. Cited by: 39; All Open Access, Bronze Open Access, Green Open Access.

J. Polcher, B. McAvaney, P. Viterbo, M. A. Gaertner, A. Hahmann, J. F. Mahfouf, J. Noilhan, T. Phillips, A. Pitman, C. A. Schlosser, J. P. Schulz, B. Timbal, D. Verseghy, and Y. Xue. A proposal for a general interface between land surface schemes and general circulation models. *Glob. and Planet. Change*, 19(1-4):261–276, December 1998.

M. Prigoliti, M. T. Chiofalo, F. Petruzzellis, M. A. Lo Gullo, and P. Trifilò. Ecophysiological behavior of *fagus sylvatica* l. growing at its southern distribution limit: Insights for understanding the fate of the european beech under warmer and dryer growth conditions. *Forests*, 14(10):2058, 2023. doi: 10.3390/f14102058. URL `https://www.scopus.com/inward/record.uri?eid=2-s2.0-85175097254&doi=10.3390%2ff14102058&partnerID=40&md5=15125ae41ff5b7ae00fb8ecdfc1122f7`.

S. Rukh, W. Poschenrieder, M. Heym, and H. Pretzsch. Drought resistance of norway spruce (picea abies [l.] karst) and european beech (fagus sylvatica [l.]) in mixed vs. monospecific stands and on dry vs. wet sites. from evidence at the tree level to relevance at the stand level. *Forests*, 11(6):639, 2020. doi: 10.3390/F11060639. URL https://www.scopus.com/inward/record.uri?eid=2-s2.0-85087510254&doi=10.3390%2fF11060639&partnerID=40&md5=66e3ad95cb7358e2c820e6969b0cc2e9.

D. Santaren, P. Peylin, C. Bacour, P. Ciais, and B. Longdoz. Ecosystem model optimization using in situ flux observations: Benefit of monte carlo versus variational schemes and analyses of the year-to-year model performances. *Biogeosciences*, 11(24):7137–7158, 2014. doi: 10.5194/bg-11-7137-2014. URL https://www.scopus.com/inward/record.uri?eid=2-s2.0-84918561737&doi=10.5194%2fbg-11-7137-2014&partnerID=40&md5=9cb5e6e19ea17a2b7a9e254ef64a07f8.

M. Schrumpf, E. Schulze, K. Kaiser, and J. Schumacher. How accurately can soil organic carbon stocks and stock changes be quantified by soil inventories? *Biogeosciences*, 8:1193–1212, 01 2011. doi: 10.5194/bg-8-1193-2011.

P. Schutt, W. Koch, H. Blaschke, K. Lang, J. Schuck, and H. Summer. *Avant que Forêt ne meure*. Delachaux et Niestlé ; Y. Peret Eds, Paris, 1984.

P. J. Sellers, M. D. Heiser, and F. G. Hall. Relations between surface conductance and spectral vegetation indices at intermediate (100 m^2 to 15 km^2) length scales. *J. Geophys. Res.*, 97:19033–19059, 1992.

A. Simon, K. Katzensteiner, and G. Wallentin. The integration of hierarchical levels of scale in tree species distribution models of silver fir (*abies alba* mill.) and european beech (*fagus sylvatica* l.) in mountain forests. *Ecological Modelling*, 485:110499, 2023. doi: 10.1016/j.ecolmodel.2023.110499. URL https://www.scopus.com/inward/record.uri?eid=2-s2.0-85170267257&doi=10.1016%2fj.ecolmodel.2023.110499&partnerID=40&md5=317ccbb09fe65d4f7e6955caf37cd3b1.

T. H. Skaggs, R. G. Anderson, J. G. Alfieri, T. M. Scanlon, and W. P. Kustas. Fluxpart: Open source software for partitioning carbon dioxide and water vapor fluxes. *Agricultural and Forest Meteorology*, 253–254:218–224, 2018. doi: 10.1016/j.agrformet.2018.02.019.

J. Socha, P. Hawryło, L. Tymińska-Czabańska, B. Reineking, M. Lindner, P. Netzel, E. Grabska-Szwagrzyk, R. Vallejos, and C. P. Reyer. Higher site productivity and stand age enhance forest susceptibility to drought-induced mortality. *Agricultural and Forest Meteorology*, 341, 2023. doi: 10.1016/j.agrformet.2023.109680. URL https://www.scopus.com/inward/record.uri?eid=2-s2.0-85168853227&doi=10.1016%2fj.agrformet.2023.109680&partnerID=40&md5=19602b6b919a27172cf725b15f376209. Cited by: 0; All Open Access, Hybrid Gold Open Access.

SPF Santé publique, sécurité de la chaîne alimentaire et environnement. Climat.be. https://climat.be/en-belgique/climat-et-emissions/emissions-des-gaz-a-effet-de-serre/emissions-par-gaz, 2023.

D. B. Stojanović, A. Kržič, B. Matović, S. Orlović, A. Duputie, V. Djurdjević, Z. Galić, and S. Stojnić. Prediction of the european beech (*Fagus sylvatica* l.) xeric limit using a regional climate model: An example from southeast europe. *Agricultural and Forest Meteorology*, 176:94–103, 2013. doi: 10.1016/j.agrformet.2013.03.009. URL https://www.scopus.com/inward/record.uri?eid=2-s2.0-84877333816&doi=10.1016%2fj.agrformet.2013.03.009&partnerID=40&md5=fee16c5946c0d2c047e8e6f746bde7f7.

D. Thom. Natural disturbances as drivers of tipping points in forest ecosystems under climate change - implications for adaptive management. *Forestry*, 96(3):305–315, 2023. doi: 10.1093/forestry/cpad011. URL https://www.scopus.com/inward/record.uri?eid=2-s2.0-85160026456&doi=10.1093%2fforestry%2fcpad011&partnerID=40&md5=54975e6cb975405cb08f5adcfd41c3a9.

T. Thum, N. MacBean, P. Peylin, C. Bacour, D. Santaren, B. Longdoz, D. Loustau, and P. Ciais. The potential benefit of using forest biomass data in addition to carbon and water flux measurements to constrain ecosystem model parameters: Case studies at two temperate forest sites. *Agricultural and Forest Meteorology*, 234-235:48 – 65, 2017. doi: 10.1016/j.agrformet.2016.12.004. URL https://www.scopus.com/inward/record.uri?eid=2-s2.0-85007273828&doi=10.1016%2fj.agrformet.2016.12.004&partnerID=40&md5=323be13315b7f0a1f38cf9d68a4c1414.

A. T. Trugman, L. D. L. Anderegg, W. R. L. Anderegg, A. J. Das, and N. L. Stephenson. Why is tree drought mortality so hard to predict? *Trends in Ecology & Evolution*, 36(6):520–532, 2021. ISSN 0169-5347. doi: 10.1016/j.tree.2021.02.001. URL https://www.sciencedirect.com/science/article/pii/S0169534721000355.

J. Urban, M. Ingwers, M. A. McGuire, and R. O. Teskey. Stomatal conductance increases with rising temperature. *Plant Signal Behav*, 12(8):e1356534, 2017. doi: 10.1080/15592324.2017.1356534.

E. Weng, C. E. Farrior, R. Dybzinski, and S. W. Pacala. Predicting vegetation type through physiological and environmental interactions with leaf traits: evergreen and deciduous forests in an earth system modeling framework. *Global Change Biology*, 23(6):2482–2498, 2017. doi: 10.1111/gcb.13529.

WSL (Institut fédéral de recherches sur la forêt, la neige et le paysage). Changement climatique : combien de sécheresse le hêtre peut-il supporter ? Available at: https://www.wsl.ch/fr/2020/08/changement-climatique-combien-de-secheresse-le-hetre-peut-il-supporternbsp.html, 2020. Accessed on: 07/06/2023.

T. Wutzler, A. Lucas-Moffat, M. Migliavacca, J. Knauer, K. Sickel, L. Šigut, O. Menzer, and M. Reichstein. Basic and extensible post-processing of eddy covariance flux data with reddyproc. *Biogeosciences*, 15:5015–5030, 2018. doi: 10.5194/bg-15-5015-2018. URL https://doi.org/10.5194/bg-15-5015-2018.

Y. Yao, E. Joetzjer, P. Ciais, N. Viovy, F. Cresto Aleina, J. Chave, L. Sack, M. Bartlett, P. Meir, R. Fisher, and S. Luyssaert. Forest fluxes and mortality response to drought: model description (orchidee-can-nha r7236) and evaluation at the caxiuanã drought experiment. *Geoscientific Model Development*, 15:7809–7833, 2022. doi: 10.5194/gmd-15-7809-2022. URL https://doi.org/10.5194/gmd-15-7809-2022.

J. Zell, B. Rohner, E. Thürig, and G. Stadelmann. Modeling ingrowth for empirical forest prediction systems. *Forest Ecology and Management*, 433:771–779, 2019. doi: 10.1016/j.foreco.2018.11.052. URL https://www.scopus.com/inward/record.uri?eid=2-s2.0-85057999568&doi=10.1016%2fj.foreco.2018.11.052&partnerID=40&md5=c7f0d3fffc6d07c507f754feec5ba62b.

V. B. D. échelon central), L.-M. N. D. antenne spécialisée Champenoux), and J.-P. R. (IFN). Bilan de la santé des forêts en 2003 : Les conséquences de la canicule et de la sécheresse sur la santé des forêts. Technical report, Département de la santé des forêts, December 2004.

A Temporal evolution of total dry matter from Montigny (2021-2022) using the allometric relation of Ottorini, 2012

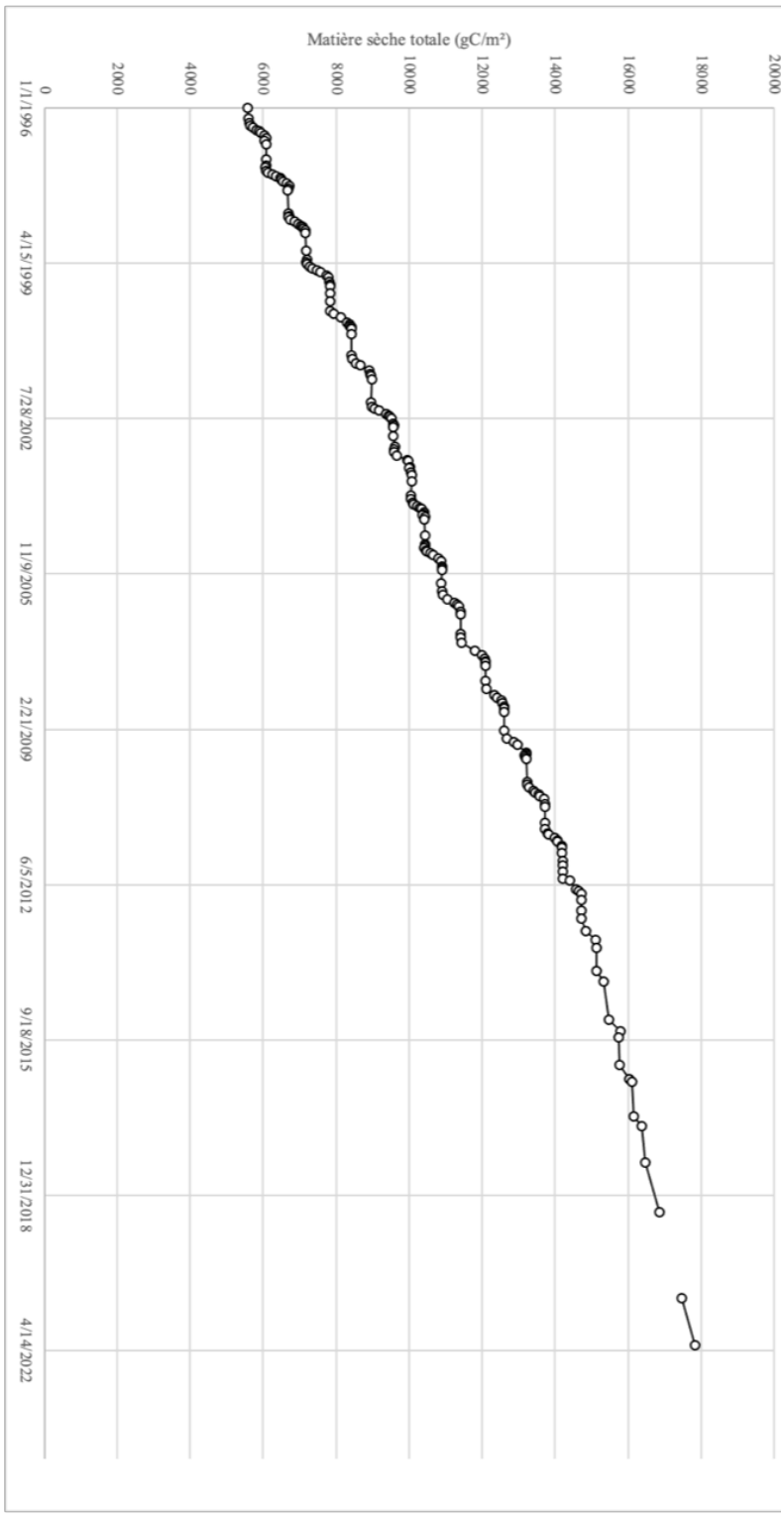

B Nitrodecline.F90 flow chart

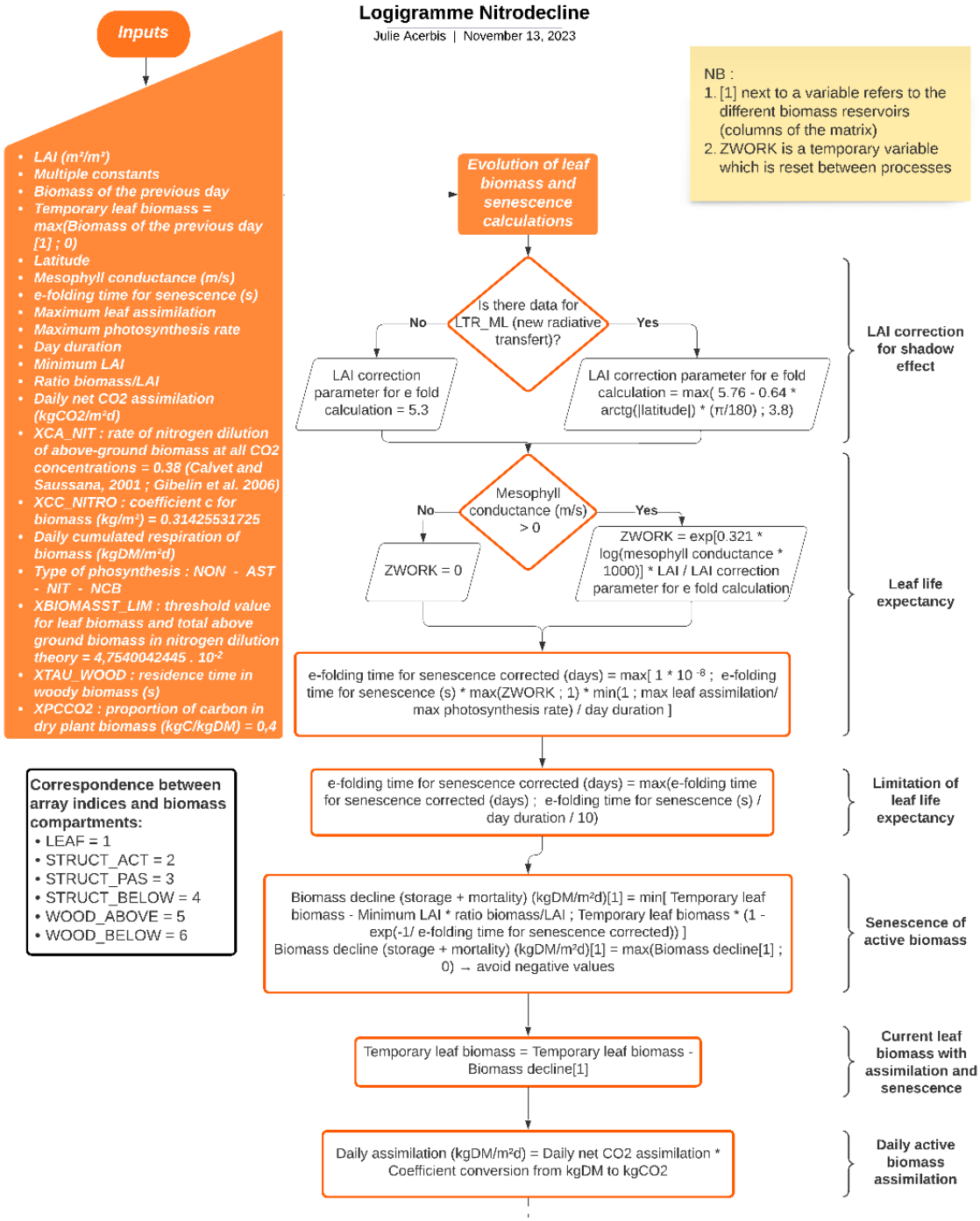

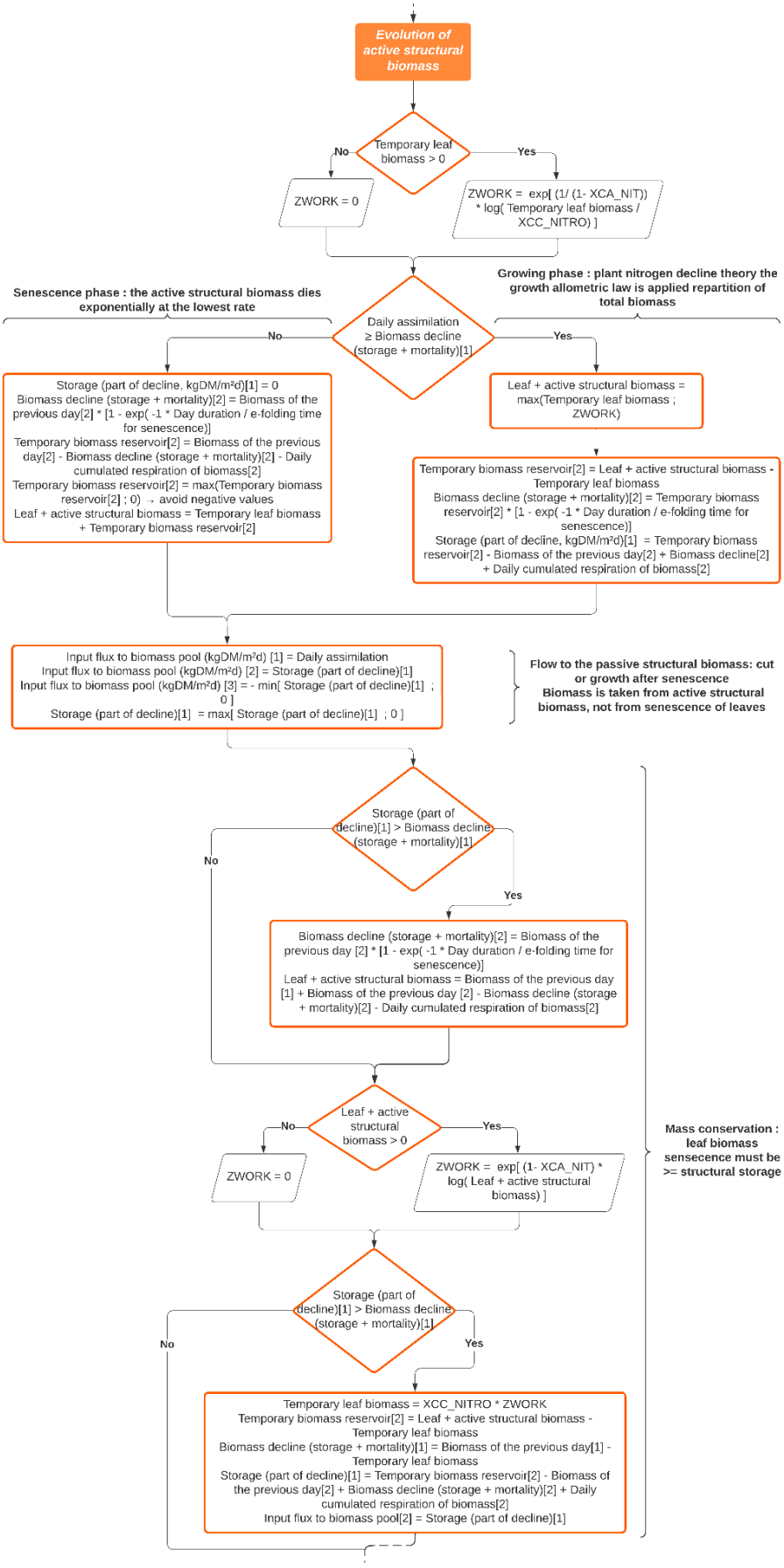
Evolution of active structural biomass
Temporary leaf biomass > 0
No
Yes
ZWORK = 0
ZWORK = exp[(1/ (1- XCA_NIT)) * log(Temporary leaf biomass / XCC_NITRO)]
Senescence phase : the active structural biomass dies exponentially at the lowest rate
Growing phase : plant nitrogen decline theory the growth allometric law is applied repartition of total biomass
Daily assimilation ≥ Biomass decline (storage + mortality)[1]
No
Yes
Storage (part of decline, kgDM/m²d)[1] = 0
Biomass decline (storage + mortality)[2] = Biomass of the previous day[2] * [1 - exp(-1 * Day duration / e-folding time for senescence)]
Temporary biomass reservoir[2] = Biomass of the previous day[2] - Biomass decline (storage + mortality)[2] - Daily cumulated respiration of biomass[2]
Temporary biomass reservoir[2] = max(Temporary biomass reservoir[2] ; 0) → avoid negative values
Leaf + active structural biomass = Temporary leaf biomass + Temporary biomass reservoir[2]
Leaf + active structural biomass = max(Temporary leaf biomass ; ZWORK)
Temporary biomass reservoir[2] = Leaf + active structural biomass - Temporary leaf biomass
Biomass decline (storage + mortality)[2] = Temporary biomass reservoir[2] * [1 - exp(-1 * Day duration / e-folding time for senescence)]
Storage (part of decline, kgDM/m²d)[1] = Temporary biomass reservoir[2] - Biomass of the previous day[2] + Biomass decline[2] + Daily cumulated respiration of biomass[2]
Input flux to biomass pool (kgDM/m²d) [1] = Daily assimilation
Input flux to biomass pool (kgDM/m²d) [2] = Storage (part of decline)[1]
Input flux to biomass pool (kgDM/m²d) [3] = - min[Storage (part of decline)[1] ; 0]
Storage (part of decline)[1] = max[Storage (part of decline)[1] ; 0]
Flow to the passive structural biomass: cut or growth after senescence
Biomass is taken from active structural biomass, not from senescence of leaves
Storage (part of decline)[1] > Biomass decline (storage + mortality)[1]
No
Yes
Biomass decline (storage + mortality)[2] = Biomass of the previous day [2] * [1 - exp(-1 * Day duration / e-folding time for senescence)]
Leaf + active structural biomass = Biomass of the previous day [1] + Biomass of the previous day [2] - Biomass decline (storage + mortality)[2] - Daily cumulated respiration of biomass[2]
Leaf + active structural biomass > 0
No
Yes
ZWORK = 0
ZWORK = exp[(1- XCA_NIT) * log(Leaf + active structural biomass)]
Mass conservation : leaf biomass sensecence must be >= structural storage
Storage (part of decline)[1] > Biomass decline (storage + mortality)[1]
No
Yes
Temporary leaf biomass = XCC_NITRO * ZWORK
Temporary biomass reservoir[2] = Leaf + active structural biomass - Temporary leaf biomass
Biomass decline (storage + mortality)[1] = Biomass of the previous day[1] - Temporary leaf biomass
Storage (part of decline)[1] = Temporary biomass reservoir[2] - Biomass of the previous day[2] + Biomass decline (storage + mortality)[2] + Daily cumulated respiration of biomass[2]
Input flux to biomass pool[2] = Storage (part of decline)[1]

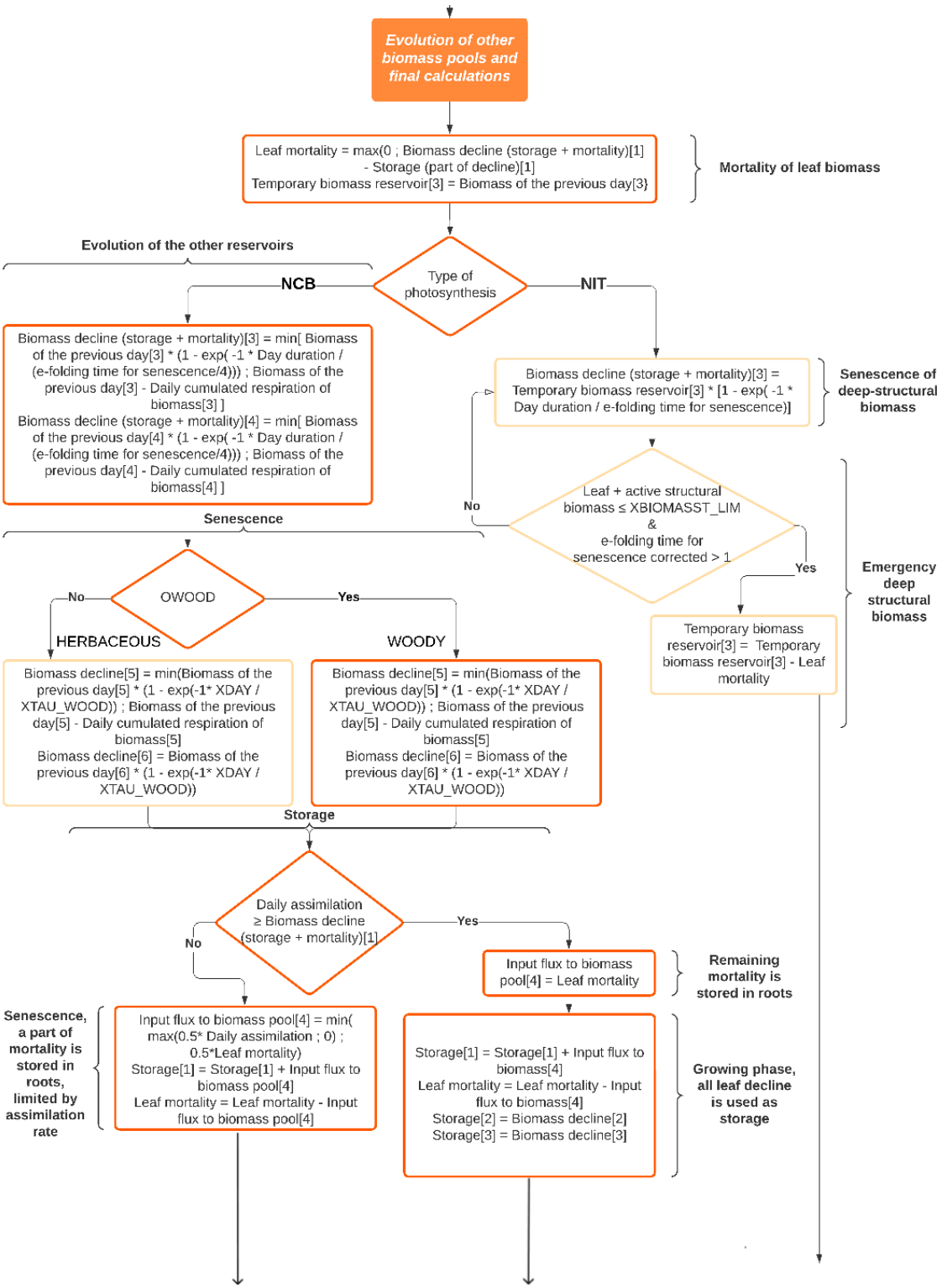
Evolution of other biomass pools and final calculations
Leaf mortality = max(0 ; Biomass decline (storage + mortality)[1] - Storage (part of decline)[1]
Temporary biomass reservoir[3] = Biomass of the previous day[3]
Mortality of leaf biomass
Evolution of the other reservoirs
Type of photosynthesis
NCB
NIT
Biomass decline (storage + mortality)[3] = min[Biomass of the previous day[3] * (1 - exp(-1 * Day duration / (e-folding time for senescence/4))) ; Biomass of the previous day[3] - Daily cumulated respiration of biomass[3]]
Biomass decline (storage + mortality)[4] = min[Biomass of the previous day[4] * (1 - exp(-1 * Day duration / (e-folding time for senescence/4))) ; Biomass of the previous day[4] - Daily cumulated respiration of biomass[4]]
Biomass decline (storage + mortality)[3] = Temporary biomass reservoir[3] * [1 - exp(-1 * Day duration / e-folding time for senescence)]
Senescence of deep-structural biomass
Leaf + active structural biomass ≤ XBIOMASST_LIM & e-folding time for senescence corrected > 1
No
Yes
Emergency deep structural biomass
Temporary biomass reservoir[3] = Temporary biomass reservoir[3] - Leaf mortality
Senescence
OWOOD
No
Yes
HERBACEOUS
WOODY
Biomass decline[5] = min(Biomass of the previous day[5] * (1 - exp(-1* XDAY / XTAU_WOOD)) ; Biomass of the previous day[5] - Daily cumulated respiration of biomass[5]
Biomass decline[6] = Biomass of the previous day[6] * (1 - exp(-1* XDAY / XTAU_WOOD))
Biomass decline[5] = min(Biomass of the previous day[5] * (1 - exp(-1* XDAY / XTAU_WOOD)) ; Biomass of the previous day[5] - Daily cumulated respiration of biomass[5]
Biomass decline[6] = Biomass of the previous day[6] * (1 - exp(-1* XDAY / XTAU_WOOD))
Storage
Daily assimilation ≥ Biomass decline (storage + mortality)[1]
No
Yes
Input flux to biomass pool[4] = Leaf mortality
Remaining mortality is stored in roots
Senescence, a part of mortality is stored in roots, limited by assimilation rate
Input flux to biomass pool[4] = min(max(0.5* Daily assimilation ; 0) ; 0.5*Leaf mortality)
Storage[1] = Storage[1] + Input flux to biomass pool[4]
Leaf mortality = Leaf mortality - Input flux to biomass pool[4]
Storage[1] = Storage[1] + Input flux to biomass[4]
Leaf mortality = Leaf mortality - Input flux to biomass[4]
Storage[2] = Biomass decline[2]
Storage[3] = Biomass decline[3]
Growing phase, all leaf decline is used as storage

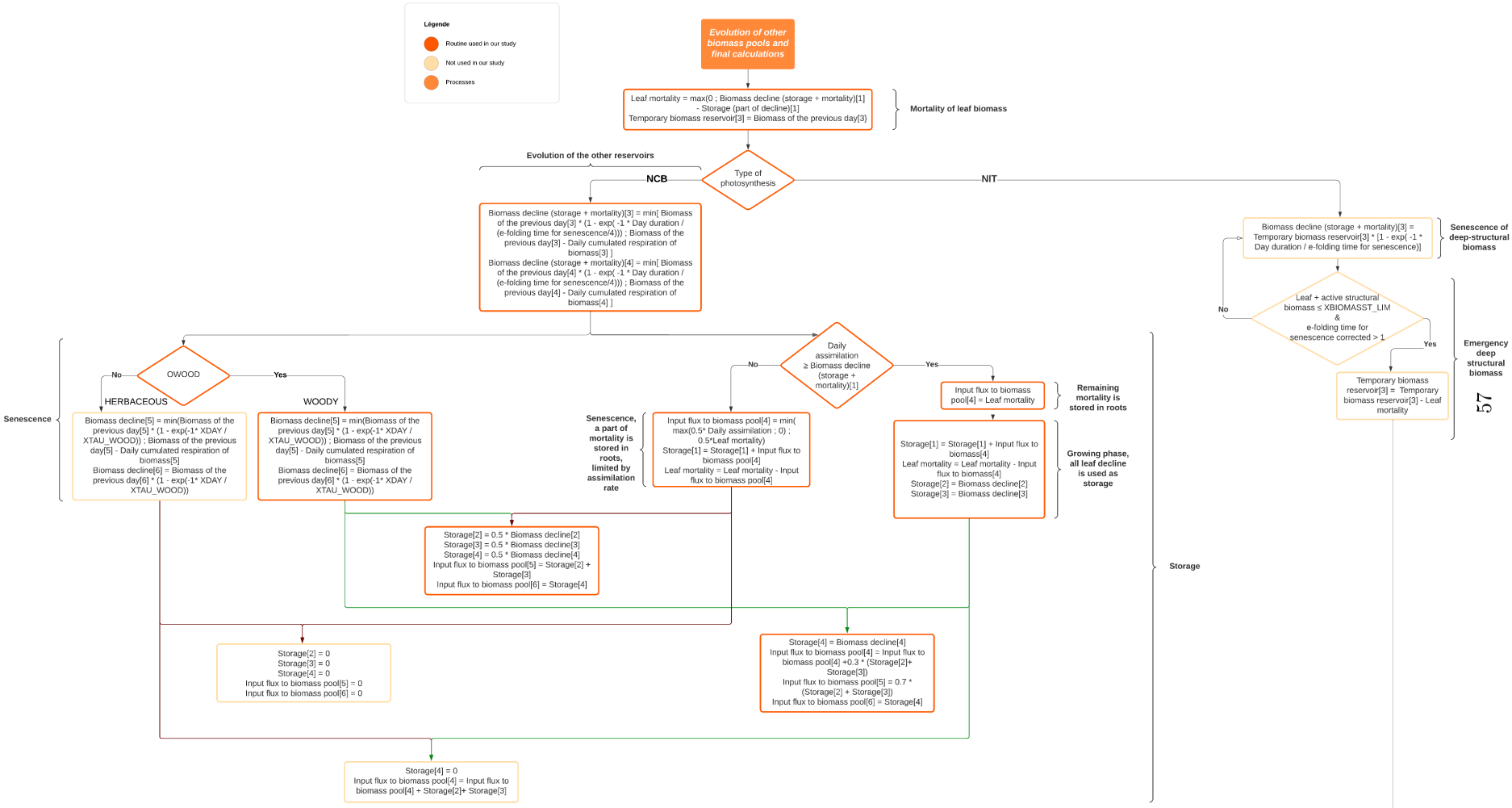
Légende
Routine used in our study
Not used in our study
Processes
Evolution of other biomass pools and final calculations
Leaf mortality = max(0 ; Biomass decline (storage + mortality)[1] - Storage (part of decline)[1]
Temporary biomass reservoir[3] = Biomass of the previous day[3]
Mortality of leaf biomass
Evolution of the other reservoirs
Type of photosynthesis
NCB
NIT
Biomass decline (storage + mortality)[3] = min[Biomass of the previous day[3] * (1 - exp(-1 * Day duration / (e-folding time for senescence/4))) ; Biomass of the previous day[3] - Daily cumulated respiration of biomass[3]]
Biomass decline (storage + mortality)[4] = min[Biomass of the previous day[4] * (1 - exp(-1 * Day duration / (e-folding time for senescence/4))) ; Biomass of the previous day[4] - Daily cumulated respiration of biomass[4]]
Biomass decline (storage + mortality)[3] = Temporary biomass reservoir[3] * [1 - exp(-1 * Day duration / e-folding time for senescence)]
Senescence of deep-structural biomass
Leaf + active structural biomass ≤ XBIOMASST_LIM & e-folding time for senescence corrected > 1
No
Yes
Emergency deep structural biomass
Temporary biomass reservoir[3] = Temporary biomass reservoir[3] - Leaf mortality
Daily assimilation ≥ Biomass decline (storage + mortality)[1]
No
Yes
Input flux to biomass pool[4] = Leaf mortality
Remaining mortality is stored in roots
Storage[1] = Storage[1] + Input flux to biomass[4]
Leaf mortality = Leaf mortality - Input flux to biomass[4]
Storage[2] = Biomass decline[2]
Storage[3] = Biomass decline[3]
Growing phase, all leaf decline is used as storage
Senescence, a part of mortality is stored in roots, limited by assimilation rate
Input flux to biomass pool[4] = min(max(0.5* Daily assimilation ; 0) ; 0.5*Leaf mortality)
Storage[1] = Storage[1] + Input flux to biomass[4]
Leaf mortality = Leaf mortality - Input flux to biomass pool[4]
Storage[2] = 0.5 * Biomass decline[2]
Storage[3] = 0.5 * Biomass decline[3]
Storage[4] = 0.5 * Biomass decline[4]
Input flux to biomass pool[5] = Storage[2] + Storage[3]
Input flux to biomass pool[6] = Storage[4]
Storage[4] = Biomass decline[4]
Input flux to biomass pool[4] = Input flux to biomass pool[4] +0.3 * (Storage[2]+ Storage[3])
Input flux to biomass pool[5] = 0.7 * (Storage[2] + Storage[3])
Input flux to biomass pool[6] = Storage[4]
Storage
Senescence
OWOOD
No
Yes
HERBACEOUS
WOODY
Biomass decline[5] = min(Biomass of the previous day[5] * (1 - exp(-1* XDAY / XTAU_WOOD)) ; Biomass of the previous day[5] - Daily cumulated respiration of biomass[5]
Biomass decline[6] = Biomass of the previous day[6] * (1 - exp(-1* XDAY / XTAU_WOOD))
Biomass decline[5] = min(Biomass of the previous day[5] * (1 - exp(-1* XDAY / XTAU_WOOD)) ; Biomass of the previous day[5] - Daily cumulated respiration of biomass[5]
Biomass decline[6] = Biomass of the previous day[6] * (1 - exp(-1* XDAY / XTAU_WOOD))
Storage[2] = 0
Storage[3] = 0
Storage[4] = 0
Input flux to biomass pool[5] = 0
Input flux to biomass pool[6] = 0
Storage[4] = 0
Input flux to biomass pool[4] = Input flux to biomass pool[4] + Storage[2]+ Storage[3]
17

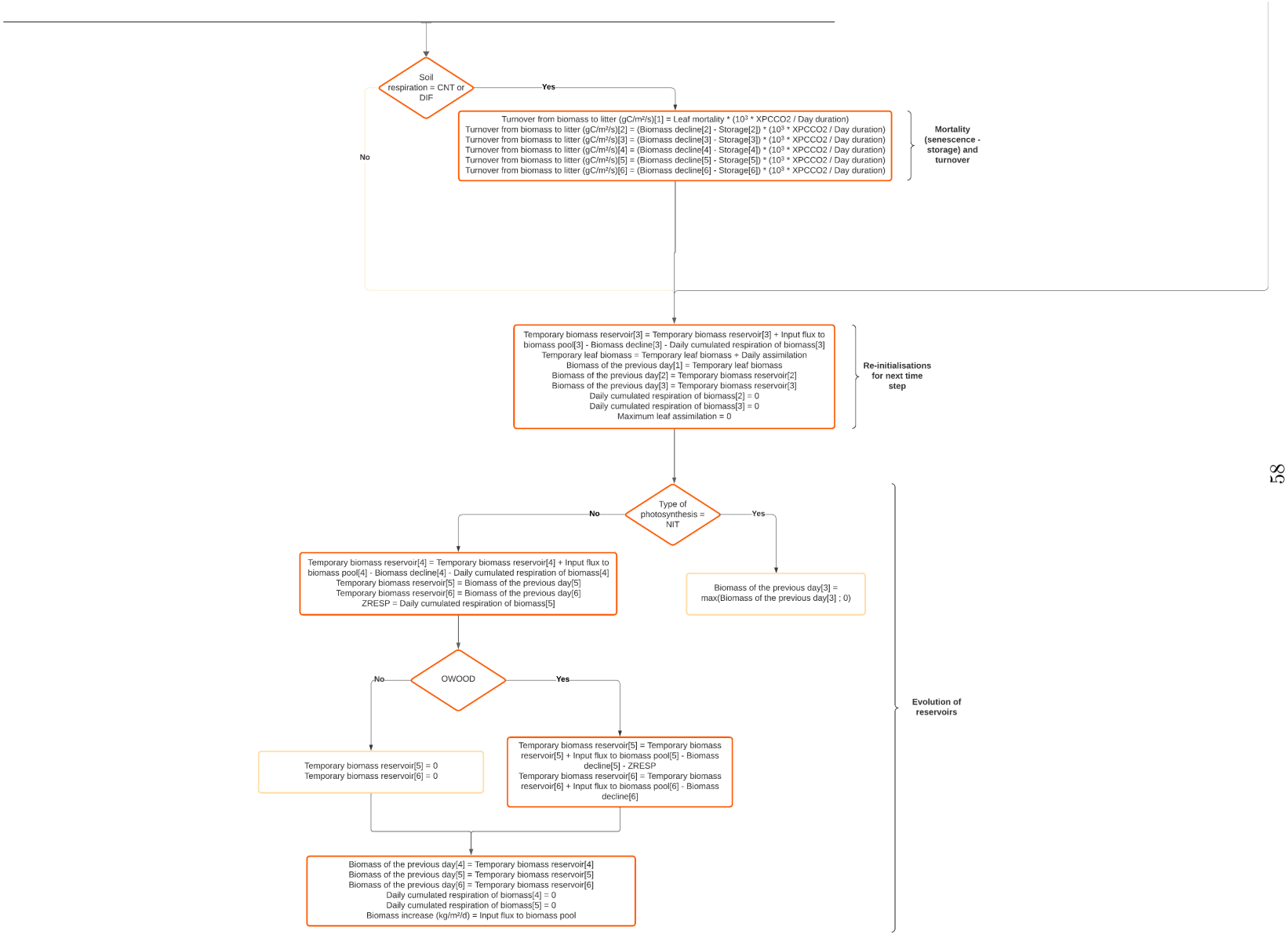
Soil respiration = CNT or DIF
Yes
No
Turnover from biomass to litter (gC/m²/s)[1] = Leaf mortality * (10³ * XPCCO2 / Day duration)
Turnover from biomass to litter (gC/m²/s)[2] = (Biomass decline[2] - Storage[2]) * (10³ * XPCCO2 / Day duration)
Turnover from biomass to litter (gC/m²/s)[3] = (Biomass decline[3] - Storage[3]) * (10³ * XPCCO2 / Day duration)
Turnover from biomass to litter (gC/m²/s)[4] = (Biomass decline[4] - Storage[4]) * (10³ * XPCCO2 / Day duration)
Turnover from biomass to litter (gC/m²/s)[5] = (Biomass decline[5] - Storage[5]) * (10³ * XPCCO2 / Day duration)
Turnover from biomass to litter (gC/m²/s)[6] = (Biomass decline[6] - Storage[6]) * (10³ * XPCCO2 / Day duration)
Mortality (senescence - storage) and turnover
Temporary biomass reservoir[3] = Temporary biomass reservoir[3] + Input flux to biomass pool[3] - Biomass decline[3] - Daily cumulated respiration of biomass[3]
Temporary leaf biomass = Temporary leaf biomass + Daily assimilation
Biomass of the previous day[1] = Temporary leaf biomass
Biomass of the previous day[2] = Temporary biomass reservoir[2]
Biomass of the previous day[3] = Temporary biomass reservoir[3]
Daily cumulated respiration of biomass[2] = 0
Daily cumulated respiration of biomass[3] = 0
Maximum leaf assimilation = 0
Re-initialisations for next time step
Type of photosynthesis = NIT
No
Yes
Temporary biomass reservoir[4] = Temporary biomass reservoir[4] + Input flux to biomass pool[4] - Biomass decline[4] - Daily cumulated respiration of biomass[4]
Temporary biomass reservoir[5] = Biomass of the previous day[5]
Temporary biomass reservoir[6] = Biomass of the previous day[6]
ZRESP = Daily cumulated respiration of biomass[5]
Biomass of the previous day[3] = max(Biomass of the previous day[3] ; 0)
OWOOD
No
Yes
Temporary biomass reservoir[5] = 0
Temporary biomass reservoir[6] = 0
Temporary biomass reservoir[5] = Temporary biomass reservoir[5] + Input flux to biomass pool[5] - Biomass decline[5] - ZRESP
Temporary biomass reservoir[6] = Temporary biomass reservoir[6] + Input flux to biomass pool[6] - Biomass decline[6]
Biomass of the previous day[4] = Temporary biomass reservoir[4]
Biomass of the previous day[5] = Temporary biomass reservoir[5]
Biomass of the previous day[6] = Temporary biomass reservoir[6]
Daily cumulated respiration of biomass[4] = 0
Daily cumulated respiration of biomass[5] = 0
Biomass increase (kg/m²/d) = Input flux to biomass pool
Evolution of reservoirs

C Spin-up outputs

The blue lines correspond to the modelled values on the 255 years of the spin-up, and the red line is the median for each iteration. The median was chosen as it isn't sensitive to extreme values.

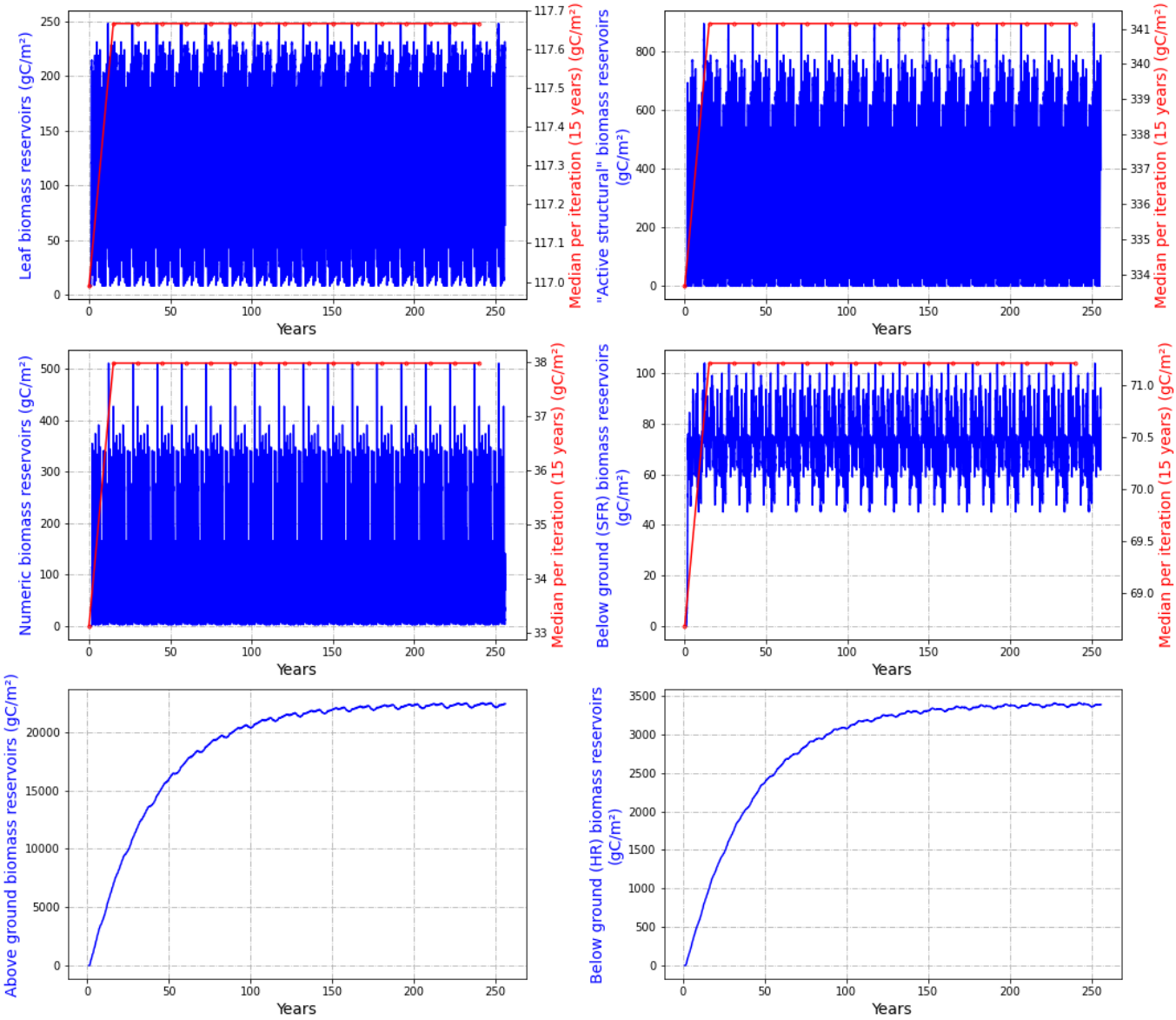

Figure 17: The outputs for the spin for each biomass.

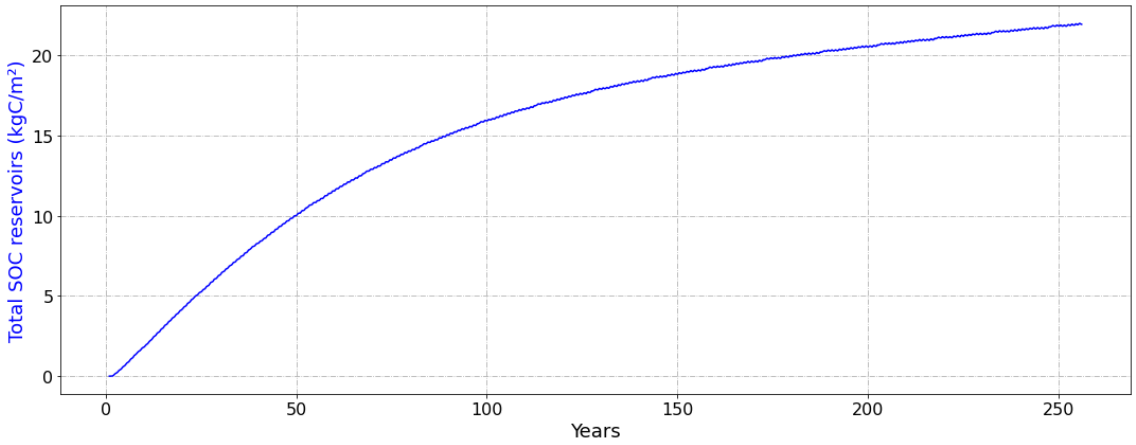

Figure 18: The outputs for the spin of the total soil organic carbon.

D Graphs of the water vapour fluxes

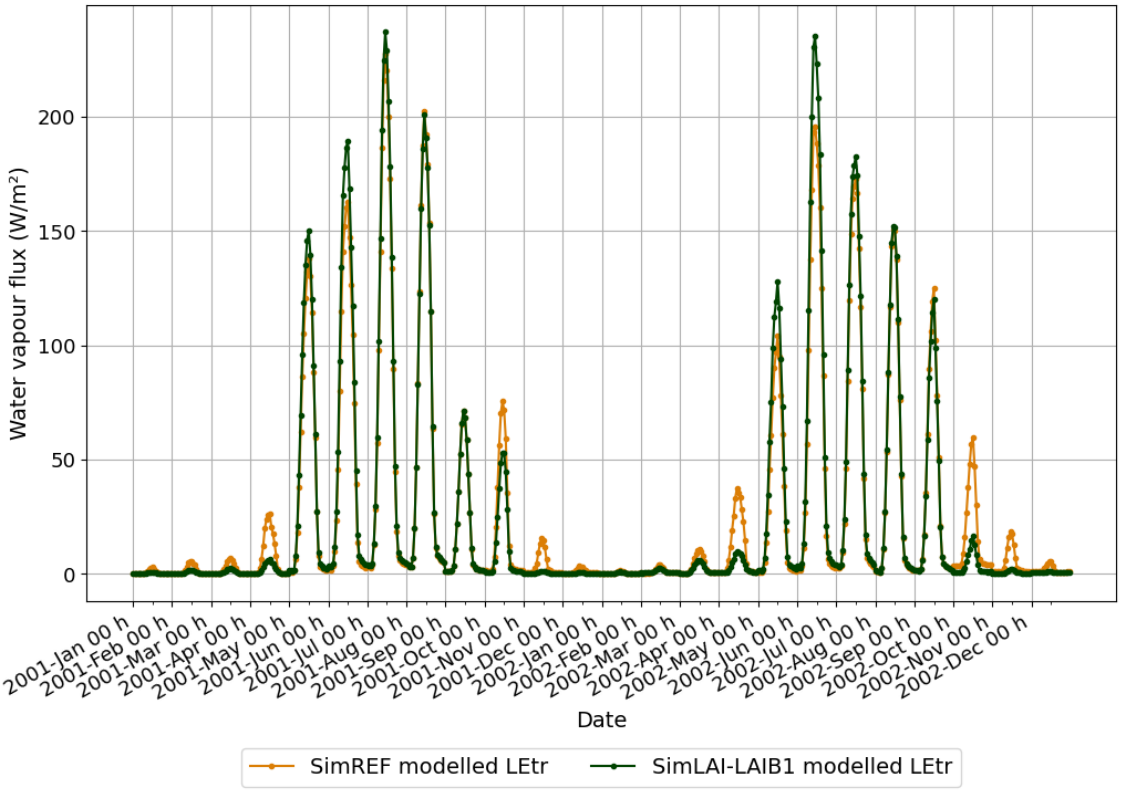

Figure 19: Graphs of the monthly average diurnal cycle of simulated transpiration from the foliage fraction which isn't covered by intercepted water for 2001 and 2002.

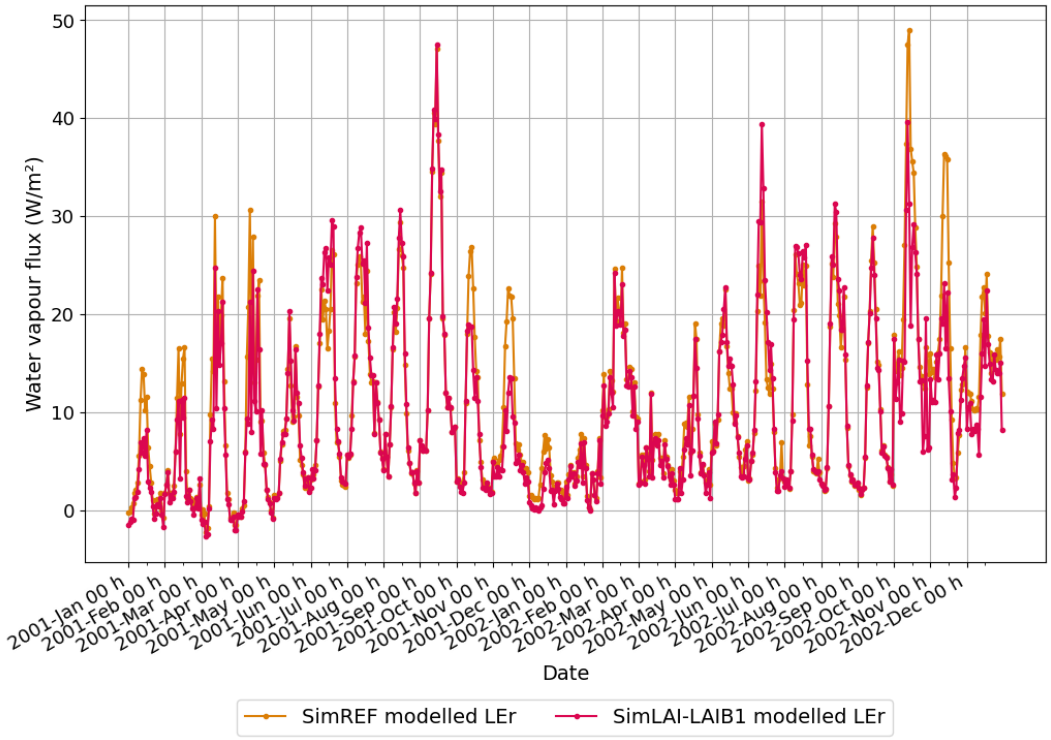

Figure 20: Graphs of the monthly average diurnal cycle of simulated direct evaporation from the fraction of the foliage covered by intercepted water for 2001 and 2002.

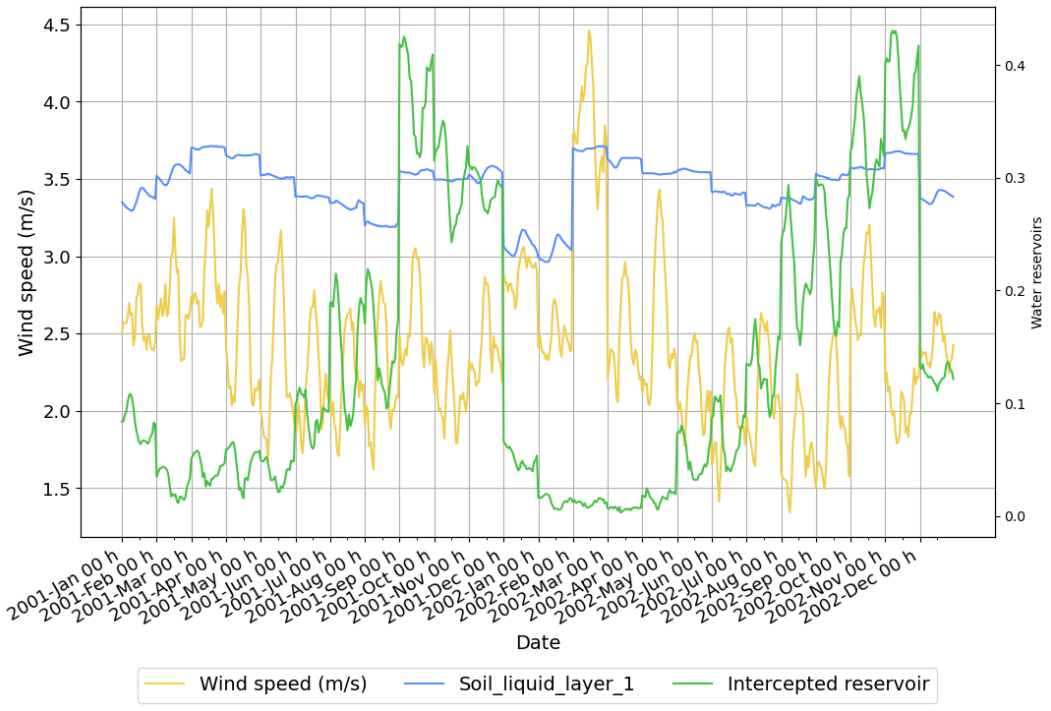

Figure 21: Graphs of the monthly average diurnal cycle of prognostic variables of the latent heat flux for 2001 and 2002 (SimREF).

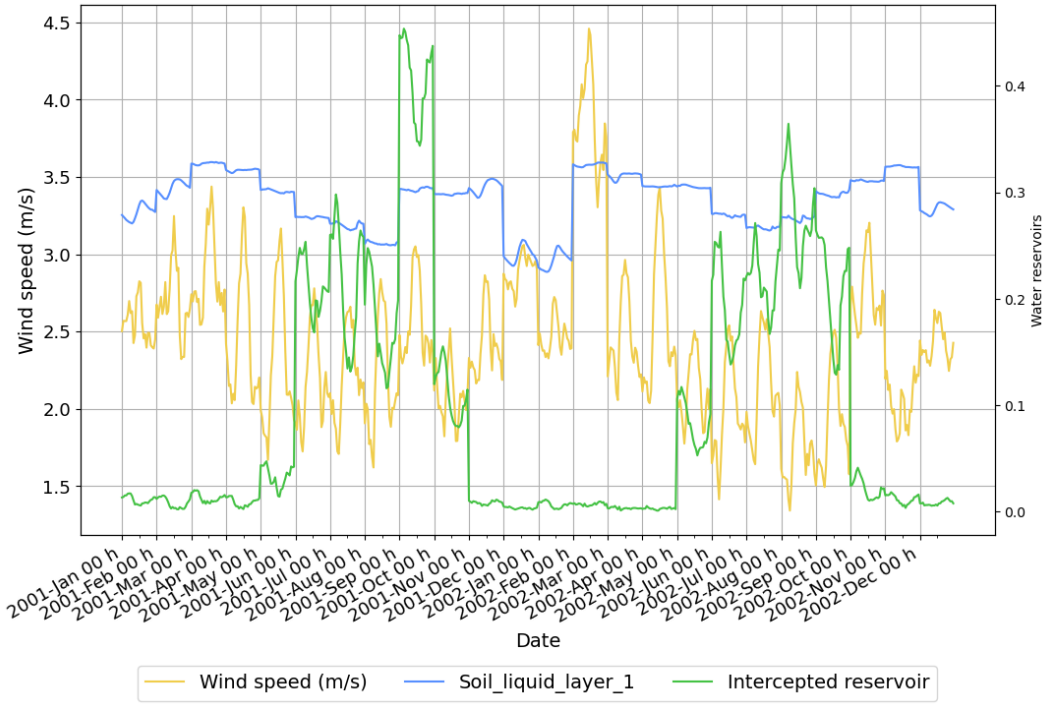

Figure 22: Graphs of the monthly average diurnal cycle of prognostic variables of the latent heat flux for 2001 and 2002 (SimLAI-LAIB1).

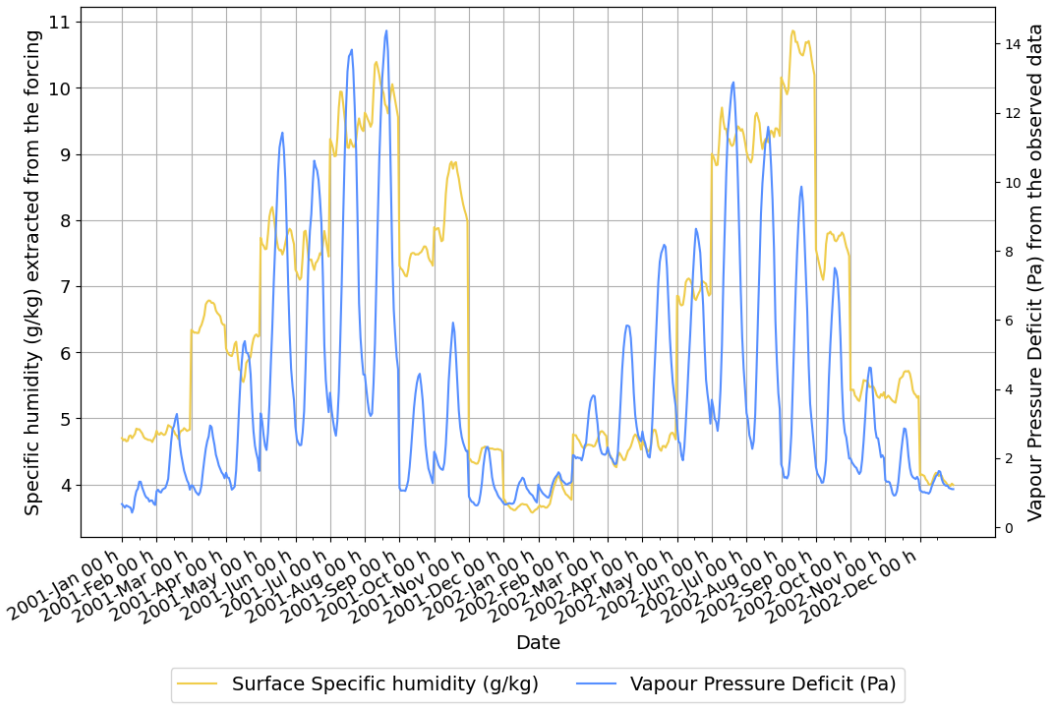

Figure 23: Graphs of the monthly average diurnal cycle of vapour deficit pressure (hPa) and specific humidity for 2001 and 2002.

E Graphs of the monthly average diurnal cycle for the drought year 2003

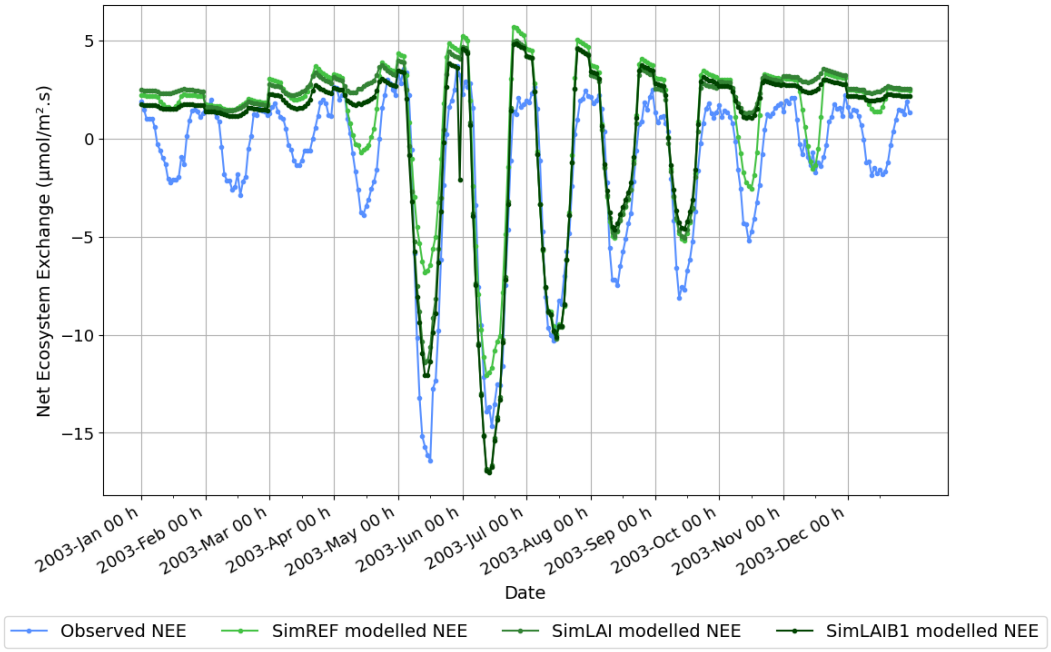

Figure 24: Graphs of the monthly average diurnal cycle of observed and simulated Net ecosystem exchange (µmol/m^{2}s) for the drought of 2003.

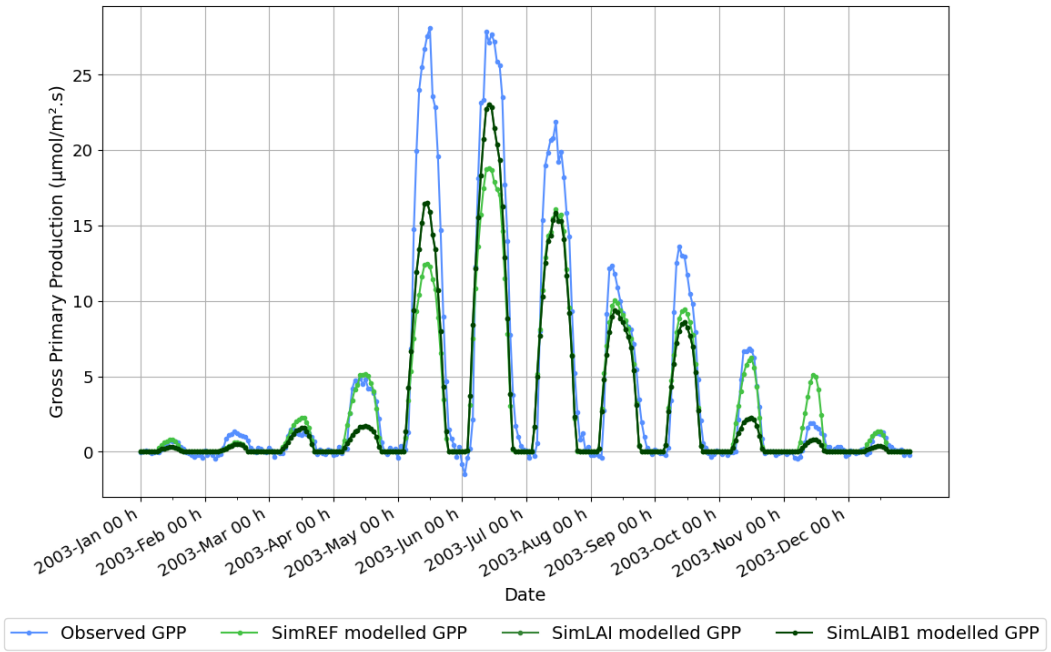

Figure 25: Graphs of the monthly average diurnal cycle of observed and simulated Gross Primary Production (µmol/m^{2}s) for the drought of 2003.

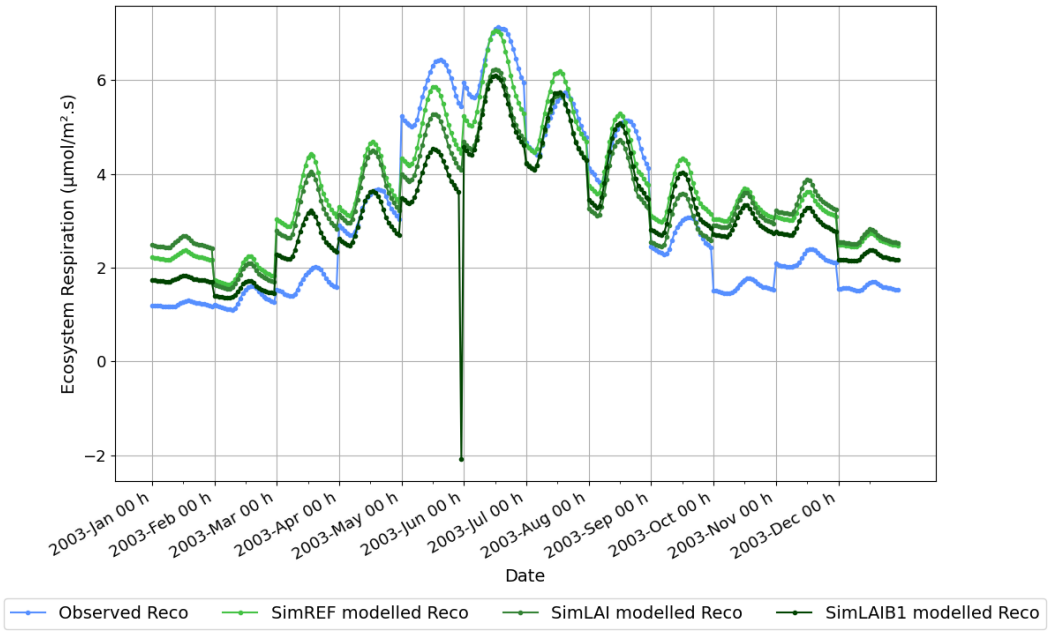

Figure 26: Graphs of the monthly average diurnal cycle of observed and simulated Ecosystem Respiration (µmol/m^{2}s) for the drought of 2003.

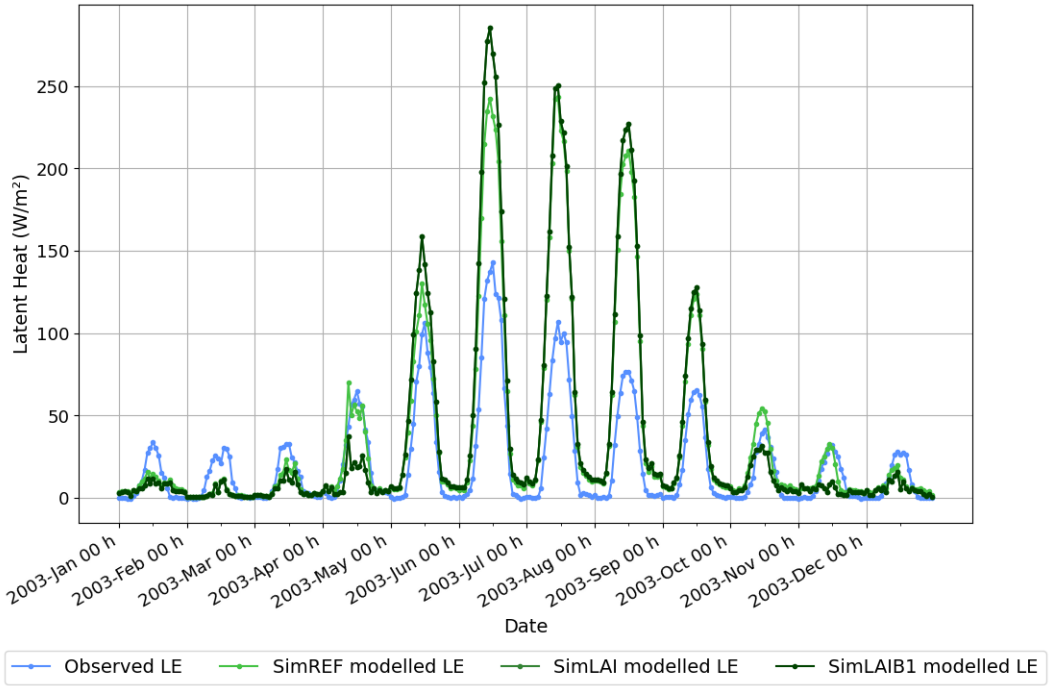

Figure 27: Graphs of the monthly average diurnal cycle of observed and simulated Latent Heat (W/m^2) for the drought of 2003.

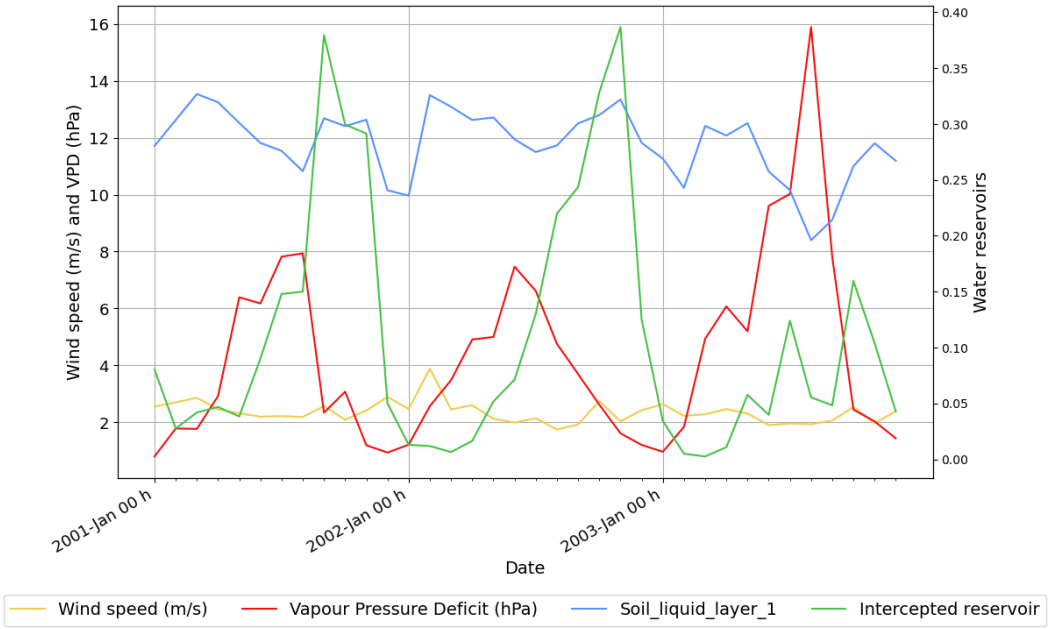

Figure 28: Graphs of the monthly average diurnal cycle of observed wind speed (m/s) and vapour deficit pressureand simulated Latent Heat (W/m^2) for the drought of 2003.